DEVELOPMENT OF LITHIUM SULFUR BATTERY BY INCORPORATION OF REDUCED GRAPHENE OXIDE AND MESOPOROUS CARBON NANOFIBER ENABLED BY AIR CONTROLLED ELECTROSPRAY METHOD

A Thesis

Presented to the Faculty of the Graduate School

of Cornell University

In Partial Fulfillment of the Requirements for the Degree of

Master of Science

by

Willy Sandi Halim

May 2018

ABSTRACT

The popularity of lithium-sulfur technology and graphene oxide have been surging following the rapid development of technology. High capacity and low cost of sulfur in conjunction with the high surface area and intriguing chemical and mechanical properties of graphene oxide (GO) are subject to many scientific interests. For my project, GO was primary interest to improve the electrochemical performance of lithium sulfur battery as a polysulfide inhibitor and active materials anchor. In chapter 1, GO was utilized as an interlayer to capture polysulfide. GO was coated onto mesoporous carbon nanofiber using air controlled electrospray method. We analyzed the performance of Li-S battery at different reduction temperatures under N_2 gas flow and found optimum performance at 300^{o}C. In chapter 2, GO was directly coated onto celgard separator along with the conductive polymer as an effective suppressor of polysulfide diffusion. In chapter 3, GO serves as a binder and polysulfide anchor to adhere active materials onto an aluminum substrate. The fabrication was carried by air controlled electrospray process. Air controlled electrospray process showed superior performance as opposed to conventional slurry method due to unique porous mechanical structure morphology and elimination of insulating polymer binder. Our conclusion indicated that air controlled electrospray process provides novel, facile, and scalable process to develop advance lithium-sulfur cells.

BIOGRAPHICAL SKETCH

Willy Halim was born in Jakarta, Indonesia on January 15th, 1992. Since he was a kid he dreamt to become a popular scientist to solve engineering and environmental problems around the world. Coming from a business background, his father forced him to pursue finance major instead of engineering when he decided to go to the United States. However, he successfully convinced his father to pursue chemical engineering due to his interest in mathematics. His passion escalated since he started working on Lithium sulfur battery with Prof. Yong Lak Joo.

Willy obtained his bachelor of science in Chemical Engineering from U.C. Berkeley in August 2014. Prior entering Cornell University as an M. Eng student, he was working with a distribution chemical company in Campbell, California. Before joining Prof. Joo's group to work on Lithium Sulfur Batteries, he was working on iron oxide nanoparticles with the supervision of Dr. Detlef Matthias Smilgies. However, he realized that his passion was not on nanoparticles. Then, he started working for Prof. Joo on Summer 2016 to develop high loading lithium sulfur batteries via air controlled electrospray under the supervision of Dr. Jaehyuk Lee. Since then, he realized that his work is more like as a hobby.

To my parents and friends.

ACKNOWLEDGMENTS

First of all, I would like to thank Prof. Yong Lak Joo and Axium Nanofiber that relentlessly support my lithium sulfur projects so that I can drill my skills as a scientist and engineer. Without Prof. Joo, I would not be able to progress this far, his valuable feedback and motivational speech always give me a chance to focus on my track and recharge my spirits, so that I progress faster than other graduate students, and also funding from Axium Nano that enables me to do characterization and fulfill my project with excellent results.

Secondly, I would like to thank Dr. Jin Hong Lee, a current postdoc at Joo group. His continuous support and feedback help me personally to take data, organize plans, work more efficiently, analyze characterization in depth, and be more ethically professional as a graduate student. I sincerely feel that his collaboration is the primary reason that I can accomplish this far.

Then, I would like to thank Dr. Jaehyuk Lee and Byunghee Ko who helped me getting started lithium sulfur project.

After that, I would like to thank all Joo group members who supported my work and make the lab more comfortable to work on. They are like my second family. Working with them provides more encouragement than any other.

And, I would like to thank CCMR that provides all the instruments to support my research.

Last, but not least, I would like to thank and dedicate my work to my parents, Lotus Amarta Halim and Shienny Laksana. I would never have been able to pursue an education in the United States and graduate school in Cornell without them. Their continuous support is the only reason that I was able to finish my education and be a professional in my career later on.

TABLE OF CONTENTS

PREFACE

Life in Cornell has been a roller coaster for me, particularly in my M.S. program working with Prof. Joo. It gave me invaluable experience as a researcher and a professional. Prof. Joo taught me how to be humble and selfless through numerous constructive feedback and criticism. I felt that his feedback and encouragement were the primary reason that I was able to progress this far. My learning process accelerated when I met Dr. Jinhong Lee, a mentor and a beloved friend who taught me lessons about research and life. He introduced a new way of thinking that I was never exposed to before. Viewing science through a new lens, I realized the aesthetic value of numbers and graphs from a researcher's point of view. He also ignited my curiosity and challenged me to stand on my ground and provide clear and meaningful data. To Prof. Joo and Dr. Jinhong Lee, I hope that this thesis can provide a solid evidence as a result of my learning process from both of my teacher and future professor.

CHAPTER 1

INTRODUCTION

Overview of Lithium Sulfur Battery

Amid the rapid development of electronics and electrical vehicles and the needs to incorporate energy storage technology to save power from sustainable power sources, advanced electrochemical energy storage has rapidly gained momentum. The most popular lithium-ion technology is approaching its limit. One of the most promising candidates in electrochemistry technology is lithium sulfur battery. Its popularity owes due to lower cost, environmentally benign, and 3-5 folds higher theoretical energy density compared to lithium-ion [1–4]. This technology has been subjected to many interest from scientists and investors.

Unfortunately, many problems persist in applying lithium-sulfur technology to the current technology. One is rapid fading in capacity due to the dissolution of intermediary product and migration of polysulfide that significantly reduce the active materials. Next, the insulating attribute of sulfur causes low sulfur utilization. Then, toxic electrolyte and uses of lithium metal as a source of lithium ion are causing safety concern [5,6].

To overcome this problem scientists have been applying various approaches in the past decade. Various carbon and interlayer have been implemented to serve as an electrical conduit and immobilize the polysulfides migration; for example graphene oxide [7–9], graphene sheets [10,11], carbon nanotube [12,13], carbon nanofiber [14–

17], or any functionalized carbon materials [18,19]. The first scientific breakthrough on lithium-sulfur was published by Linda Nazar on a highly ordered nanostructured carbon-sulfur cathode at 2008 [20]. Since then, other carbon-based materials start to be implemented to enhance the performance of lithium-sulfur battery. Most of the scientists focused their research on the chemistry of the cathodes [19,21–24]. Another research interest lies the separator. By coating graphene oxide or metal oxides such as TiO2, ZnO, or MOF on the separator, the polysulfide is greatly suppressed. In general, the modified separator should offer ion selectivity, physical absorption, and chemical bonding with polysulfides [25,26]. Therefore, only solvated Li^+ may pass through the membrane while the polysulfides are blocked. Then, the coating should not increase the electrical resistivity significantly or safety concern. Next, from electrolyte point of view, the addition of $LiNO_3$ in the electrolyte solution enhances the cell performance significantly [27,28]. It is believed that $LiNO_3$ oxidized the Li_xS to form protective SEI layer on Li, which largely eliminate the shuttle reactions. The setback, however, discharge below 1.7V can decompose $LiNO_3$ additive on the anode side, which exacerbates the fading capacity of Lithium-sulfur battery. Hence, discharge cutoff below 1.7V should be avoided. In addition, the current practical electrolyte (LiTFSI in DOL:DME or THF in TEGDME) for laboratory work was extremely toxic and raises safety issues. So, gel polymer electrolyte is also investigated, and several scientific literatures indicate that gel polymer electrolyte provides higher specific capacity compared to conventional liquid electrolyte. Aside from the superior performance, gel polymer electrolyte also mitigates safety concern [29].

The chemistry, crystallinity, and morphology of cathodes and anodes were scientist's primary interests to improve the energy density of the lithium-sulfur battery. Most of the electrode fabrications were carried out using slurry coating method, which relied mostly on the binder to adhere the active materials onto the current electrode and also requires drying process that causes cracking. Most conventional polymer binders, like PVDF, PAA, LiPAA, PEO, etc. cause an inimical effect on the cell, due to its insulating property. To circumvent that problem, several scientists modified functional group to reduce the resistivity or anchor the polysulfides [30,31]. Moreover, the application of the slurry coating is not suitable for high loading, because it leads to cracking once the sulfur mass is above 3.5 mg cm^{-2} [32,33]. In fact, high loading of active sulfur material is necessary to compete with commercial lithium-ion battery. Therefore slurry coating method is not applicable to achieve a high loading of sulfur. One method to achieve high capacity with relatively high loading 5 mg cm^{-2} or more is by utilizing activated mesoporous carbon nanofiber as a substrate to deposit the electrode [21]. There are several ways to deposit sulfur substrate into carbon fiber, the most popular one is by melt impregnation, which developed by Manthiram group and the other is by air-controlled electrospray which was developed by Joo group.

Kinetics of lithium-sulfur battery

The lithiation of sulfur involves several state changes. During the discharge process, a solid sulfur material began with the reduction of lithium polysulfide (Li_2S_8),

which dissolves into the electrolyte and subsequently reduced to lower order polysulfides (Li_2S_6, Li_2S_4). During this dissolution, the higher order polysulfide tends to migrate to lithium anode and creates surface passivation. Then the lower order polysulfides are then further reduced to insoluble Li_2S, which precipitates from the electrolyte. Three-quarters of the theoretical capacity comes from the reduction of the final state, Li_2S_4 to Li_2S_2 or Li_2S. Since Li_2S is an electronic insulator, electrically conductive material such as carbon-based materials, conductive polymer or metal oxides is added to facilitate charge transfer and to provide a substrate for the electrodeposition reactions. Several challenges need elucidation to achieve high capacity reversible reactions, including generally slow redox kinetics, the high electronic resistivity in the precipitate, and possible detachment of precipitates from carbon hosts [34]. For charge reaction, insoluble polysulfide converted to lower order soluble polysulfide (Li_2S_6 , Li_2S_4) and followed by higher order polysulfide Li_2S_8 and eventually back to S_8. The typical charge/discharge profile of lithium-sulfur is displayed on Figure 1.1 below.

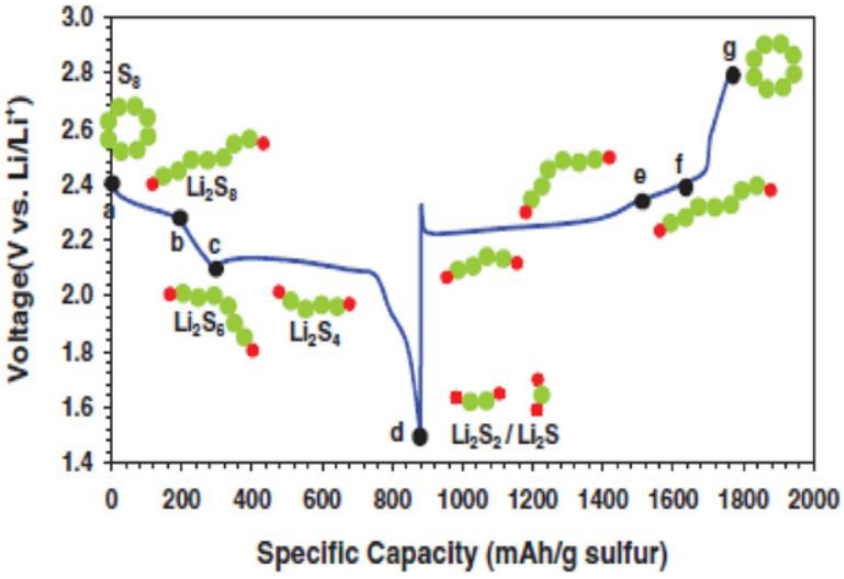

Figure 1.1 Lithium-sulfur typical charge/discharge profile [35].

The precipitation of insoluble polysulfide on conductive substrates proceeds via nucleation, followed by 2D growth occurring at the three-phase boundary between precipitate, substrate, and electrolyte. Growth was limited to precipitate impingement. Precipitation during galvanostatic cycling produces different Li_2S morphology depending on the current rate. At high C-rates larger overpotentials produce smaller nuclei and high nuclei density, resulting in a thin film across the substrate, whereas lower C-rates produce larger nuclei but fewer precipitates. High storage capacities via Li2S precipitation can be realized through control of conductive substrate's surface area, choice of solvent, and appropriate electrokinetic control of the nucleation and growth process [36,37].

Air controlled electrospray process

Electrospray is one of the most versatile ionization techniques for the investigation of macromolecules. It was introduced in 1984 by Yamashita, Fenn, and Aleksandrov et al. simultaneously [38,39]. In electrospraying, the liquid at the outlet of a nozzle is subjected to electrical shear stress by maintaining the high voltage at the nozzle. Electrospray can tune the droplets sizes, in a special case, down to the nanometer. The charge and size of droplets can be controlled to some extent by adjusting flow rate and voltage. Due to its properties, electrospraying is considered an effective journey to nanotechnology [40,41].

In this lithium-sulfur project, air-controlled electrospray process was frequently utilized for coating and depositing active materials. Unlike conventional electrospray, air-controlled electrospray utilizes convective jet flow to create smaller

droplets that enhance evaporation process, leaving dry solute behind. It is an effective method for coating as it can deposit various materials on many surfaces. Also, this process allows more effective electrode fabrication, as the dry solute eliminate the needs of additional drying, which offers the potential for scaling up and offer many new opportunities for electrochemical research. The difference between electrospray and air controlled electrospray is illustrated in Illustration 1.1 below

Illustration 1.1 The schematic difference of air controlled electrospray and electrospray for lithium-ion battery application [42]

Organization

In Chapter 1 and 2, air controlled electrospray process is utilized to coat graphene oxide and conductive polymer: PEDOT:PSS graphene to suppress the polysulfides migration. In chapter 1, the effects of electrical conductivity and oxide content on lithium-sulfur electrochemical performance was explored. Graphene oxide

was coated on top of mesoporous carbon nanofiber and thermally reduced at various temperatures to tune the oxide content and conductivity to determine the best performance of lithium-sulfur battery. Then, in chapter 2, the effect of conductive polymer PEDOT:PSS was explored. Commercially available partially reduced graphene was dispersed in water with PEDOT:PSS as a surfactant. Then the solution was coated onto the Celgard separator to block polysulfide migration and explore the synergy between active material utilization and lithium-sulfur battery performance. Lastly, in Chapter 3, this process was utilized to deposit active materials onto current electrode without any binder by utilizing Van Der Waals interaction between graphene oxide and aluminum oxide. We explored the effect of binder-free and rough morphology on the electrical conductivity and electrochemical performance of Lithium-sulfur battery. Details on air-controlled electrospray process conditions will be discussed in each chapter.

REFERENCES

[1] A. Manthiram, Y. Fu, Y.-S. Su, Challenges and Prospects of Lithium-Sulfur Batteries, Acc. Chem. Res. (2012). doi:10.1021/ar300179v.

[2] A. Manthiram, S.-H. Chung, C. Zu, Lithium-Sulfur Batteries: Progress and Prospects., Adv. Mater. (2015) 1–27. doi:10.1002/adma.201405115.

[3] G. Zhou, F. Li, H.-M. Cheng, Progress in flexible lithium batteries and future prospects, Energy Environ. Sci. 7 (2014) 1307–1338. doi:10.1039/C3EE43182G.

[4] J. Lochala, D. Liu, B. Wu, C. Robinson, J. Xiao, Research Progress toward the Practical Applications of Lithium–Sulfur Batteries, ACS Appl. Mater. Interfaces. 9 (2017) 24407–24421. doi:10.1021/acsami.7b06208.

[5] A. Manthiram, Y. Fu, Y.-S. Su, Challenges and Prospects of Lithium–Sulfur Batteries, Acc. Chem. Res. 46 (2013) 1125–1134. doi:10.1021/ar300179v.

[6] N. Deng, W. Kang, Y. Liu, J. Ju, D. Wu, L. Li, B.S. Hassan, B. Cheng, A review on separators for lithiumsulfur battery: Progress and prospects, J. Power Sources. 331 (2016) 132–155. doi:10.1016/j.jpowsour.2016.09.044.

[7] L. Ji, M. Rao, H. Zheng, L. Zhang, Y. Li, W. Duan, J. Guo, E.J. Cairns, Y. Zhang, Graphene oxide as a sulfur immobilizer in high performance lithium/sulfur cells, J. Am. Chem. Soc. 133 (2011) 18522–18525. doi:10.1021/ja206955k.

[8] S. Stankovich, D.A. Dikin, R.D. Piner, K.A. Kohlhaas, A. Kleinhammes, Y. Jia,

Y. Wu, S.B.T. Nguyen, R.S. Ruoff, Synthesis of graphene-based nanosheets via chemical reduction of exfoliated graphite oxide, Carbon N. Y. 45 (2007) 1558–1565. doi:10.1016/j.carbon.2007.02.034.

[9] J.Q. Huang, T.Z. Zhuang, Q. Zhang, H.J. Peng, C.M. Chen, F. Wei, Permselective graphene oxide membrane for highly stable and anti-self-discharge lithium-sulfur batteries, ACS Nano. 9 (2015) 3002–3011. doi:10.1021/nn507178a.

[10] T. Wei, G. Luo, Z. Fan, C. Zheng, J. Yan, C. Yao, W. Li, C. Zhang, Preparation of graphene nanosheet/polymer composites using in situ reduction-extractive dispersion, Carbon N. Y. 47 (2009) 2296–2299. doi:10.1016/j.carbon.2009.04.030.

[11] X. Liang, C. Hart, Q. Pang, A. Garsuch, T. Weiss, L.F. Nazar, A highly efficient polysulfide mediator for lithium–sulfur batteries, Nat. Commun. 6 (2015) 5682. doi:10.1038/ncomms6682.

[12] A. Barinov, L. Gregoratti, P. Dudin, S. La Rosa, M. Kiskinova, Imaging and spectroscopy of multiwalled carbon nanotubes during oxidation: Defects and oxygen bonding, Adv. Mater. 21 (2009) 1916–1920. doi:10.1002/adma.200803003.

[13] J. Guo, Y. Xu, C. Wang, Sulfur-impregnated disordered carbon nanotubes cathode for lithium-sulfur batteries, Nano Lett. 11 (2011) 4288–4294. doi:10.1021/nl202297p.

[14] J. Wang, Y. Yang, F. Kang, Porous carbon nanofiber paper as an effective interlayer for high-performance lithium-sulfur batteries, Electrochim. Acta. 168

(2015) 271–276. doi:10.1016/j.electacta.2015.04.055.

[15] M. Rao, X. Song, E.J. Cairns, Nano-carbon/sulfur composite cathode materials with carbon nanofiber as electrical conductor for advanced secondary lithium/sulfur cells, J. Power Sources. 205 (2012) 474–478. doi:10.1016/j.jpowsour.2012.01.047.

[16] B.P. Williams, Y.L. Joo, Tunable Large Mesopores in Carbon Nanofiber Interlayers for High-Rate Lithium Sulfur Batteries, J. Electrochem. Soc. 163 (2016) A2745–A2756. doi:10.1149/2.0931613jes.

[17] J. Lee, B. Ko, J. Kang, Y. Chung, Y. Kim, W. Halim, J.H. Lee, Y.L. Joo, Facile and scalable fabrication of highly loaded sulfur cathodes and lithium–sulfur pouch cells via air-controlled electrospray, Mater. Today Energy. 6 (2017) 255–263. doi:10.1016/j.mtener.2017.11.003.

[18] J. Song, T. Xu, M.L. Gordin, P. Zhu, D. Lv, Y.B. Jiang, Y. Chen, Y. Duan, D. Wang, Nitrogen-doped Mesoporous carbon promoted chemical adsorption of sulfur and fabrication of high-Areal-capacity sulfur cathode with exceptional cycling stability for lithium-sulfur batteries, Adv. Funct. Mater. 24 (2014) 1243–1250. doi:10.1002/adfm.201302631.

[19] Q. Pang, J. Tang, H. Huang, X. Liang, C. Hart, K.C. Tam, L.F. Nazar, A Nitrogen and Sulfur Dual-Doped Carbon Derived from Polyrhodanine@Cellulose for Advanced Lithium-Sulfur Batteries, Adv. Mater. 27 (2015) 6021–6028. doi:10.1002/adma.201502467.

[20] X. Ji, K.T. Lee, L.F. Nazar, A highly ordered nanostructured carbon–sulphur cathode for lithium–sulphur batteries, Nat. Mater. 8 (2009) 500–506.

doi:10.1038/nmat2460.

[21] L. Qie, C. Zu, A. Manthiram, A High Energy Lithium-Sulfur Battery with Ultrahigh-Loading Lithium Polysulfide Cathode and its Failure Mechanism, Adv. Energy Mater. 6 (2016). doi:10.1002/aenm.201502459.

[22] A. Manthiram, Y. Fu, S.H. Chung, C. Zu, Y.S. Su, Rechargeable lithium-sulfur batteries, Chem. Rev. 114 (2014) 11751–11787. doi:10.1021/cr500062v.

[23] G. He, X. Ji, L. Nazar, High "C" rate Li-S cathodes: sulfur imbibed bimodal porous carbons, Energy Environ. Sci. 4 (2011) 2878. doi:10.1039/c1ee01219c.

[24] Y. Yang, G. Zheng, Y. Cui, Nanostructured sulfur cathodes, Chem. Soc. Rev. 42 (2013) 3018. doi:10.1039/c2cs35256g.

[25] T. Zhao, Y. Ye, X. Peng, G. Divitini, H.K. Kim, C.Y. Lao, P.R. Coxon, K. Xi, Y. Liu, C. Ducati, R. Chen, R.V. Kumar, Advanced Lithium–Sulfur Batteries Enabled by a Bio-Inspired Polysulfide Adsorptive Brush, Adv. Funct. Mater. 26 (2016) 8418–8426. doi:10.1002/adfm.201604069.

[26] S. Bai, X. Liu, K. Zhu, S. Wu, H. Zhou, Metal-organic framework-based separator for lithium-sulfur batteries, Nat. Energy. 1 (2016). doi:10.1038/nenergy.2016.94.

[27] S.S. Zhang, A review on electrolyte additives for lithium-ion batteries, J. Power Sources. 162 (2006) 1379–1394. doi:10.1016/j.jpowsour.2006.07.074.

[28] S.S. Zhang, Role of LiNO 3 in rechargeable lithium/sulfur battery, Electrochim. Acta. 70 (2012) 344–348. doi:10.1016/j.electacta.2012.03.081.

[29] M. Liu, D. Zhou, Y.B. He, Y. Fu, X. Qin, C. Miao, H. Du, B. Li, Q.H. Yang, Z. Lin, T.S. Zhao, F. Kang, Novel gel polymer electrolyte for high-performance

lithium-sulfur batteries, Nano Energy. 22 (2016) 278–289. doi:10.1016/j.nanoen.2016.02.008.

[30] G. Xu, Q. bo Yan, A. Kushima, X. Zhang, J. Pan, J. Li, Conductive graphene oxide-polyacrylic acid (GOPAA) binder for lithium-sulfur battery, Nano Energy. 31 (2017) 568–574. doi:10.1016/j.nanoen.2016.12.002.

[31] P. Bhattacharya, M.I. Nandasiri, D. Lv, A.M. Schwarz, J.T. Darsell, W.A. Henderson, D.A. Tomalia, J. Liu, J.G. Zhang, J. Xiao, Polyamidoamine dendrimer-based binders for high-loading lithium-sulfur battery cathodes, Nano Energy. 19 (2016) 176–186. doi:10.1016/j.nanoen.2015.11.012.

[32] S. Urbonaite, T. Poux, P. Novák, Progress Towards Commercially Viable Li-S Battery Cells, Adv. Energy Mater. 5 (2015). doi:10.1002/aenm.201500118.

[33] N. Ding, S.W. Chien, T.S.A. Hor, Z. Liu, Y. Zong, Key parameters in design of lithium sulfur batteries, J. Power Sources. 269 (2014) 111–116. doi:10.1016/j.jpowsour.2014.07.008.

[34] F.Y. Fan, W.C. Carter, Y.-M. Chiang, Mechanism and Kinetics of Li2S Precipitation in Lithium–Sulfur Batteries, Adv. Mater. 27 (2015) 5203–5209. doi:10.1002/adma.201501559.

[35] M. Barghamadi, A.S. Best, A.I. Bhatt, A.F. Hollenkamp, M. Musameh, R.J. Rees, T. Rüther, Lithium–sulfur batteries—the solution is in the electrolyte, but is the electrolyte a solution?, Energy Environ. Sci. 7 (2014) 3902–3920. doi:10.1039/C4EE02192D.

[36] Y.X. Ren, T.S. Zhao, M. Liu, P. Tan, Y.K. Zeng, Modeling of lithium-sulfur batteries incorporating the effect of Li2S precipitation, J. Power Sources. 336

(2016) 115–125. doi:10.1016/j.jpowsour.2016.10.063.

[37] H. Noh, J. Song, J.-K. Park, H.-T. Kim, A new insight on capacity fading of lithium–sulfur batteries: The effect of Li2S phase structure, J. Power Sources. 293 (2015) 329–335. doi:10.1016/j.jpowsour.2015.05.072.

[38] M. Yamashita, J.B. Fenn, Electrospray ion source. Another variation on the free-jet theme, J. Phys. Chem. 88 (1984) 4451–4459. doi:10.1021/j150664a002.

[39] M.L. Alexandrov, L.N. Gall, N. V. Krasnov, V.I. Nikolaev, V.A. Pavlenko, V.A. Shkurov, Extraction of ions from solutions under atmospheric pressure as a method for mass spectrometric analysis of bioorganic compounds, Rapid Commun. Mass Spectrom. 22 (2008) 267–270. doi:10.1002/rcm.3113.

[40] A. Jaworek, A.T. Sobczyk, Electrospraying route to nanotechnology: An overview, J. Electrostat. 66 (2008) 197–219. doi:10.1016/j.elstat.2007.10.001.

[41] A. Jaworek, Micro- and nanoparticle production by electrospraying, Powder Technol. 176 (2007) 18–35. doi:10.1016/j.powtec.2007.01.035.

[42] L. Fei, S.H. Yoo, R.A.R. Villamayor, B.P. Williams, S.Y. Gong, S. Park, K. Shin, Y.L. Joo, Graphene Oxide Involved Air-Controlled Electrospray for Uniform, Fast, Instantly Dry, and Binder-Free Electrode Fabrication, ACS Appl. Mater. Interfaces. 9 (2017) 9738–9746. doi:10.1021/acsami.7b00087.

CHAPTER 2

BALANCING ELECTRICAL CONDUCTIVITY AND OXIDE GROUP CONTENT ON MESOPOROUS CARBON NANOFIBER INTERLAYER AS A POLYSULFIDE SUPPRESSOR IN LITHIUM SULFUR BATTERY

Abstract

The popularity of lithium-sulfur technology and graphene oxide have been surging following the rapid development of technology. High capacity and low cost of sulfur in conjunction with high surface area and intriguing chemical and mechanical properties of graphene oxide (GO) to enhance cell performance are subject to many scientific interests. In our experiment, GO was coated on mesoporous carbon nanofiber (MPCNF) to enhance polysulfide blockage. However, due to its insulating attribute, reduction of GO was essential to improve the electrical conductivity and cell performance. We scrutinized the impact of oxide content from GO and thermally reduced graphene oxide (rGO) as an additional interlayer on MPCNF with the performance of Li-S cells. As the temperature for heat treatment increased, the conductivity improved at the expense of dwindling oxide content. In our system, we found that optimum Li-S performance was achieved by heating the GO coated MPCNF at 300^{o}C under N_2 gas flow for 2 hours; furthermore, reduction at a higher temperature led to an inferior performance of Li-S cell due to insufficient oxide amount and weakened tensile strength of GO to hold polysulfide migration.

Introduction

Lithium-sulfur (Li-S) batteries have been a promising candidate for the next generation energy storage due to its five folds energy density and lower cost compared to lithium-ion battery (LIB) [1,2]. As the demand for energy storage increases due to steadily rising interest in electric vehicles (EV), portable electric devices, and the needs to store power for renewable energy, it is crucial to move beyond conventional LIB [3-5]. With only 150$/ton of sulfur on earth, Li-S technology has received many attentions from scientific and economic perspective [6,7]. The setback, however, including insulating property of sulfur, low sulfur utilization, dissolution of higher order polysulfide (Li_2S_x, x=4-8) into the electrolyte, and migration of polysulfide (PS) onto the anode material cause an irreversible loss of active materials, infinite charging, and poor capacity retention; hence stymies commercialization of Li-S technology [8, 9].

Since early 20's various attempts have been made to improve the performance of Li-S. For example, as reported by Nazar group, a bimodal porous carbon is mixed with sulfur materials to improve conductivity and sulfur utilization [10, 11]. This result has taken a huge leap in improving Li-S technology although many concerns still need to be addressed. Another method is adding $LiNO_3$ salt into the electrolyte to form protection film on the anode which improves the stabilization of redox reaction, however, after a long-term cycling the effect of surface passivation is compromised as the polysulfide reduction keeps bombarding the active material during discharge, consequently, a detrimental effect on the battery performance is inevitable [12-13].

Other approaches include surface functionalization [14-18], embedding an interlayer or depositing graphene oxide (GO), carbon nanotubes (CNT), double layer alumina protector [19-27] onto the separator. These approaches have been proven analytically to improve the capacity and cyclability of Li-S battery significantly in the past couple of years.

Embedding mesoporous carbon nanofiber (MPCNF) or graphene oxide as an interlayer has been a research hotspot owing to its large surface area and intriguing mechanical and chemical properties [21,22,25]. Previous studies by Manthiram revealed that CNF hinders the polysulfide migration during cycling due to its tortuosity, which helps increasing its capacity. However, as the cycles keep running, the polysulfides will inevitably escape the MPCNF and bombard the lithium anode, therefore reducing its efficiency at longer cycle [21,22]. Another approach is coating of GO on the separator [28,29]. It shows a higher performance compared to those without coating because of polar-polar interaction from the oxide group and polysulfide that enhance polysulfide trapping. However, the presence of GO in Li-S battery lowers the conductivity of the cell due to copious presence of insulating oxide group, which disrupts the sp^2 bonding network. Most of the time, the graphene oxide is reduced chemically or thermally to recover the honeycomb hexagonal lattice, hence increasing the electrical conductivity [30, 31]. Even with a high surface area, sometimes GO or reduced GO (rGO) break in the middle of discharge or charge cycle because the film is extremely thin, so it cannot handle the volume expansion of sulfur and polysulfide diffusion for longer cycle from continuous electrochemical reaction.

In our experiment, we coated GO layer on MPCNF interlayer using our novel air controlled electrospray method. By integrating tortuosity and oxide film property from GO and MPCNF, we improved the performance of the cell compared to pristine MPCNF. Then, the MPCNF coated GO is heat treated for 2 hours to reduce the oxygen content from carbon lattices and increased the conductivity to optimize the capacity and retention further. We explored the oxygen content, conductivity, and its repercussion on Li-S battery performances using GO and thermally reduced GO at various temperatures. The sulfur electrode was prepared via slurry coating with 1.1 mg cm^{-2} S loading. Electrochemical performance was conducted to investigate the impact of oxide content in the interlayer on cell capacity and retention.

Method

Synthesis of rGO coated carbon nanofiber (CNF) interlayer:

Preparation of MPCNF interlayer by air-controlled electrospinning method.

1.2 g of Polyacrylonitrile (PAN) (MW = 150,000 Sigma Aldrich), 0.8 g of polymethylmethacrylate (PMMA), 0.3 g of tetraethyl orthosilicate (TEOS), and 0.05 g of Zinc Chloride (ZnCl) were dissolved in 12 mL of dimethylformamide (DMF) to form 13.7 wt % of polymer content. The solution was stirred for 72 hours at 65ºC to enhance crosslinking polymer. Then, 6 ml of the polymer solution was air-controlled electrospun on an aluminum collector at 15 kV, 30 cm distance from the nozzle tip to the collector, 0.1 ml s^{-1} flow rate, and 12 psi airflow with 18 gauge stainless steel needle. After the process finished, the fiber was peeled and folded into the appropriate

size for heat treating. Initially, the fiber was subjected to stabilization at 280^{o}C for 2 hours with a ramp rate of 5^{o}C min^{-1}, followed by carbonization at 900^{o}C for 2 hours with a ramp rate of 5^{o}C min^{-1} under N_2 flow, and finally activation at 900^{o}C for 2 hours with a ramp rate of 5^{o}C min^{-1} under CO_2 flow.

Preparation of thermally reduced GO on MPCNF interlayer:

Graphene oxide solution from Kisco corp was diluted to 6 mg ml^{-1}. 5 ml of the solution was extracted and sprayed onto activated MPCNF substrate using air control electrospray at 25 kV, 30 cm distance from the nozzle tip to the collector, 0.1 ml s^{-1} flow rate, and 20 psi airflow with 18 gauge stainless steel needle. After spraying, the surface color of the MPCNF turned into a dark grey, indicating successful coating of GO on MPCNF. Each sample was heat treated at 300^{o}C and 500^{o}C under N_2 flow for 2 hours and became reduced graphene oxide (rGO) on MPCNF substrate. After heat treatment, the rGO side had a silverish or light grey color. The retrieved MPCNF-rGO sample was punched into several 1.5 cm diameter coin cells and weight approximately 4-5 mg cm^{-2} with 200-300 µm thickness.

Deposition of Sulfur Electrode and Cell assembly:

The deposition of sulfur material was prepared via slurry coating method. 56% of the active sulfur material, 32% of mesoporous carbon (super p), and 12% of PVDF solution (10% weight percent in NMP solvent) were mixed in a ball mixer for 30

minutes. Then, the slurry was coated on top of the aluminum collector with 200 µm gap doctor blade. Next, the sample was dried in a 60^{o}C oven for 24 hours to evaporate the solvent. Finally, the electrode was punched into coin cells size (diameter = 1.75 cm), with the typical sulfur weight of 1.2 mg cm^{-2} and ready for assembly.
The electrolyte was 1 M lithium bis(trifluoromethanesulfonylimde) (LiTFSI) in 1,2-dimethoxyethane and 1,3-dioxolane (DME-DOL 1:1 v/v) containing 0.1 wt.% $LiNO_3$ additive. CR2032 coin cells were assembled in an argon-filled glove box with the sulfur cathode, interlayers (MPCNF, MPCNF+GO, or MPCNF + rGO), celgard separator, Li metal foil, and spacer in sequence.

Testing and characterization:

X-ray photoelectron spectroscopy (XPS) and Raman spectra were conducted to characterize the reduction of graphene oxide and polysulfide adsorption. SEM was performed to observe the morphology and structure of MPCNF, GO, and rGO at 300^{o}C and 500^{o}C before and after cycling 100 times. Cyclic Voltammetry (CV) with a scan rate of 0.1 mV s^{-1} and Electrochemical Impedance Spectroscopy (EIS) were performed to measure the redox reaction and charge transfer resistance of the cells. Galvanostatic charge/discharge tests were carried out on MTI battery testing system at various rates.

Result and Discussion

The synthetic route to obtain mesoporous carbon nanofiber (MPCNF) substrates and interlayers is shown in illustration 2.1. The polymer solution (core part) and air gas (shell part) were introduced into a coaxial nozzle concurrently. Prior to this work, we successfully developed the gas-assisted electrospinning process which increases the production of nanofibers because convective air flow provides additional drag force to the polymer jet. Thus, fast flow rate of polymer solutions can be applied during the spinning process. After the heat treatment, the MPCNF matt for interlayer was obtained.

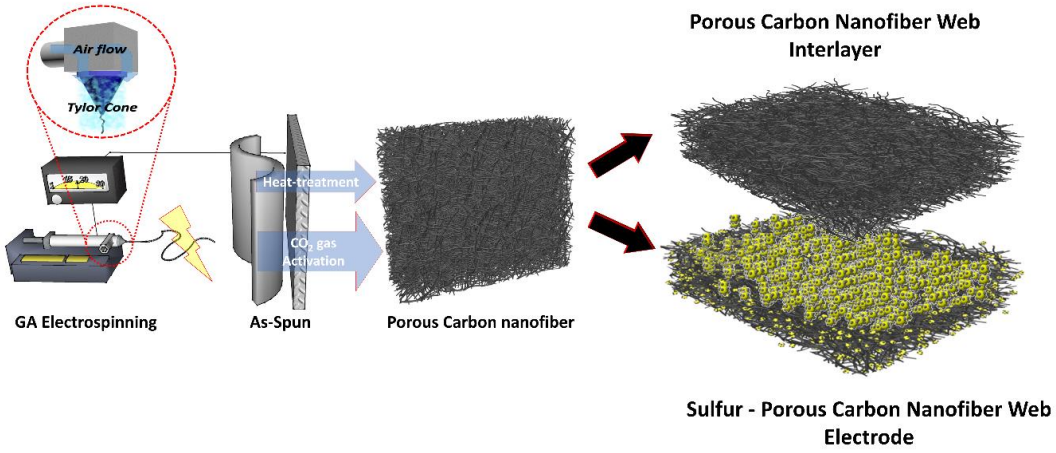

Illustration 2.1) Schematic illustration of preparing MPCNF matt for Li-Sulfur batteries

We implemented the free-standing MPCNF interlayer as our reference. The MPCNF was created by embedding sacrificial polymer (PMMA) in the polymer solution to create micropores structure during the activation step. In our system, the thickness of

the MPCNF interlayer was around 200 µm and weight around 8 – 10 mg. Braunauer-Emmett-Teller (BET) technique was used to observe the BET surface area and pore size distribution of mesoporous carbon nanofiber (Fig. 2.1). The MPCNF after carbonization and activation had a specific surface area of 292 m^2g^{-1} and 802 m^2g^{-1} respectively. After activation, we noticed that the specific surface area and micropores to mesopores ratio were significantly improved after CO_2 activation, which technically improved the surface adsorption sites for the polysulfides.

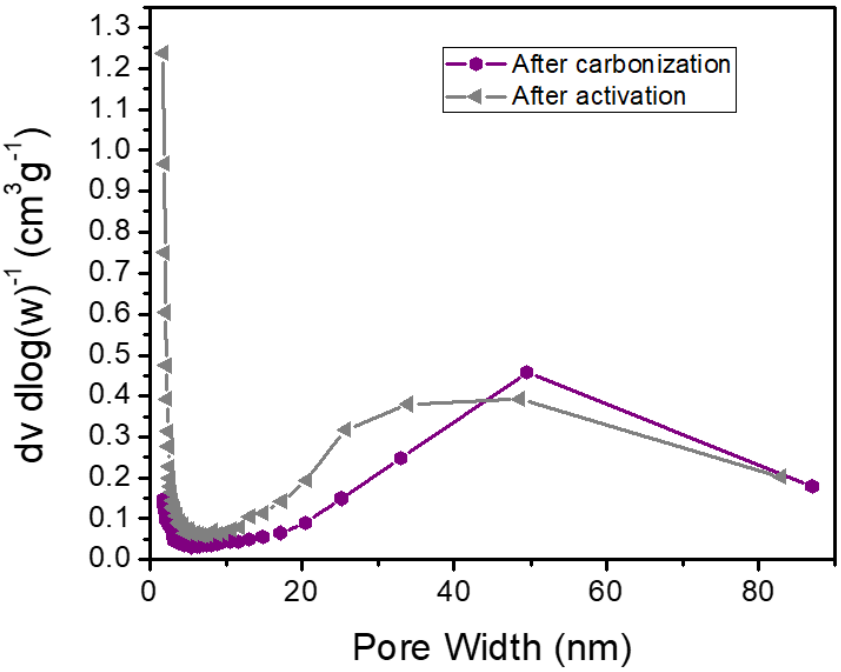

Figure 2.1) BET result of MPCNF interlayer before and after CO_2 activation.

GO is a polar material and bears a negative charge due to numerous oxygen content functional group (hydroxyl (OH) and carboxyl (COOH) groups). The weight of graphene oxide was less than 0.5 mg in total, which was less than 6% of the total interlayer mass. The illustration of our Li-S battery by utilizing GO coated MPCNF

(MPCNF+GO) was shown in Fig 2.2 below. From the SEM images, we were unable to determine the thickness of GO from the cross-section SEM images, which implied that either the GO sprayed layer was very thin or fused and indistinguishable with the MPCNF during gas assisted electrospray by looking at the cross-sectional area.

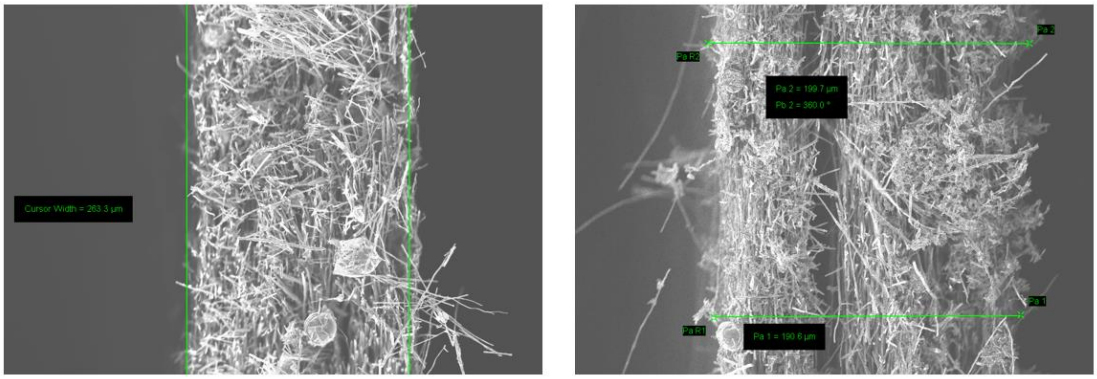

MPCNF+GO MPCNF+rGO300

Figure 2.2) Cross-section MPCNF on coated GO images. Before heat treatment (left) and after heat treatment at 300°C (right)

The cell was assembled by facing the GO layer to the sulfur cathode as shown in illustration 2.2. Then illustration 2.3 depicts all the MPCNF along with the GO layer before and after reduction. Before reduction, it showed a dark grey color and wrinkled on the GO surface. After the reduction by heat treatment at 300°C (MPCNF+rGO300) or 500°C (MPCNF+rGO500) in N_2 gas flow, the color of GO film turned into light gray and smoother surface was observed. For the convenience of this report, we define reduced GO (rGO) as being thermally treated under N_2 flow at designated temperature for 2 hours.

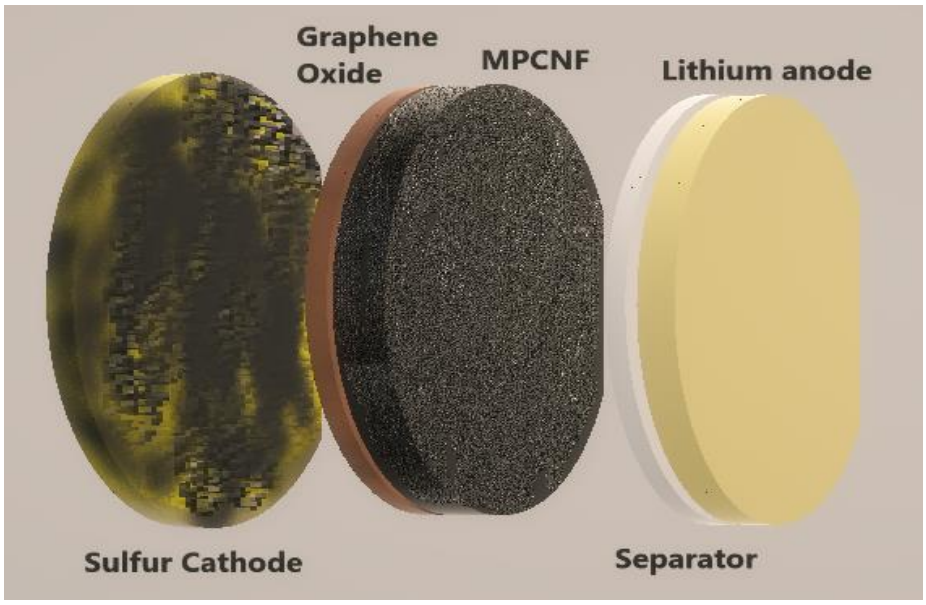

Illustration 2.2) The illustration of GO coated MPCNF interlayer system

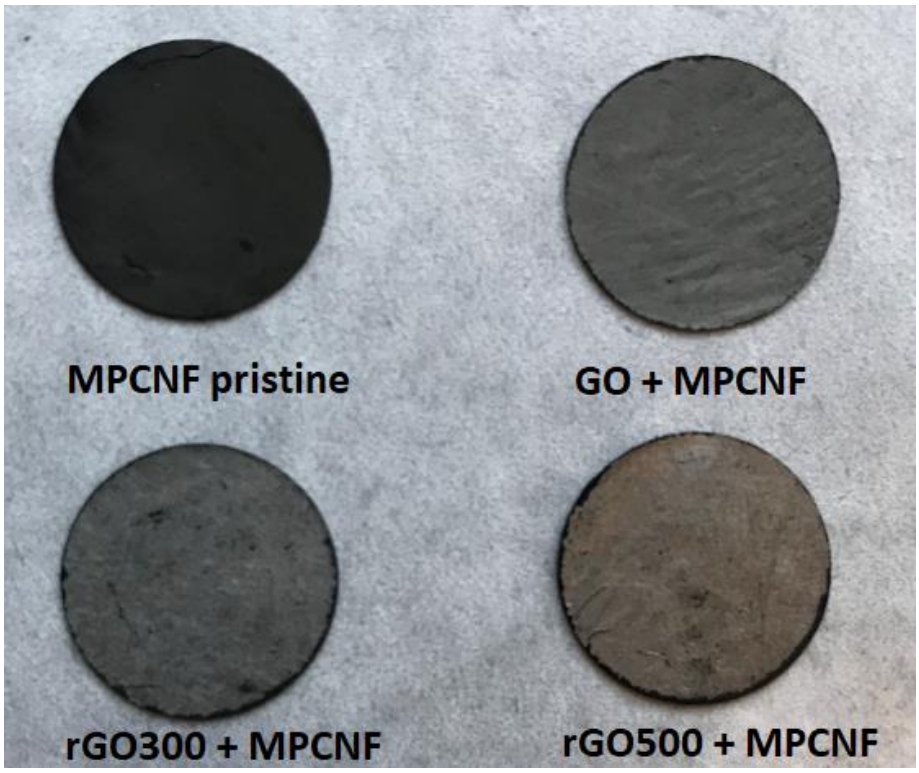

Illustration 2.3) The images of uncoated MPCNF and GO coated MPCNF before and after reduction at 300^{o}C and 500^{o}C

XPS measurement was conducted to elucidate the graphene oxide reduction (Fig 2.3). Based on the survey scan, the ratio of carbon to oxygen ratio increases as the temperature increases. The C:O ratio at each reduction temperature was summarized in Table 2.1. Conclusively, more oxygen content dwindled at higher heat treatment temperature. High resolution in situ XPS (Fig 2.4) shows that C 1s region of graphene oxide was assigned to 3 components: C=C or C-C at 284 eV, C-OH at 286 eV, and C=O at 289.5 eV (Fig 1.5) [32-36]. A clear shift in the XPS bands towards higher binding energy (284.9 eV) for GO was observed, implying a significant surface charging due to the electrically insulating nature of GO [37]. After the reduction of GO at 300^{o}C in N_2 flow the binding energy of carbon atoms C-O and C-C shifted to lower energy by 0.6 eV, entailing the improvement in electrical conductivity of GO layer, and the ratio of relative intensity C-C: C-O stays at 1: 1.2. After further reduction to 500^{o}C, the relative intensity ratio of C-C: C-O group increased to 2: 1, which implies the dehydrogenation and deoxygenation from carbon planar [15,35]. Also, the binding energy of C-O peak shifted by 0.5 eV to lower binding energy, while C-C binding peak remained at 284.4 eV, suggesting an improvement in the electrical conductivity. Overall, our survey scan and high-resolution C^{1S} XPS results show agreement with the literature [38–41].

Raman spectroscopy also serves an important role for characterization because it provides additional evidence for the reduction of GO (Fig 2.5). Raman spectra on GO exhibits two broad peaks at 1316 cm^{-1} and 1584 cm^{-1}. The D band is attributed to defects, reflecting the level of disorder edges in rGO domain and the G band is ascribed to the vibration of sp^2 hybridized carbon atoms in a 2D hexagonal lattice [42].

Initially, GO had I_D/I_G ratio of 1.214 (Table 1). After exposing at 300^{o}C for 2 hours, a slight increase in the D peak intensity was observed, with I_D/I_G ratio increased to 1.25, signifying oxygen functional groups had been removed and a larger number of defects and disordered edge were introduced during heat treatment [43, 44]. Then, further reduction at 500^{o}C rapidly increased the I_D/I_G to 1.36, reflecting more disordered and defects in the GO layer. Naturally, a decrease in I_D/I_G ratio is expected upon reduction of GO because the disorder associated with oxygen defects diminishes. Our experimental observation suggests that carbon honeycomb lattice is partially restored, but forced removal of oxygen at higher temperature leads to more creation of strains and topological defects on the sp^2 sites [35,45,46]

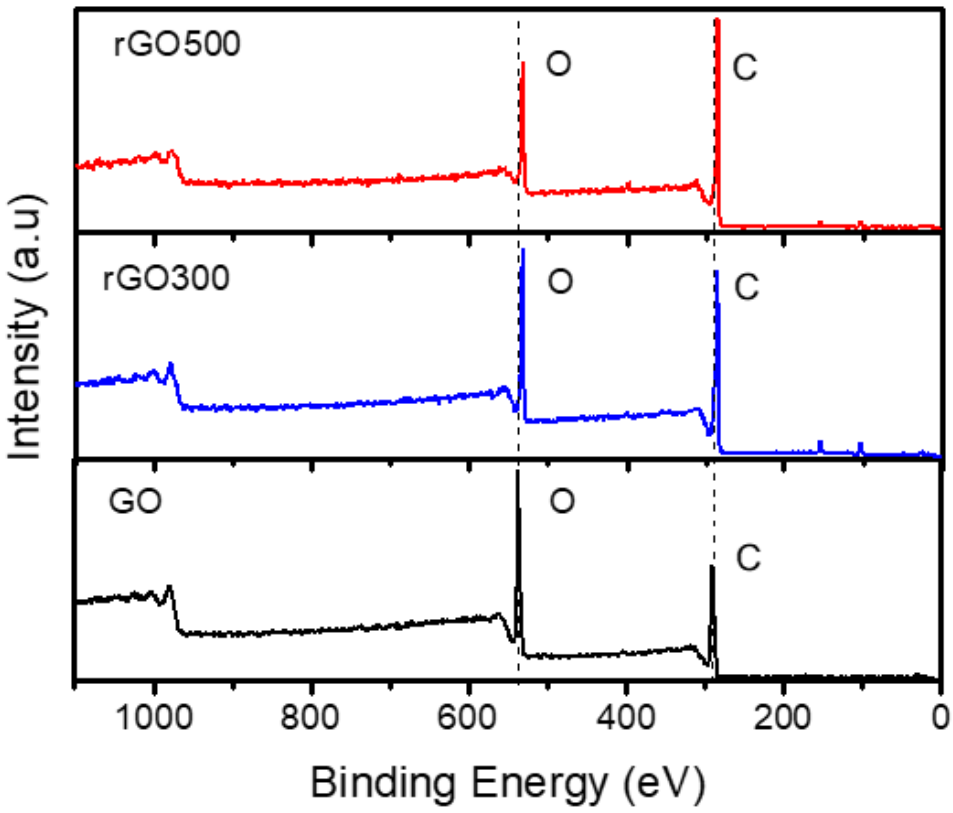

Figure 2.3) XPS survey scan of pristine GO and rGO at different temperatures

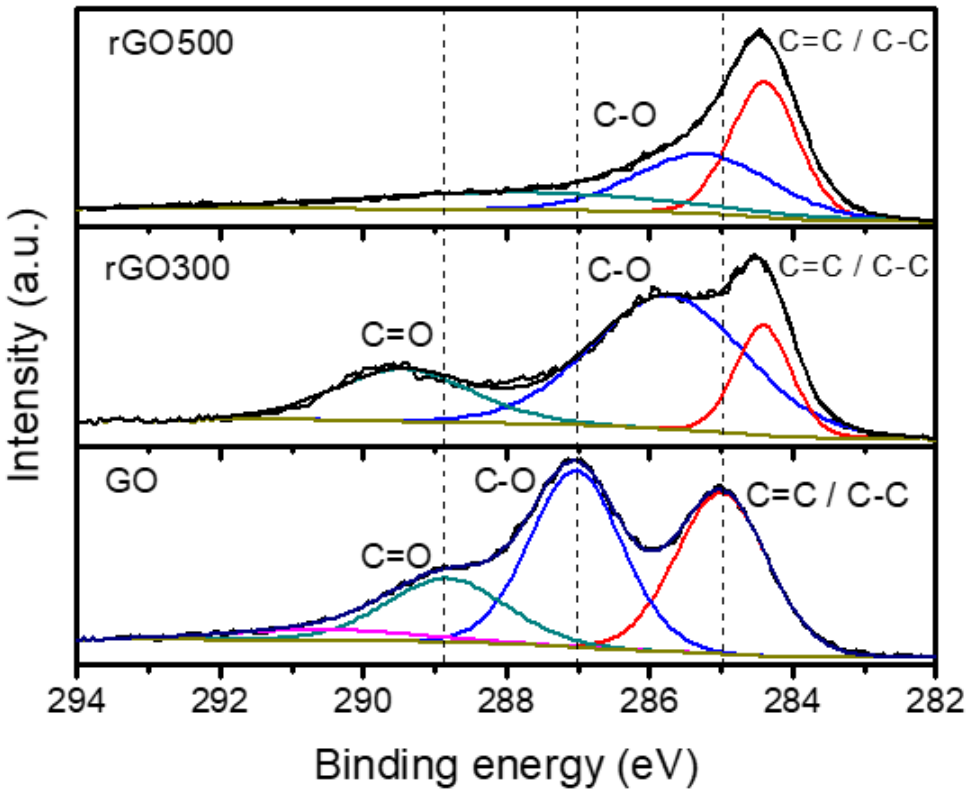

Figure 2.4) High resolution XPS of pristine GO and rGO at different temperatures

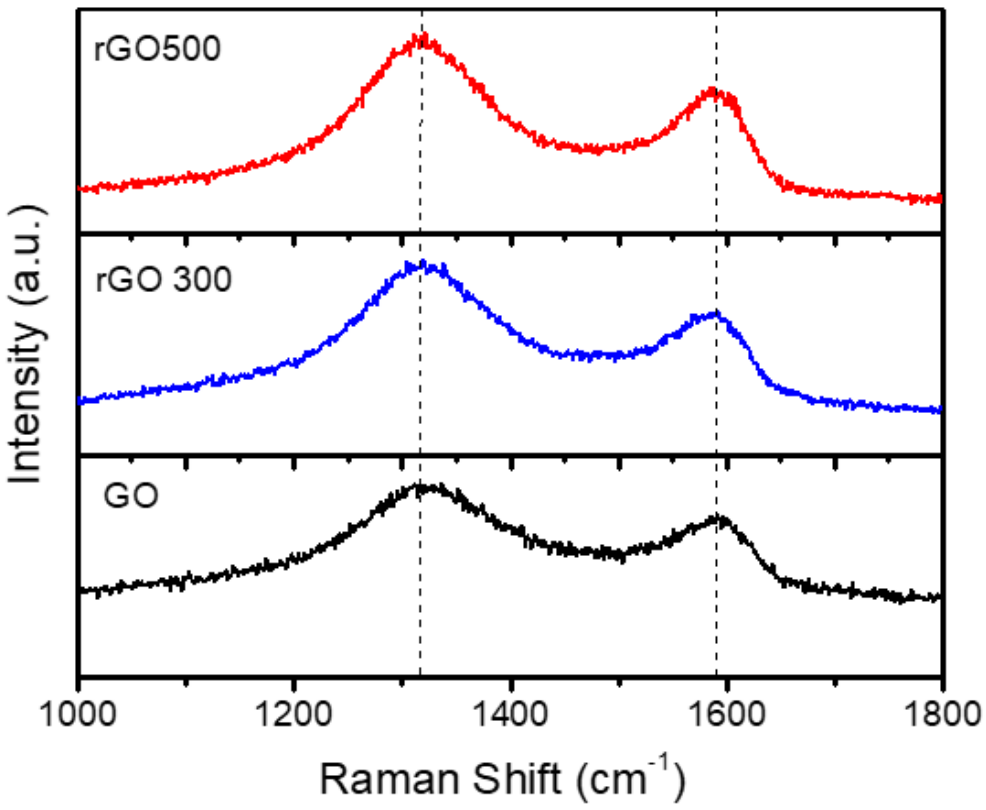

Figure 2.5) Raman spectra of pristine GO and rGO at different temperatures

Table 2.1 Carbon to oxygen ratio from survey scan XPS and I_d/I_g ratio from Raman spectra

Samples	C : O ratio	I_d/I_g ratio
GO	65 : 35	1.214
rGO300	73 : 27	1.25
rGO500	78 : 22	1.36

The redox reaction on each interlayer is demonstrated by cyclic voltammetry (CV) test (Fig 2.6). CV scan was performed between 2.8 and 1.6 V at 0.1 mV s^{-1} scan rate. All samples showed two reduction peaks around 2.2V and 1.9V, corresponded to the redox reaction of high order polysulfides (s_6^{2-}, s_4^{2-}) and lower order polysulfide (S^{2-} or S_2^{2-}) respectively [48]. The oxidation peak was also observed at around 2.6V. All samples have a similar magnitude of oxidation and reduction peak. However, uncoated MPCNF interlayer showed a gradual decline in the reduction peak; moreover, the cell started operating at 2.5 V instead of 2.8 V or higher as opposed to the rest of the cells, indicating the possibility of polysulfide self-diffusion and lack of polysulfide adsorption in the MPCNF interlayer. In contrast, the sharpest peak and superior stability were displayed on MPCNF+rGO300, which represents higher sulfur utilization and excellent adsorption of the polysulfides.

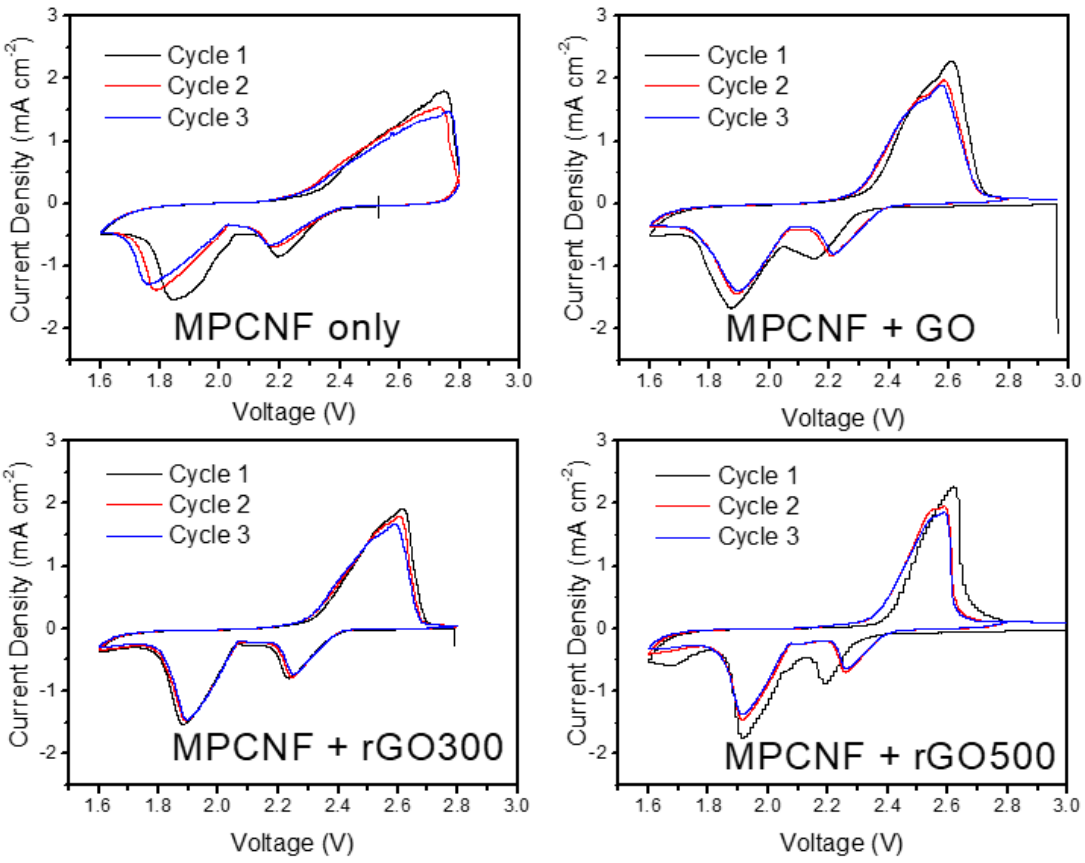

Figure 2.6) Cyclic voltammetry test on various interlayers

In general, the presence of graphene oxide lowers the conductivity of the cell. The EIS of the cell showed that the charge transfer resistance increased by 400% when GO layer was implemented on the MPCNF interlayer, presumably due to myriad oxide group stretching from the carbon planar (Fig 2.7). Electrical conductivity is a critical factor for the battery to perform well, because high internal resistance causes the battery to build up heat faster and rapid drop of voltage under load, triggering an early shutdown. After MPCNF+GO was reduced at 300^{o}C, the charge transfer resistance declined by approximately 20%, and further reduction at 500^{o}C lead the semicircle to shrink further. Therefore, increasing heat treatment temperature improves electrical conductivity.

The sulfur electrodes are tested with four different interlayers: MPCNF, MPCNF+GO, MPCNF+rGO300, and MPCNF+rGO500 (Fig 2.8). The electrochemical performance of pure sulfur cathode is evaluated at 0.5C (1C = 2.0 mA cm^{-2}) from 2.8V to 1.8V. The sulfur loading electrode delivered stable capacity until 100^{th} cycle. Immediate observation from the cyclability data shows that MPCNF+rGO300 interlayer achieves the highest capacity and retention among the samples. The presence of GO in the system should improve the cell performance compared to freestanding MPCNF due to the presence of oxide group that enhances the adsorption due to polar-polar interaction, but the insulating property of GO hinders the electron pathway and lowering the sulfur utilization [28, 30]. Interestingly, a further temperature increase of GO presented detrimental effect on the system, which possibly due to an insufficient amount of oxide group to capture the polysulfide or frail tension of rGO layer after extra stress imposed at a higher temperature.

The initial capacity of free-standing MPCNF interlayer was 1164 mAh g^{-1} , which then dropped to 914 mAh g^{-1}. Following rapid decay over 20 cycles, the reference cell reached reversible capacity at 716 mAh g^{-1} with 0.25% capacity fading per cycle. By coating the MPCNF with GO interlayer, MPCNF+GO improved the initial capacity to 1307 mAh g^{-1}, which then plummeted to 1015 mAh g^{-1}; the capacity declined at 0.9% per cycle for the next 25 cycles. The reversible capacity was obtained at 722 mAh g^{-1} with 0.19% capacity fading each cycle. The MPCNF+rGO300 interlayer exhibited the highest capacity and the most durable retention rate in our system. Initially, the discharge capacity was achieved at 1216 mAh g^{-1} which then dropped to 1022 mAh g^{-1}, achieving reversible capacity each cycle at a fading rate of 0.13%. Increasing the temperature of graphene oxide over 300^{o}C caused an inimical effect on the cell performance. The initial capacity using MPCNF+rGO500 interlayer was 1039 mAh g^{-1}. The capacity declined swiftly and stabilized at 500 mAh g^{-1}, and the capacity slowly decayed at 0.3% each cycle.

From the rate capability test, immediate observation can be noticed by looking at the gap of MPCNF+GO and MPCNF or MPCNF+rGO500 at 1C (Fig 2.9). While MPCNF and MPCNF+rGO500 deliver around 200 mAh g^{-1} at 1C, MPCNF+GO and MPCNF+rGO300 deliver 3x higher discharge capacity at around 550 mAh g^{-1} and 650 mAh g^{-1} respectively. When the current rate is amplified to 2C, MPCNF and MPCNF+rGO500 interlayers are unable to attain any capacity, whereas MPCNF+GO and MPCNF+rGO300 manage to accomplish 150 mAh g^{-1} and 250 mAh g^{-1} subsequently. Above all, the rate capability shows similar patterns with cyclability,

with MPCNF+rGO300 achieves the highest capacity, follows by MPCNF+GO, MPCNF, and MPCNF+rGO500.

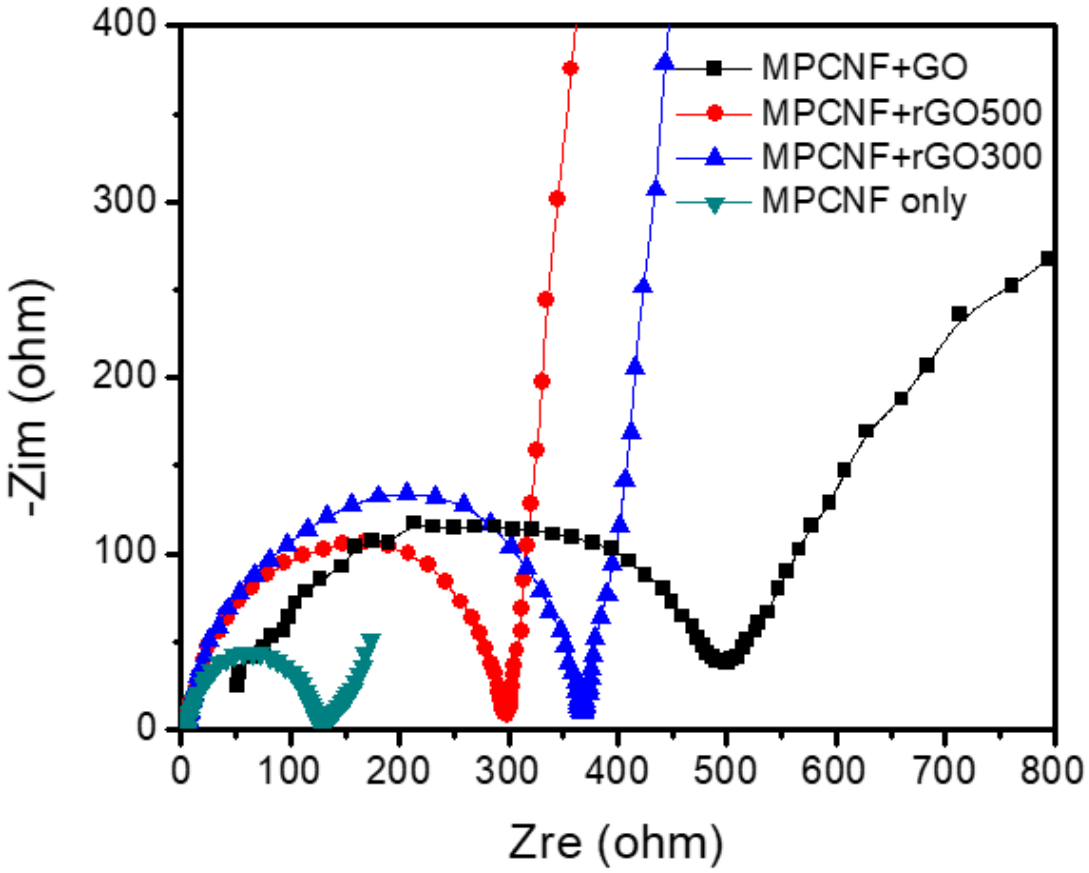

Figure 2.7) Electronic Impedance Spectroscopy on various interlayers

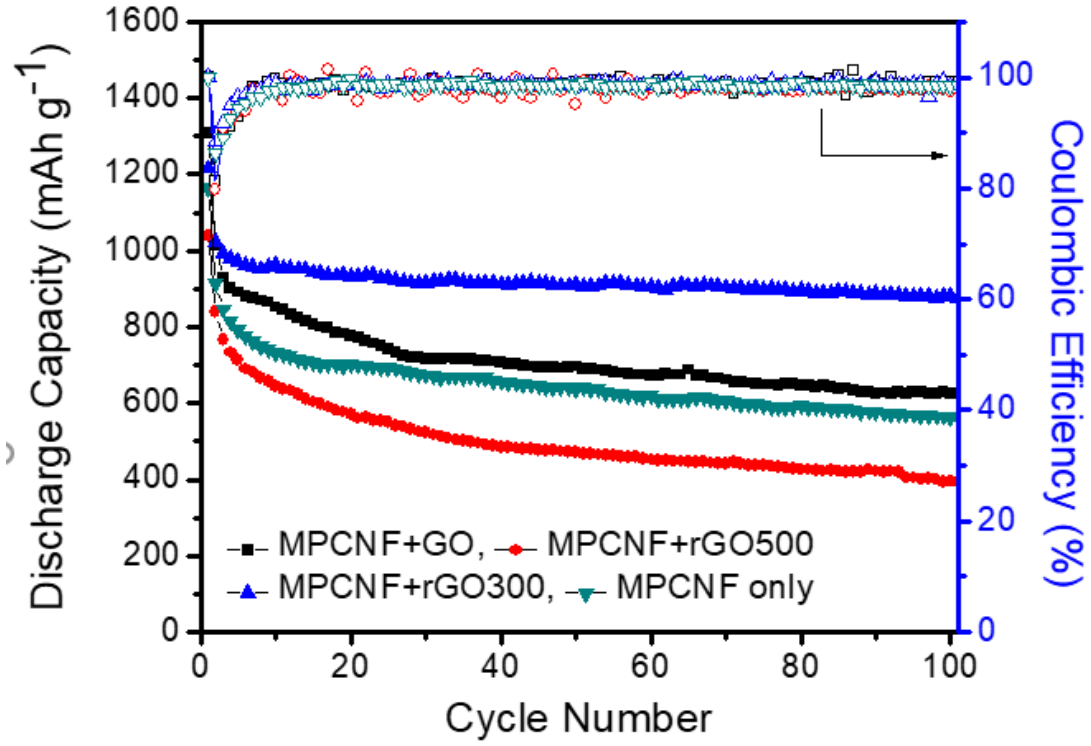

Figure 2.8) Electrochemical performances of the cells with various interlayers at 0.5 C rate (1C – 1670 mA g^{-1}).

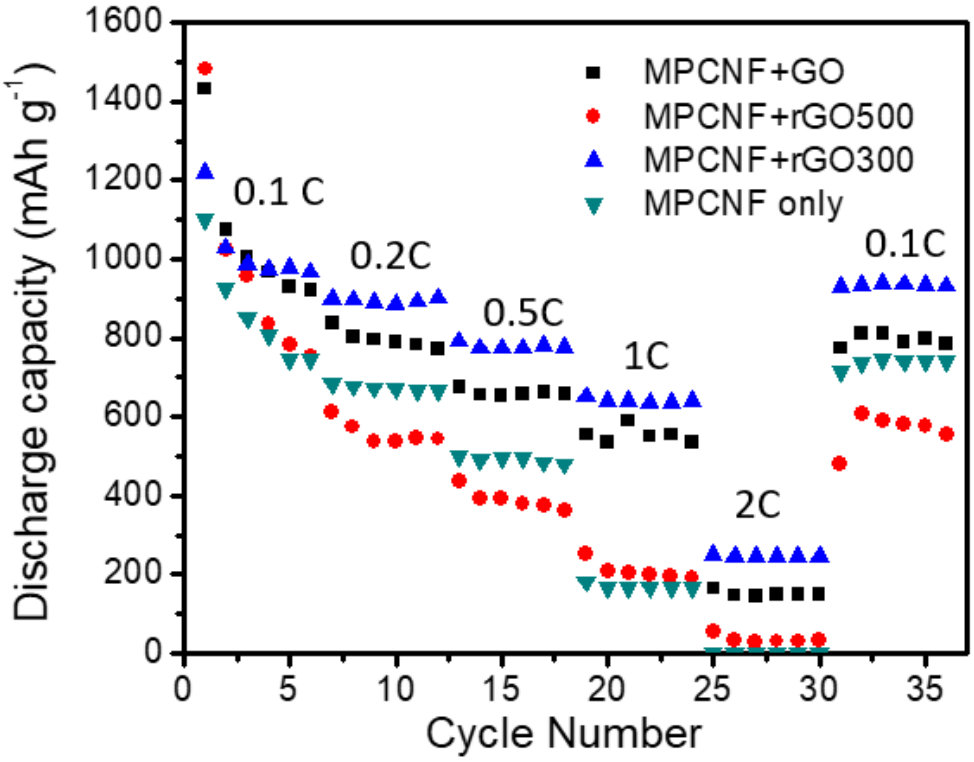

Figure 2.9) Rate capability of cells with four different interlayers

Scanning electron microscope (SEM) was conducted to signify the role of interlayers in trapping the polysulfide diffusion. Morphologies of MPCNF, MPCNF+GO, MPCNF+rGO300, and MPCNF+rGO500 interlayers were presented before cycling (Fig 2.10a-d). By coating the MPCNF with GO, the rift between carbon networks was filled with web structure film. GO layer displayed a rough and dense layer. After heat treatment at 300^{o}C, the surface became slightly smoother, and further heat treatment at 500^{o}C showed a leaf-like structure in the rGO morphology. The carbon fibers that were protruding from the surface resembles leaf' midrib and its vein. Next, the structure after 100 cycles on each interlayer was presented on the front side and back side to compare the diffusion of polysulfide through carbon nanofiber framework (Fig 2.11a-d). The front side SEM of MPCNF displayed the absence of polysulfide existence, indicating poor adsorption of polysulfide. As the tortuosity only delays the shuttle effect, polysulfide escapes at longer cycling are inevitable. Looking at MPCNF backside, the void implies the withdrawal of polysulfide from the MPCNF network. The clogging is improved by GO coating. MPCNF+GO showed an accumulation of sulfur on the surface, and the backside also shows a rife of the sulfur component even after 100th cycle, implying excellent trapping within the interlayers. By scrutinizing the morphology on rGO300 interlayers, nuclei formations were observed in the surface of rGO300, implying a complete reaction to lower order polysulfides. Moreover, the backside was completely covered with sulfur material as the one with GO, showing an exquisite adsorption to accommodate the polysulfides in the interlayer. On the rGO500 surface, meticulous observation displayed disseminate wreckage in graphene oxide layer (Fig 2.12). Some of the structure still intact, and big

lumps of sulfur aggregated on rGO500 surface. The rift implies a deterioration in the tensile strength of GO layer after heat treatment at a higher temperature. By observing the backside morphology of the MPCNF (Fig 2.13a-d), the polysulfide coverage is not as dense as MPCNF+GO or MPCNF+rGO300, or maybe even worse than pristine MPCNF. This evidence provides an assertion of inferior capacity and retention of MPCNF+rGO500

interlayer.

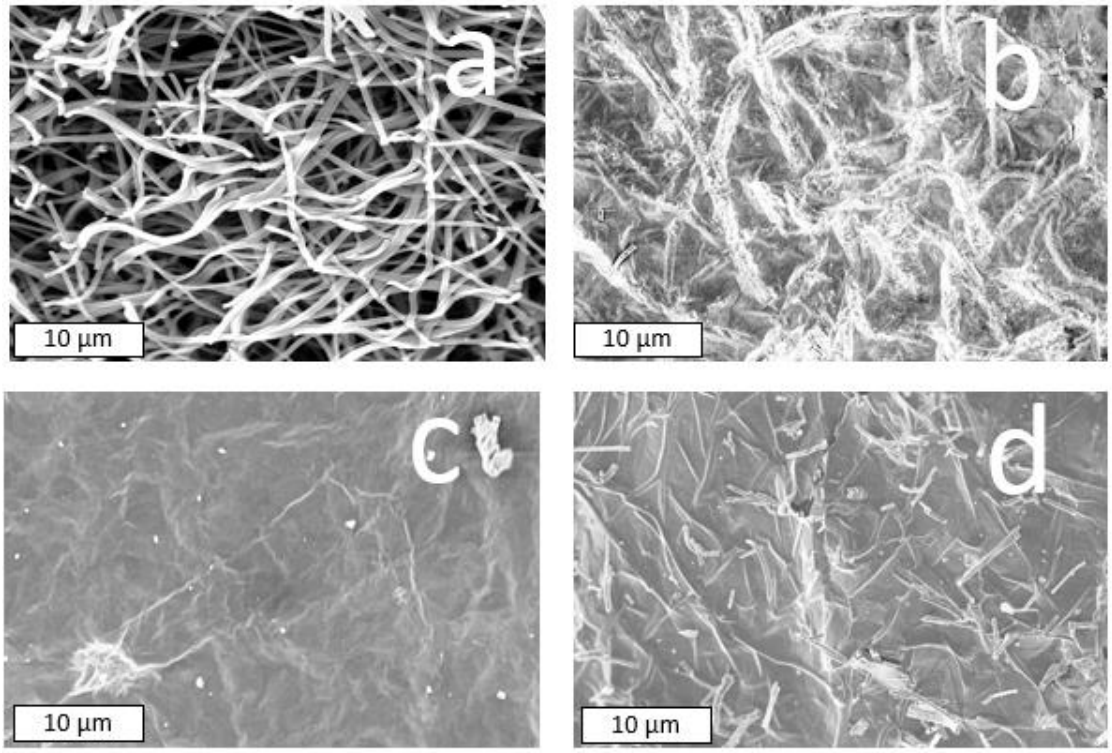

Figure 2.10) The SEM images of a) MPCNF b) MPCNF+GO c) MPCNF+rGO300 d) MPCNF+rGO500 before cycling.

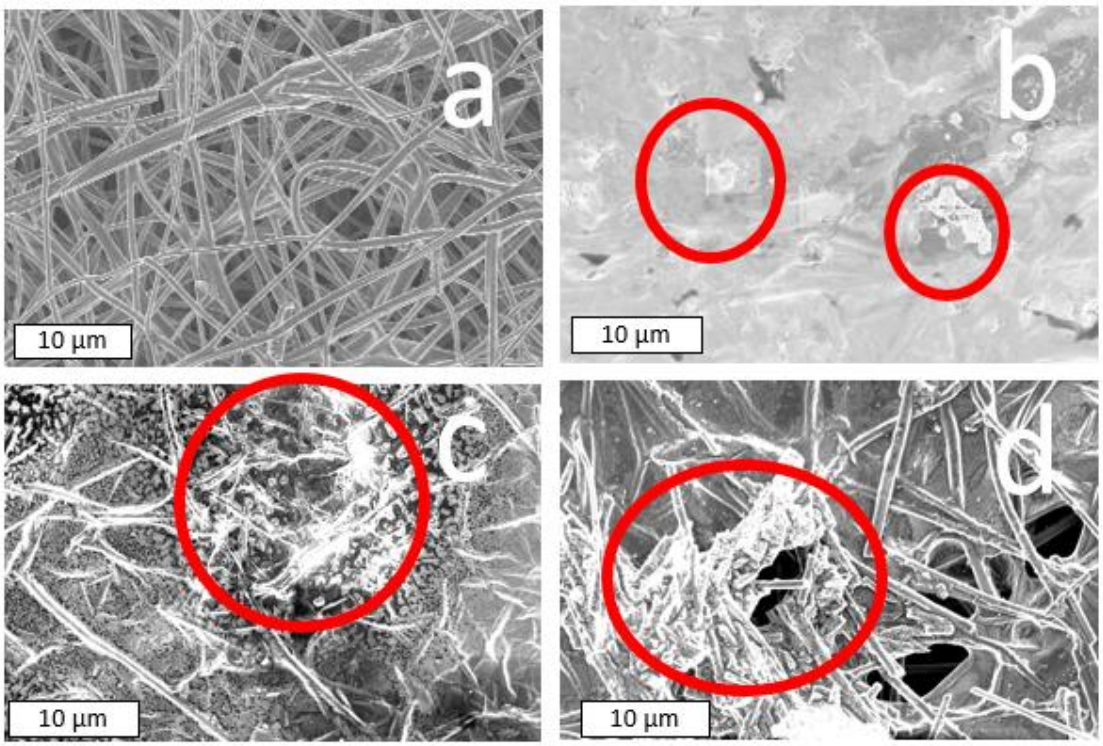

Figure 2.11) The SEM images of a) MPCNF b) MPCNF+GO c) MPCNF+rGO300 d) MPCNF+rGO500 after cycling facing sulfur cathode. The aggregated polysulfide existences were marked with red circles.

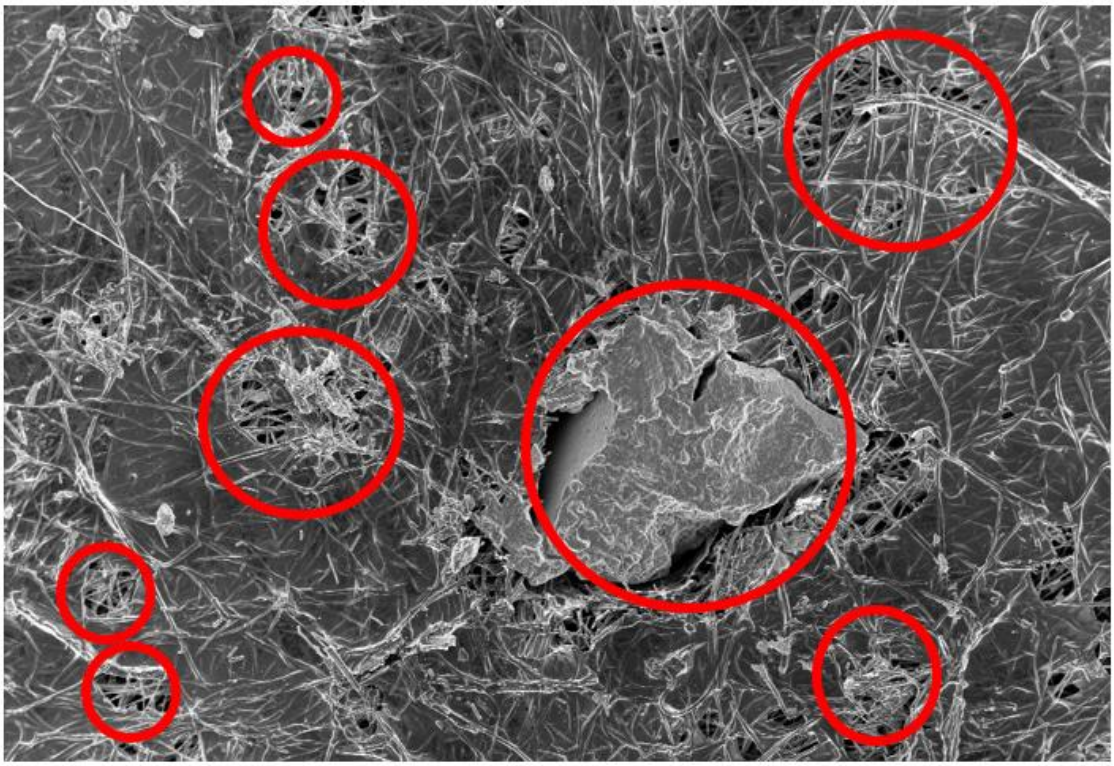

Figure 2.12) Lower magnification of SEM images for MPCNF+rGO500 after cycling facing sulfur cathode. The aggregated polysulfide existences were indicated by red circles.

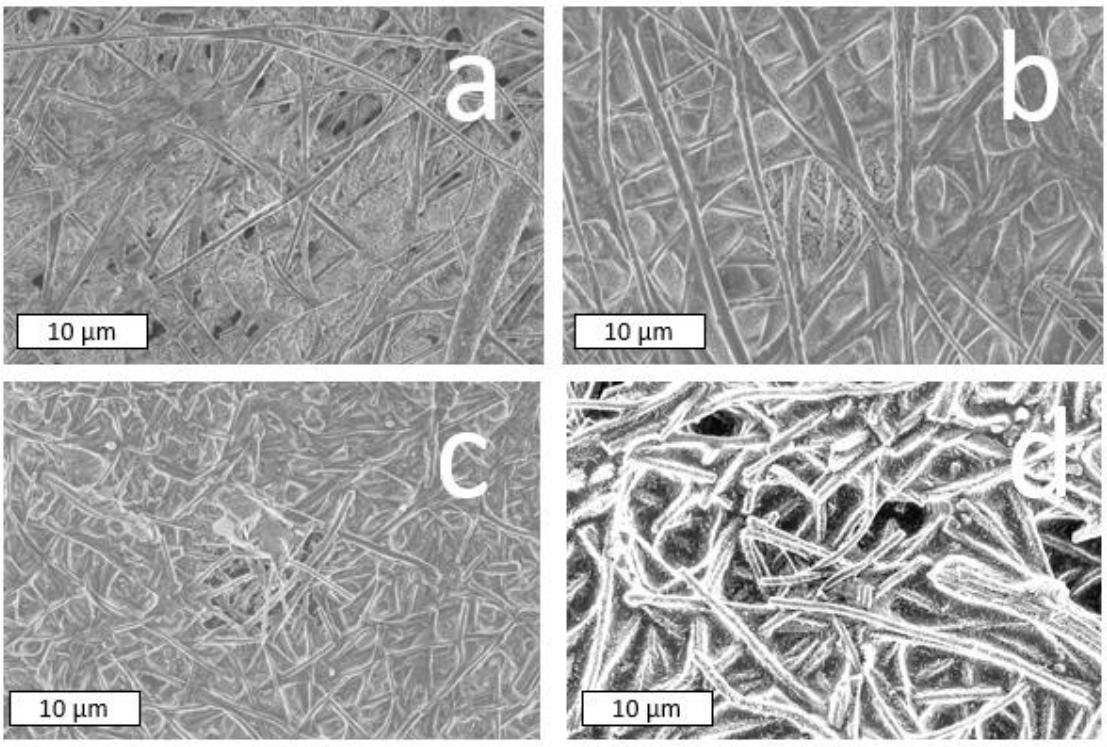

Figure 2.13) The SEM images of a) MPCNF b) MPCNF+GO c) MPCNF+rGO300 d) MPCNF+rGO500 after cycling facing separator.

High-resolution spectra on Sulfur S^{2p} was investigated to clarify the adsorption of polysulfides (Fig 2.14). The test was conducted on all samples after finished cycling. The graph shows a small broad peak at 163 eV for MPCNF+GO and MPCNF+rGO500, and a relatively medium peak at 162.5 eV for MPCNF+rGO300. The peaks correspond to the presence of insoluble polysulfides [49]. These phenomena demonstrate the existence of a polar-polar interaction between oxide group and polysulfides. Also, no significant peak was observed on MPCNF interlayer, which showed the lack of interaction between carbon fiber and polysulfide. To extend the analysis, we perform high-resolution spectra two weeks after the sample finished cycling (Fig 2.15). MPCNF+GO and MPCNF+rGO300 presented small bumps at 164 eV. However, no peak was observed at similar binding energy for MPCNF, and perhaps subtle peak was present for MPCNF+rGO500 by observing thoroughly. Conclusively, no significant polysulfide peak was present because the soluble polysulfide reacted with the atmosphere and detachment of remaining insoluble polysulfide due to sluggish binding force with the interlayer. Considering a small peak still present after a long period of inactivity after cycling, it entails superior polar-polar interaction between oxygen group and lithium polysulfide.

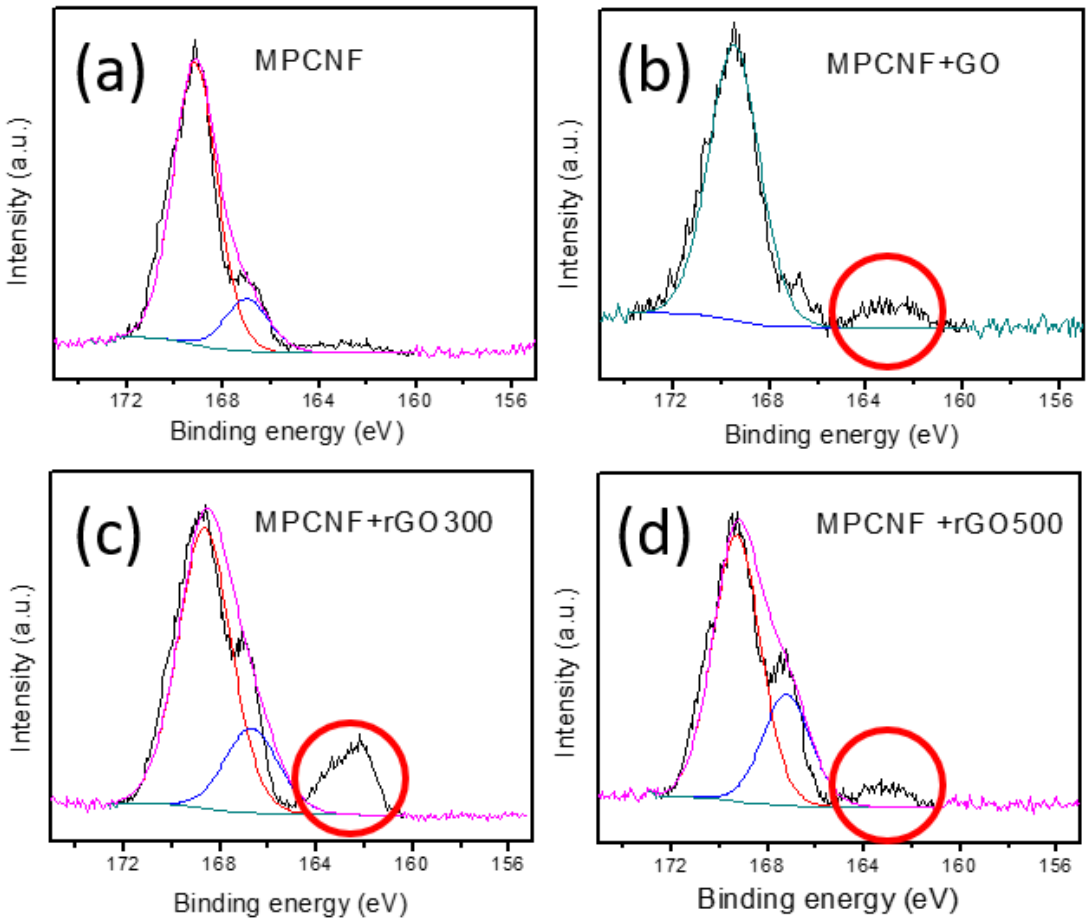

Figure 2.14) High resolution in situ XPS of S^{2p} after cycling. Polysulfides peaks were marked with red circles.

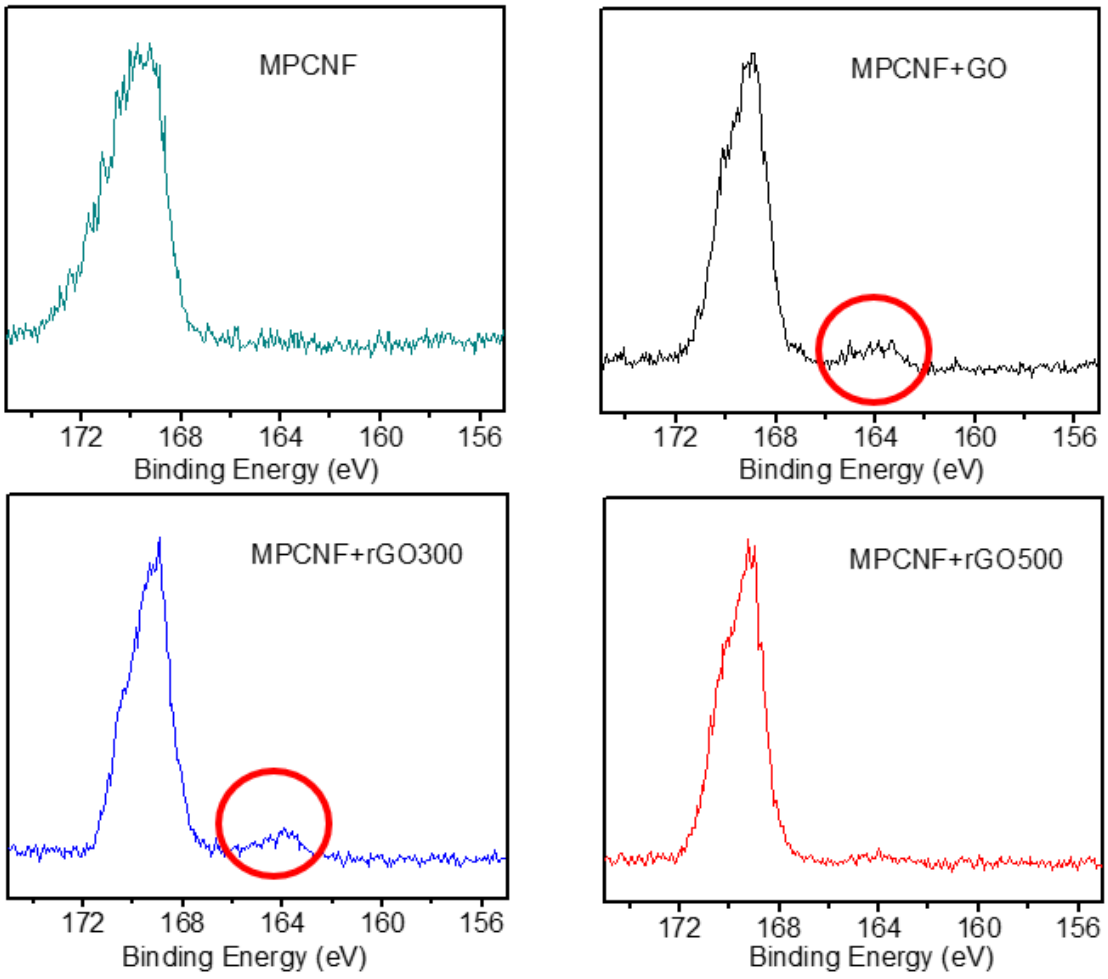

Figure 2.15) High resolution in situ XPS of S^{2p} two weeks after cycling. Polysulfides peaks were marked with red circles.

The polar-polar interaction between oxide group from GO or rGO and polysulfides are elucidated from high-resolution spectra on S^{2p} XPS. This fact provides assertion on superior performance by rGO300 compared to others. An excellent harmony exists between polar host oxide group and carbon sp^2 network. Higher sulfur utilization and ample oxide group to instantly capture polysulfide are leading to higher capacity and outstanding retention for at least 100 cycles. On the contrary, poor performances by MPCNF+rGO500 interlayer is suggested by insufficient oxygen group to adhere polysulfides, which demonstrated the lack of polysulfide peak after two weeks, and higher resistivity compared to conventional MPCNF interlayer. SEM images on MPCNF+rGO500 after cycling displayed ruptures disseminate across rGO surface, implying dissatisfactory mechanical strength to contain sulfur expansion and migration.

The implementation of proper content of oxide group is considered beneficial to revamp the performance of lithium-sulfur battery. By combining tortuous path from MPCNF interlayer and additional attraction force from reduced graphene oxide, most of the polysulfide remain in the interlayer even after 100 cycles (Illustration 2.4). This propitious integrated interlayer system greatly mitigates the shuttle effect and showing a favorable prospect to the commercialization of Li-S battery. However, the more advanced system is required for Li-S battery to compete with conventional Li-ion battery at similar volumetric energy density, such as high loading sulfur and lesser or thinner inactive material like interlayer and mesoporous carbon. Ultra-high loading sulfur (18.1 mg cm^{-2}) investigation that was conducted by Manthiram demonstrates a prominent figure in a high loading sulfur community [49]. Incorporating high sulfur

content by the proper balance of oxide content from carbonaceous material or metal oxide would be an interesting topic to explore.

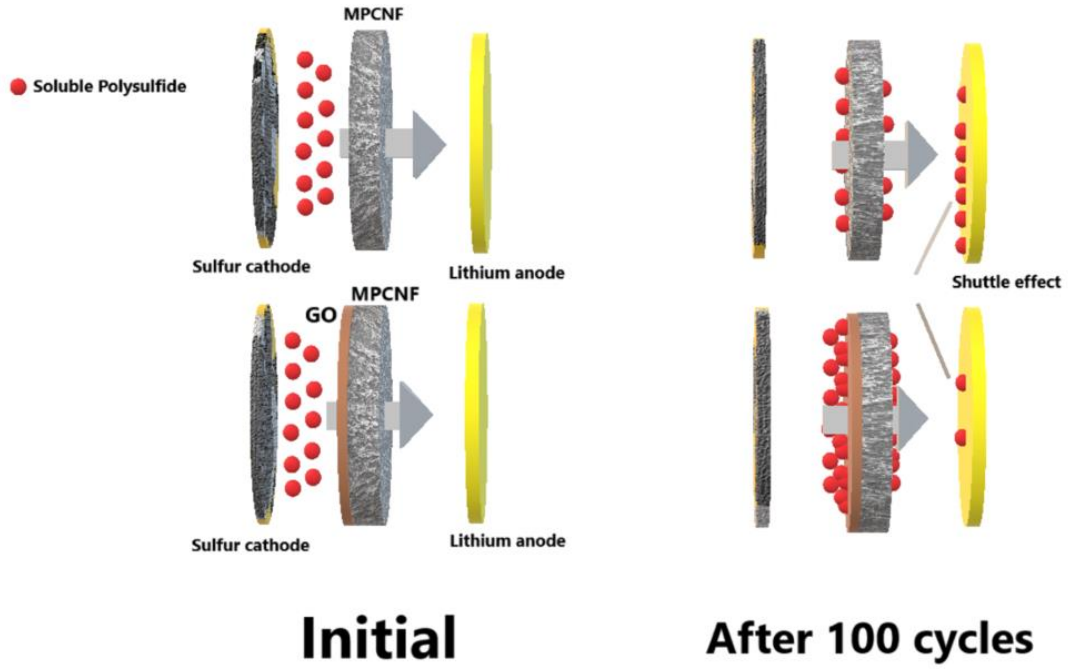

Illustration 2.4) The illustration of interlayer with graphene oxide role in blocking polysulfide.

Conclusion

We successfully improve the discharge capacity and retention by adding additional rGO layer from conventional MPCNF interlayer via air-controlled electrospray method. In general, air controlled electrospray enables coating on various surface. Our investigation shows that proper oxide content and conductivity are critical factors in achieving high capacity and durable Li-S battery. Heat treatment is one way to adjust the oxygen content of graphene oxide. High oxide content will decline conductivity, whereas insufficient oxide content will have a backfire effect on the system. Thin, weightless, and cheap GO film is a prosperous candidate to promote Li-S as a next generation high energy density battery with lightweight and low-cost attribute.

REFERENCES

[1] A. Manthiram, Y. Fu, S.H. Chung, C. Zu, Y.S. Su, Rechargeable lithium-sulfur batteries, Chem. Rev. 114 (2014) 11751–11787. doi:10.1021/cr500062v.

[2] Y. Yang, G. Zheng, Y. Cui, Nanostructured sulfur cathodes, Chem. Soc. Rev. 42 (2013) 3018. doi:10.1039/c2cs35256g.

[3] X. Ji, K.T. Lee, L.F. Nazar, A highly ordered nanostructured carbon–sulphur cathode for lithium–sulphur batteries, Nat. Mater. 8 (2009) 500–506. doi:10.1038/nmat2460.

[4] A. Manthiram, S.-H. Chung, C. Zu, Lithium-Sulfur Batteries: Progress and Prospects, Adv. Mater. 27 (2015) 1980–2006. doi:10.1002/adma.201405115.

[5] L. Chen, L.L. Shaw, Recent advances in lithium-sulfur batteries, J. Power Sources. 267 (2014) 770–783. doi:10.1016/j.jpowsour.2014.05.111.

[6] R. Van Noorden, The rechargeable revolution: A better battery, Nature. 507 (2014) 26–28. doi:10.1038/507026a.

[7] N. Deng, W. Kang, Y. Liu, J. Ju, D. Wu, L. Li, B.S. Hassan, B. Cheng, A review on separators for lithiumsulfur battery: Progress and prospects, J. Power Sources. 331 (2016) 132–155. doi:10.1016/j.jpowsour.2016.09.044.

[8] S. Xin, L. Gu, N.H. Zhao, Y.X. Yin, L.J. Zhou, Y.G. Guo, L.J. Wan, Smaller sulfur molecules promise better lithium'sulfur batteries, J. Am. Chem. Soc. 134 (2012) 18510–18513. doi:10.1021/ja308170k.

[9] S. Urbonaite, T. Poux, P. Novák, Progress Towards Commercially Viable Li-S Battery Cells, Adv. Energy Mater. 5 (2015). doi:10.1002/aenm.201500118.

[10] G. He, X. Ji, L. Nazar, High “C” rate Li-S cathodes: sulfur imbibed bimodal porous carbons, Energy Environ. Sci. 4 (2011) 2878. doi:10.1039/c1ee01219c.

[11] J. Schuster, G. He, B. Mandlmeier, T. Yim, K.T. Lee, T. Bein, L.F. Nazar, Spherical ordered mesoporous carbon nanoparticles with high porosity for lithium-sulfur batteries, Angew. Chemie - Int. Ed. 51 (2012) 3591–3595. doi:10.1002/anie.201107817.

[12] S.S. Zhang, Role of LiNO3 in rechargeable lithium/sulfur battery, Electrochim. Acta. 70 (2012) 344–348. doi:10.1016/j.electacta.2012.03.081.

[13] S.S. Zhang, A review on electrolyte additives for lithium-ion batteries, J. Power Sources. 162 (2006) 1379–1394. doi:10.1016/j.jpowsour.2006.07.074.

[14] Q. Pang, D. Kundu, M. Cuisinier, L.F. Nazar, Surface-enhanced redox chemistry of polysulphides on a metallic and polar host for lithium-sulphur batteries, Nat. Commun. 5 (2014) 4759. doi:10.1038/ncomms5759.

[15] X. Liang, C. Hart, Q. Pang, A. Garsuch, T. Weiss, L.F. Nazar, A highly efficient polysulfide mediator for lithium–sulfur batteries, Nat. Commun. 6 (2015) 5682. doi:10.1038/ncomms6682.

[16] Q. Pang, J. Tang, H. Huang, X. Liang, C. Hart, K.C. Tam, L.F. Nazar, A Nitrogen and Sulfur Dual-Doped Carbon Derived from Polyrhodanine@Cellulose for Advanced Lithium-Sulfur Batteries, Adv. Mater. 27 (2015) 6021–6028. doi:10.1002/adma.201502467.

[17] Z. Zhang, Z. Li, F. Hao, X. Wang, Q. Li, Y. Qi, R. Fan, L. Yin, 3D interconnected porous carbon aerogels as sulfur immobilizers for sulfur impregnation

for lithium-sulfur batteries with high rate capability and cycling stability, Adv. Funct. Mater. 24 (2014) 2500–2509. doi:10.1002/adfm.201303080.

[18] N. Mosavati, V.R. Chitturi, S.O. Salley, K.Y.S. Ng, Nanostructured titanium nitride as a novel cathode for high performance lithium/dissolved polysulfide batteries, J. Power Sources. 321 (2016) 87–93. doi:10.1016/j.jpowsour.2016.04.099.

[19] L. Ji, M. Rao, H. Zheng, L. Zhang, Y. Li, W. Duan, J. Guo, E.J. Cairns, Y. Zhang, Graphene oxide as a sulfur immobilizer in high performance lithium/sulfur cells, J. Am. Chem. Soc. 133 (2011) 18522–18525. doi:10.1021/ja206955k.

[20] B.P. Williams, Y.L. Joo, Tunable Large Mesopores in Carbon Nanofiber Interlayers for High-Rate Lithium Sulfur Batteries, J. Electrochem. Soc. 163 (2016) A2745–A2756. doi:10.1149/2.0931613jes.

[21] L. Qie, A. Manthiram, A facile layer-by-layer approach for high-areal-capacity sulfur cathodes, Adv. Mater. 27 (2015) 1694–1700. doi:10.1002/adma.201405689.

[22] A. Manthiram, Y. Fu, Y.-S. Su, Challenges and Prospects of Lithium-Sulfur Batteries, Acc. Chem. Res. (2012). doi:10.1021/ar300179v.

[23] M. Rao, X. Song, E.J. Cairns, Nano-carbon/sulfur composite cathode materials with carbon nanofiber as electrical conductor for advanced secondary lithium/sulfur cells, J. Power Sources. 205 (2012) 474–478. doi:10.1016/j.jpowsour.2012.01.047.

[24] J. Guo, Y. Xu, C. Wang, Sulfur-impregnated disordered carbon nanotubes cathode for lithium-sulfur batteries, Nano Lett. 11 (2011) 4288–4294. doi:10.1021/nl202297p.

[25] J. Guo, Y. Xu, C. Wang, Sulfur-impregnated disordered carbon nanotubes cathode for lithium-sulfur batteries, Nano Lett. 11 (2011) 4288–4294. doi:10.1021/nl202297p.

[26] K. Dong, S. Wang, H. Zhang, J. Wu, Preparation and electrochemical performance of sulfur-alumina cathode material for lithium-sulfur batteries, Mater. Res. Bull. 48 (2013) 2079–2083. doi:10.1016/j.materresbull.2013.02.031.

[27] Q. Li, Z. Zhang, K. Zhang, J. Fang, Y. Lai, J. Li, A simple synthesis of hollow carbon nanofiber-sulfur composite via mixed-solvent process for lithium-sulfur batteries, J. Power Sources. 256 (2014) 137–144. doi:10.1016/j.jpowsour.2014.01.063.

[28] L. Zhang, L. Ji, P.-A. Glans, Y. Zhang, J. Zhu, J. Guo, Electronic structure and chemical bonding of a graphene oxide–sulfur nanocomposite for use in superior performance lithium–sulfur cells, Phys. Chem. Chem. Phys. 14 (2012) 13670. doi:10.1039/c2cp42866k

[29] J.Q. Huang, T.Z. Zhuang, Q. Zhang, H.J. Peng, C.M. Chen, F. Wei, Permselective graphene oxide membrane for highly stable and anti-self-discharge lithium-sulfur batteries, ACS Nano. 9 (2015) 3002–3011. doi:10.1021/nn507178a

[30] R. Elazari, G. Salitra, A. Garsuch, A. Panchenko, D. Aurbach, Sulfur-impregnated activated carbon fiber cloth as a binder-free cathode for rechargeable Li-S batteries, Adv. Mater. 23 (2011) 5641–5644. doi:10.1002/adma.201103274.

[31] X. Wang, Z. Wang, L. Chen, Reduced graphene oxide film as a shuttle-inhibiting interlayer in a lithium-sulfur battery, J. Power Sources. 242 (2013) 65–69. doi:10.1016/j.jpowsour.2013.05.063 Short communication.

[32] M. Davies, High resolution XPS of organic polymers: The Scienta ESCA300 database - G. Beamson and D. Briggs John Wiley, Biomaterials. 15 (1994) 318. doi:10.1002/adma.19930051035.

[33] R.J. Waltman, J. Pacansky, C.W. Bates, X-ray Photoelectron Spectroscopic Studies on Organic Photoconductors: Evaluation of Atomic Charges on Chlorodiane Blue and p-(Diethylamino)benzaldehyde Diphenylhydrazone, Chem. Mater. 5 (1993) 1799–1804. doi:10.1021/cm00036a018.

[34] T. Wei, G. Luo, Z. Fan, C. Zheng, J. Yan, C. Yao, W. Li, C. Zhang, Preparation of graphene nanosheet/polymer composites using in situ reduction-extractive dispersion, Carbon N. Y. 47 (2009) 2296–2299. doi:10.1016/j.carbon.2009.04.030.

[35] S. Stankovich, D.A. Dikin, R.D. Piner, K.A. Kohlhaas, A. Kleinhammes, Y. Jia, Y. Wu, S.B.T. Nguyen, R.S. Ruoff, Synthesis of graphene-based nanosheets via chemical reduction of exfoliated graphite oxide, Carbon N. Y. 45 (2007) 1558–1565. doi:10.1016/j.carbon.2007.02.034.

[36] S. Park, J. An, I. Jung, R.D. Piner, S.J. An, X. Li, A. Velamakanni, R.S. Ruoff, Colloidal suspensions of highly reduced graphene oxide in a wide variety of organic solvents, Nano Lett. 9 (2009) 1593–1597. doi:10.1021/nl803798y.

[37] A. Ganguly, S. Sharma, P. Papakonstantinou, J. Hamilton, Probing the thermal deoxygenation of graphene oxide using high-resolution in situ X-ray-based spectroscopies, J. Phys. Chem. C. 115 (2011) 17009–17019. doi:10.1021/jp203741y.

[38] C. Mattevi, G. Eda, S. Agnoli, S. Miller, K.A. Mkhoyan, O. Celik, D. Mastrogiovanni, G. Granozzi, E. Carfunkel, M. Chhowalla, Evolution of electrical,

chemical, and structural properties of transparent and conducting chemically derived graphene thin films, Adv. Funct. Mater. 19 (2009) 2577–2583. doi:10.1002/adfm.200900166.

[39] D. Yang, A. Velamakanni, G. Bozoklu, S. Park, M. Stoller, R.D. Piner, S. Stankovich, I. Jung, D.A. Field, C.A. Ventrice, R.S. Ruoff, Chemical analysis of graphene oxide films after heat and chemical treatments by X-ray photoelectron and Micro-Raman spectroscopy, Carbon N. Y. 47 (2009) 145–152. doi:10.1016/j.carbon.2008.09.045.

[40] A. Barinov, L. Gregoratti, P. Dudin, S. La Rosa, M. Kiskinova, Imaging and spectroscopy of multiwalled carbon nanotubes during oxidation: Defects and oxygen bonding, Adv. Mater. 21 (2009) 1916–1920. doi:10.1002/adma.200803003.

[41] Y.-Q. Wang, F.-Q. Zhang, P.M. a. Sherwood, X-ray Photoelectron Spectroscopic Study of Carbon Fiber Surfaces. 23. Interfacial Interactions between Polyvinyl Alcohol and Carbon Fibers Electrochemically Oxidized in Nitric Acid Solution, Chem. Mater. 11 (1999) 2573–2583. doi:10.1021/cm9902772.

[42] X.H. Li, S. Kurasch, U. Kaiser, M. Antonietti, Synthesis of monolayer-patched graphene from glucose, Angew. Chemie - Int. Ed. 51 (2012) 9689–9692. doi:10.1002/anie.201203207.

[43] C. Nithya, S. Gopukumar, rGO/nano Sb composite: a high performance anode material for Na^+ ion batteries and evidence for the formation of nanoribbons from the nano rGO sheet during galvanostatic cycling, J. Mater. Chem. A. 2 (2014) 10516–10525. doi:10.1039/C4TA01324G.

[44] X. Zhou, Y. Li, G. Ma, Q. Ma, Z. Lei, One-step solid-state synthesis of sulfur-reduced graphene oxide composite for lithium-sulfur batteries, J. Alloys Compd. 685 (2016) 216–221. doi:10.1016/j.jallcom.2016.05.171.

[45] H.C. Schniepp, J.L. Li, M.J. McAllister, H. Sai, M. Herrera-Alonson, D.H. Adamson, R.K. Prud'homme, R. Car, D.A. Seville, I.A. Aksay, Functionalized single graphene sheets derived from splitting graphite oxide, J. Phys. Chem. B. 110 (2006) 8535–8539. doi:10.1021/jp060936f.

[46] H.K. Jeong, P.L. Yun, R.J.W.E. Lahaye, M.H. Park, H.A. Kay, J.K. Ick, C.W. Yang, Y.P. Chong, R.S. Ruoff, H.L. Young, Evidence of graphitic AB stacking order of graphite oxides, J. Am. Chem. Soc. 130 (2008) 1362–1366. doi:10.1021/ja076473o.]

[47] H. Yamin, A. Gorenshtein, J. Penciner, Y. Sternberg, E. Peled, Lithium Sulfur Battery: Oxidation/Reduction Mechanism of Polysulfides in THF Solutions, J. Electrochem. Soc. 135 (1988) 1045. doi:10.1149/1.2095868.

[48] Y. Lu, S. Gu, J. Guo, K. Rui, C. Chen, S. Zhang, J. Jin, J. Yang, Z. Wen, Sulfonic Groups Originated Dual-Functional Interlayer for High Performance Lithium-Sulfur Battery, ACS Appl. Mater. Interfaces. 9 (2017) 14878–14888. doi:10.1021/acsami.7b02142.

[49] L. Qie, C. Zu, A. Manthiram, A High Energy Lithium-Sulfur Battery with Ultrahigh-Loading Lithium Polysulfide Cathode and its Failure Mechanism, Adv. Energy Mater. 6 (2016). doi:10.1002/aenm.201502459.REFERENCES

CHAPTER 3

EFFECTIVE SUPPRESSION OF THE POLYSULFIDE SHUTTLE EFFECT IN LITHIUM–SULFUR BATTERIES BY IMPLEMENTING RGO-PEDOT:PSS COATED SEPARATORS VIA AIR-CONTROLLED ELECTROSPRAY

Abstract

Lithium-sulfur batteries are promising battery systems for becoming the next-generation energy storage devices. However, realizing their practical value is greatly challenged by the limitation of exhibiting poor cycling performances due to the low electrical conductivity of sulfur active material and polysulfide shuttling effect during cycling. To solve these issues, a hybrid structure of reduced graphene oxide and poly(3,4-ethylenedioxythiophene):poly(styrene sulfonate) was fabricated and coated onto the surface of the separator using the air-controlled electrospray method in this work. By embedding this coated separator into the lithium-sulfur batteries, lower polarization was ensued. Also, a combination of physical and chemical interactions mitigated the polysulfide shuttling effect. Hence, using these hybrid coatings led to improvement in the initial capacity and improved cycling performances, resulting from higher active material utilization and fewer loss of the active material. Overall, this investigation demonstrates this coating material offers improvement on lithium-sulfur battery technology.

Introduction

In recent years, development of electric vehicles and smart grids has been on the rise. To accommodate such high-power requiring inventions, energy storage devices with high energy densities are utmost necessary.[1, 2] Conventional lithium-ion batteries (LIBs) have been able to accomplish great success in the energy storage sector, but they are still not sufficient enough to supply the power demands that electric vehicles and grid-scale applications require.[1, 3, 4] Hence, many groups have attempted to study different battery chemistries, and lithium-sulfur batteries (Li–S) are rising as one of the next-generation energy storage devices.

Lithium-sulfur batteries (Li–S) have been attracting intense attention because of its high theoretical capacity (1675 mA h g^{-1}) and energy density (2600 Wh kg^{-1}). In addition, this battery system utilizes sulfur as the cathode material, which is non-toxic and abundant.[5-8] Despite these striking advantages, there are some limitations to this technology that remains unsolved. Firstly, sulfur is electrically insulating, which causes high cell polarization and under-utilization of active materials.[7,8] Secondly, the dissolution of intermediate lithium polysulfide species in the electrolyte leads to irreversible loss of sulfur, resulting in rapid capacity fading and poor Coulombic efficiency of the cells.[5 ,7 ,9] Thirdly, huge volume expansion of sulfur during the repeated charging/discharging processes devastates the structural integrity of the electrodes, which leads to poor electrical contact with the conductive additives and current collectors.[10]

Many efforts have been devoted to address these challenging issues in Li–S batteries by developing and applying multiple types of porous nanostructured sulfur electrodes.[8, 10] Multidimensional carbon/sulfur composites based on carbon nanofiber web structures,[11-13] carbon nanotubes[14-17], reduced graphene oxide sheets[18-20] have been conducted as a mainstream approach due to their high specific surface area and electrical conductivity. These innovative strategies involving composite materials not only improve the reaction kinetics but also alleviate the degree of polysulfide migration by localizing the sulfur particles in the cathode compartment of the cell. However, adding such inactive carbon material leads to an overall lower energy density of the cell. In addition, fabricating and processing nanostructured electrode materials can be time consuming and difficult as it most often requires multiple steps.[4, 9, 21]

Utilizing coated separators in Li–S batteries has been sought out as a potential solution to resolve such matters.[6, 9, 22-27] Manthiram group have demonstrated that the highly conductive carbon layers on the separator suppress polysulfide shuttle effect through physical trapping and provide enhanced conductivity by acting as an "additional current collector", which improves the electrochemical performance.[22] However, the weak adsorption with polysulfides induces problems with long-term capturing abilities, leading to limited cycling stability.[24, 28] As a result, to reinforce the chemical interaction with polysulfides, polar materials such as graphene oxide[28, 29], inorganic oxide material[30, 31], metal-organic framework[32], conducting polymer[33] , and boron nitride nanosheets[34] have been investigated as coating materials. Albeit such progress in polysulfide chemisorption on polar surfaces, further investigations on

coated separators are still needed because the functional groups reduces the electrical conductivity. Therefore, it is crucial to design an appropriate structure and material of coated separators that are highly conductive in an effective manner for suppressing the polysulfide shuttle effect. Recently, Cui et al. have conducted studies on applying conducting polymers to Li–S cathodes. The polar heteroatoms in these polymer shells had strong interactions with polysulfides to form chemical bonds, preventing polysulfide dissolution.[35, 36] The resulting Li–S battery performances indicated that the mesoporous carbon/sulfur composite coating layer of PEDOT:PSS turned out to be superior over the other conducting polymers. Despite this fact, an additional augmentation to increase the conductivity of PEDOT:PSS along with the physical support could undoubtedly improve the performances of Li–S batteries even further.

Herein, we propose a facile strategy to uniformly coat the surface of the separator with hybrid rGO-PEDOT:PSS structures. Through the means of air-controlled electrospraying, rGO-PEDOT:PSS can not only be coated uniformly, but falso swiftly on a designated substrate. By applying rGO-PEDOT:PSS coated separators to Li–S batteries, prominent benefits can be achieved. Firstly, the conductive coating layer promotes electron transfer, which leads to low polarization and fast redox reaction kinetics. Secondly, the polar nature of PEDOT:PSS induces chemical interactions with polysulfides and the chemical adsorption of polysulfide species onto PEDOT:PSS hampers the redox shuttle effect. Thirdly, the well-developed layer structure of rGO-PEDOT:PSS provides physical trapping sites for polysulfide, which in turn, mitigates the polysulfide shuttling effect. By utilizing this

method, we were able to achieve improved cycling performances for Li–S batteries through the synergistic effects by rGO and PEDOT:PSS.

Experimental

General Procedure of Air-Controlled Electrospray of rGO-PEDOT:PSS.

rGO-PEDOT:PSS coated separators were fabricated by utilizing the air-controlled electrospray process. Typically, to prepare rGO-PEDOT:PSS hybrid structures, pristine rGO is dispersed in deionized water through mild sonication. For this solution, a PEDOT:PSS solution (Sigma Aldrich, 1.3 wt. % dispersion in water) was added at a rGO-PEDOT:PSS weight ratio of 1:1 and stirred vigorously to make a homogeneous solution before spraying. The air-controlled electrospray was carried out onto a 25-micron thick Celgard PE separator using a Harvard Apparatus PHD 2000 Infusion syringe pump with a coaxial needle set under room temperature. The solution was supplied to the inner 12-gauge needle, and 20 psi air flow rate was applied thorough the 17-gauge outer shell. The working voltage was set at 15 kV, with 15 cm in distance from the needle tip to the collector, and 0.08 mL min^{-1} of solution feeding rate. The mass loading of the hybrid coating was around 0.6 mg cm^{-2}.

Preparation of the Li_2S_6 Solution

Sulfur (Spectrum Chemical) and Li_2S (Sigma Aldrich) were added to 1,2-dimethoxyethane and 1,3-dioxolane (1:1 in volume) to form a molar ratio of 5:1. Afterwards, the solution was heated to 90 °C and vigorously stirred for 12 h under an argon atmosphere to yield the Li_2S_6 Solution.

Characterization Methods

Fourier Transform Infrared spectra were recorded with a Nicolet Magna-IR 560 using an average of 180 scans with a resolution of 4 cm^{-1}. Thermogravimetric analysis was carried out with a TA instrument (TGA 500) at a heating rate of 10 °C min^{-1} under a N_2 atmosphere. Scanning electron microscopy (SEM) images were taken using a Tescan Mira3 Field Emission SEM. UV-vis absorption spectra were obtained by using a spectrophotometer (Spectramax 384) and X-ray photoelectron spectroscopy measurements were conducted with a Surface Science Instrument equipped with a monochromatic Al Kα X-ray source (1468.6 eV). Electrochemical characterizations of the coated separator were performed using 2032-type coin cells consisting Li metal anode (MTI Corporation) and a slurry coated sulfur cathode. The cathode material contained 70 wt. % sulfur/carbon composite material, 15 wt. % PVDF (Sigma Aldrich, Mw = 534,000), and 15 wt. % Super P (TIMCAL). The default composite material consisted of 80 wt. % of sublimated sulfur and 20 wt. % of Super P, and the sulfur was infiltrated into the Super P at 155 °C for 12 h. The electrodes were dried at 60 °C under vacuum for 12 h and then punched into circular disc pieces with a diameter of 15 mm. The mass loading of the sulfur active material on the cathode was around 1.0 mg cm^{-2}. The electrolyte was 1 M of bis(trifluoromethane)sulfonimide lithium salt (LiTFSI) and 0.1 M of lithium nitrate ($LiNO_3$) in a 1: 1 volume ratio of 1,2-dimethoxyethane (DME) and 1,3-Dioxolane (DOL), all purchased from Sigma Aldrich. All the cells were assembled in an argon-filled glove box. Cyclic

voltammetry and electrochemical impedance spectroscopy (EIS) test was performed using a potentiostat/galvanostat (Princeton PARSAT 4000). Galvanostatic charge/discharge measurements were carried out in the voltage range of 1.8–2.8 V using a battery cycler (MTI) at room temperature. All of the current densities and specific capacities calculated in this study were based on sulfur mass.

Result and Discussion

The rGO-PEDOT:PSS coated separator was prepared via a facile air-controlled electrospray method which has been demonstrated that the material of interest is easily deposited on a designated substrate through a high speed air stream.[11, 37] To prepare the solution for electrospraying, an aqueous solution containing PEDOT:PSS was added into the rGO solution under gentle stirring and a mild sonication to promote the dispersion of rGO in the solvent. As clearly shown in Figure 3.1, the dispersion of rGO in the solvent was significantly improved after incorporating PEDOT:PSS, possibly due to non-covalent stabilization.[38, 39] To elaborate, the hydrophobic component of the polymer chains tends to wrap around the surface of rGO via π- π interactions, while the hydrophilic PSS dissociates rGO from the solvent molecules. Such an interaction could lead to more uniform distribution of the rGO-PEDOT:PSS hybrid, which would promote the structural integrity and electron transfer.

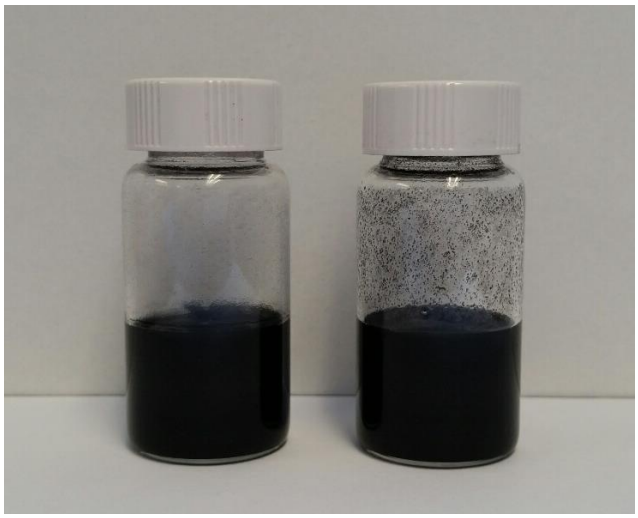

Figure 3.1 Digital image of rGO-PEDOT:PSS solution (left) and and rGO solution (right). Adding PEDOT:PSS significantly improved the dispersion of rGO

Figure 3.2a presents a schematic cell configuration of the Li-S batteries with the rGO-PEDOT:PSS coated separator. The coated separator was placed between the cathode and the separator to suppress the polysulfide shuttle effect during electrochemical reactions. The air-controlled electrospraying deposition process resulted in an excellent adhesion of rGO-PEDOT:PSS onto the Celgard separator (Figure 3.2b,c), which was demonstrated by the folding test as presented in Figure 3.2d. Scanning electron microscopy (SEM) was employed to characterize the surface morphology of the rGO-PEDOT:PSS hybrid coating on the separator. As shown in Figure 3.2e-g, a dense layer of rGO-PEDOT:PSS covering the nanopores on the surface of the separator was observed. This conductive layer could physically prevent the lithium polysulfides from migrating to the anode compartment and improve the transport of electron and lithium ion and, providing a low polarization and fast redox reaction kinetics.

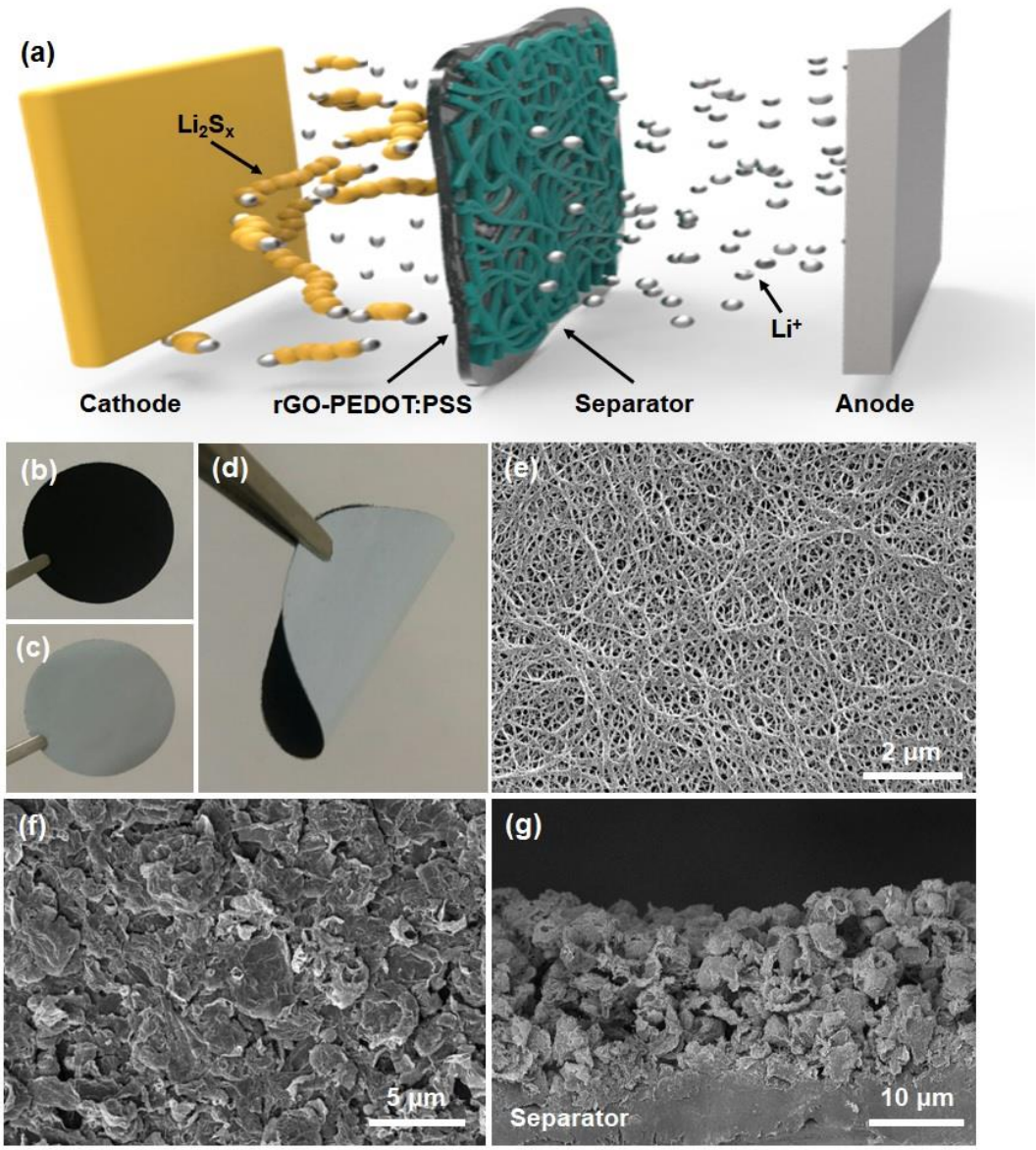

Figure 3.2a) Schematic illustration of cell configuration with rGO-PEDOT:PSS coated separator. b,c,d) image of adhesion of rGO-PEDOT:PSS and flexible interlayer. SEM images of e) pristine separator f) top-view coated separator g) cross-section coated separator.

The hybrid structure of PEDOT:PSS and rGO was characterized using FTIR analysis, with spectra of rGO, PEDOT:PSS and rGO-PEDOT:PSS presented in Figure 3.3. rGO exhibited very small absorption bands widely ranging from 700 cm^{-1} to 1200 cm^{-1}, owing to potential carbon-carbon bonds and oxygen containing bonds.[40] Meanwhile, the pristine PEDOT:PSS exhibited two notable absorption bands at 1325 cm^{-1} and 1511 cm^{-1}. The two bands correspond to C-C or C=C stretching from the quinoid conformation structure and C-C or C=C stretching from the thiophene ring, respectively. The absorption band at 1182 cm^{-1} is assigned to the symmetric vibration from the $-SO_3$ group in the PSS chain. The vibration at 1147 cm^{-1} corresponds to C-O-C stretching from the ethylenedioxy group. In addition, C-S vibrations from the thiophene ring was also observed, which is verified by the absorption bands occurring at 975 cm^{-1} and 876 cm^{-1}.[41, 42] While the rGO-PEDOT:PSS spectra were shifted slightly, all of the absorption bands are from either pure rGO or pristine PEDOT:PSS, confirming the hybrid structure from the interactions.

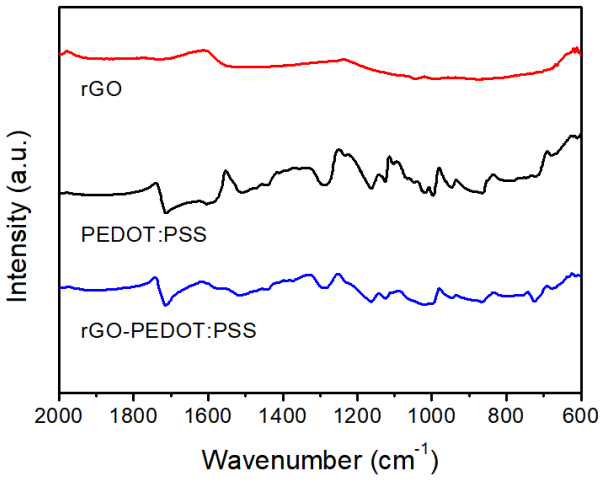

Figure 3.3 FTIR spectra of rGO, PEDOT:PSS, and rGO-PEDOT:PSS

The redox behavior of the sulfur cathodes with the rGO-PEDOT:PSS coated separator was initially evaluated by cyclic voltammetry (CV) measurements at a scan rate of 0.1 mV s^{-1}. The CV data for the neat Celgard Polypropylene (PP) separator was also given for comparison. As shown in Figure 3.4a, the cell with the neat separator exhibited two broad cathodic peaks and an anodic peak due to the sluggish kinetic process.[31] In comparison, the incorporation of rGO-PEDOT:PSS coating resulted in well-defined redox peaks with an increase in current density, suggesting the improved redox reaction kinetics and utilization of the active materials in the cells.[31, 43] Furthermore, redox peaks of the cathode with rGO-PEDOT:PSS coating of each cycle highly overlapped (Figure 3.5), indicating a lower cell polarization and excellent electrochemical reversibility.

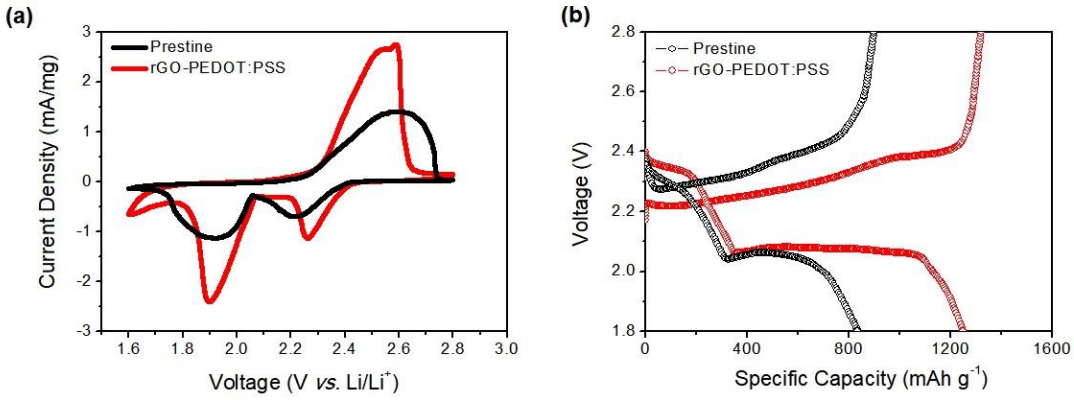

Figure 3.4 a) Cyclic voltammogram of pristine and coated separator b) first cycle charge/discharge profile of pristine and coated separator.

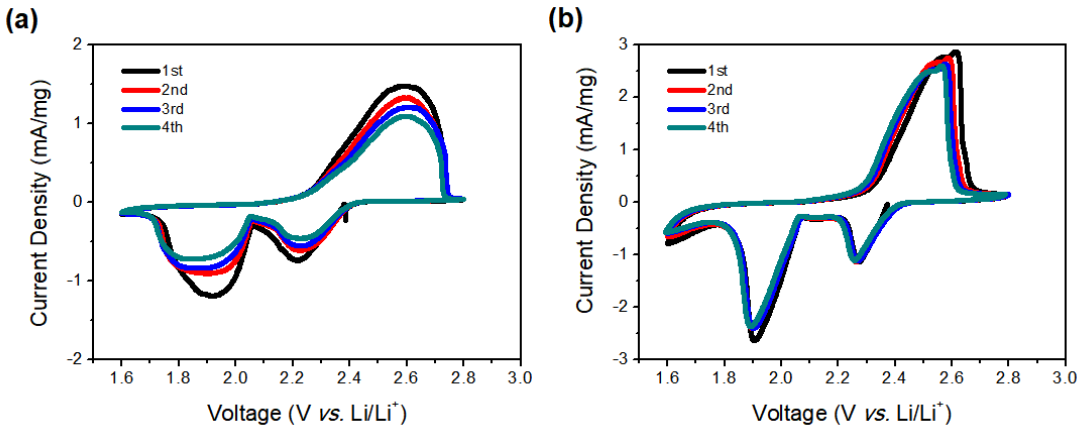

Figure 3.5a) Cyclic voltammograms of the cell with pristine separator and (b) coated separator

Figure 3.4b) shows galvanostatic charge/discharge profiles of cells after an initial activation process. As presented above, both cells exhibited two typical discharge plateaus, which agrees with the CV curves. The upper discharge plateau corresponds to cyclic elemental sulfur reduction to long-chain lithium polysulfide and the lower discharge plateau pertains to the formation of short-chain insoluble polysulfide (Li_2S_2/Li_2S) products.[7] It can be seen that the discharge plateaus for the cell with rGO-PEDOT:PSS coated separator were found to be longer, flatter, and have a lower polarization than the cell with only the neat separator. Obviously, the cell with the coated separator delivered a higher discharge capacity value of 1249.4 mAh g^{-1}, whereas the cell with the neat separator exhibited limited discharge capacity of 834.3 mAh g^{-1}, confirming high sulfur utilization enabled by the coated separator.

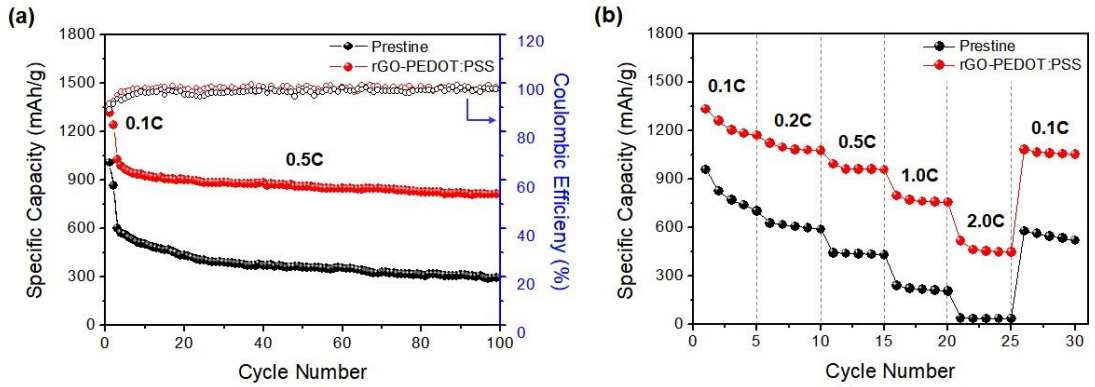

Figure 3.6a) Cycling performance and b) rate capability of pristine and coated separator.

Subsequently, the cycling performance of the cells was investigated further via estimation of 100 cycles at a current density of 0.5 C. As displayed in Figure 3.6a, the cells assembled with coated separators was able to deliver larger discharge capacities and maintain a relatively stable cycling performance with a higher Coulombic efficiency over their counterparts. After repeated cycling, the retained discharge capacity value was as high as 812.8 mAh g^{-1}. In contrast, the cell with the neat separator showed a lower discharge capacity of 296.8 mAh g^{-1}, which probably resulted from the limited sulfur utilization and continuous dissolution of lithium polysulfide into the electrolyte. The rate capability of the cells was also measured at various current densities and is presented in Figure 3.6b. As expected, the cell assembled with the neat separator suffered from poor cycling behavior. Even at a mild condition of 0.1 C, the cell continued to maintain lower discharge capacity values. Moreover, the difference in discharge capacities between the cells was observed to be conspicuous at high current densities in which the effect of redox reaction kinetics was

more significant. When the current density increased to 2 C, the cell with the coated separator still achieved 38.9 % of its initial capacity, whereas the discharge capacity retention of the cell with the neat separator was around 0.04 %. After returning to the initial current density of 0.1 C, a reasonable discharge capacity of 1069.7 mAh g^{-1} was able to recover, indicating an improved reversibility and stability.

The overall enhanced electrochemical performances of the cell with the coated separator can be attributed to several factors. Firstly, the increase in amount of conductive pathways that the rGO-PEDOT:PSS hybrid structure provides facilitated redox electron transfer and reduced interfacial resistance, allowing for a high conversion rate of lithium polysulfide into favorable chemical compounds for charge storage. Secondly, a well-developed coating layer not only serves as a physical barrier but also gives rise to a polar interaction for lithium polysulfides to suppress the loss of the active material, which in turn enhances reutilization/reactivation of the trapped active material and thus contribute to the higher capacitive behavior.

As such, a visual depiction of lithium polysulfide species and its trapping in rGO-PEDOT:PSS is presented. Note that the polysulfide investigated here was Li_2S_6, which is the representative polysulfide species. As depicted in the Figure 3.7a inset, the Li_2S_6 in DOL:DME solvent was a red-brown colored solution. Remarkably, adding rGO-PEDOT:PSS powders into the polysulfide solution resulted in color fading. UV-vis absorption characterization was also conducted to confirm the concentration changes of Li_2S_6 solutions. It has been previously reported that the noticeable absorption band in the 400-500 cm^{-1} region is related to the Li_2S_6.[43, 44] As shown in

Figure 4a, we observed a sharp decrease in absorption band, suggesting that the rGO-PEDOT:PSS exhibited strong interactions with Li_2S_6 molecules. According to other literatures, polar atoms in PEDOT offer chemical binding with lithium polysulfides to form a chelated coordination structure.[35] In this study, the as-prepared sample is composed of PEDOT:PSS and rGO sheets, which could provide a synergetic effect for adsorption of lithium polysulfide. These observed results were consistent with the behavior of the cycled separators. As depicted in Figure 3.8, the pristine PP separator for the reference cell after cycling was vividly yellow in color due to the inevitable contamination caused by the dissolved lithium polysulfides in the electrolytes.[45] On the other hand, the rGO-PEDOT:PSS coated separator with regions where the coating was peeled off showed original pristine separator color, indicating the migration of soluble polysulfide was relatively confined on the cathode side rather than diffusing to the anode side.

To better understand the adsorption of polysulfide, X-ray photoelectron spectroconscopy (XPS) was employed. As shown in Figure 3.7b, LiTFSI and polysulfide peaks were observed after cycling in the S_{2p} spectra. The peak of LiTFSI arising from the electrolyte salt was detected at around 170 eV of binding energy, while the lower energy peak in the range between 162 eV to 165 eV was attributed to the insoluble Li_2S-Li_2S_2-S compound.[46, 47] These results suggest that improved electrochemical performances could be correlated with the adsorption of polysulfide species within the hybrid coating, which could help suppress the shuttling effect, leading to high reutilization/reactivation of the entrapped active materials in the cathode.

A further manifestation of the alleviated polysulfide shuttling effect was confirmed by analyzing the cycled lithium metal anodes. The SEM micrographs of the morphology of the lithium anode surface after cycling with the pristine PP separator, and cycling with rGO-PEDOT:PSS coated separator were compared (Figure 3.7c-e). As shown in Figure 3.7d, a rough lithium metal surface was observed along with irregular aggregates in the cell with the neat separator, which is associated with the formation of the passivation layer (Li_2S_2/Li_2S) derived from a reaction between dissolved lithium polysulfides and the lithium metal anode during cycling.[29] This reaction attributed a major cause of active material loss and inner resistance build up, resulting in the fast degradation of cycling stability. In contrast, in the cell with coated separator, the surface of lithium metal was found to be smoother (Figure 3.7e), which is an obvious indication of the protected lithium metal surface against corrosion.[29, 44] This result also demonstrates that the lithium polysulfides shuttle effect and parasitic reactions were highly restricted by the coated separator.

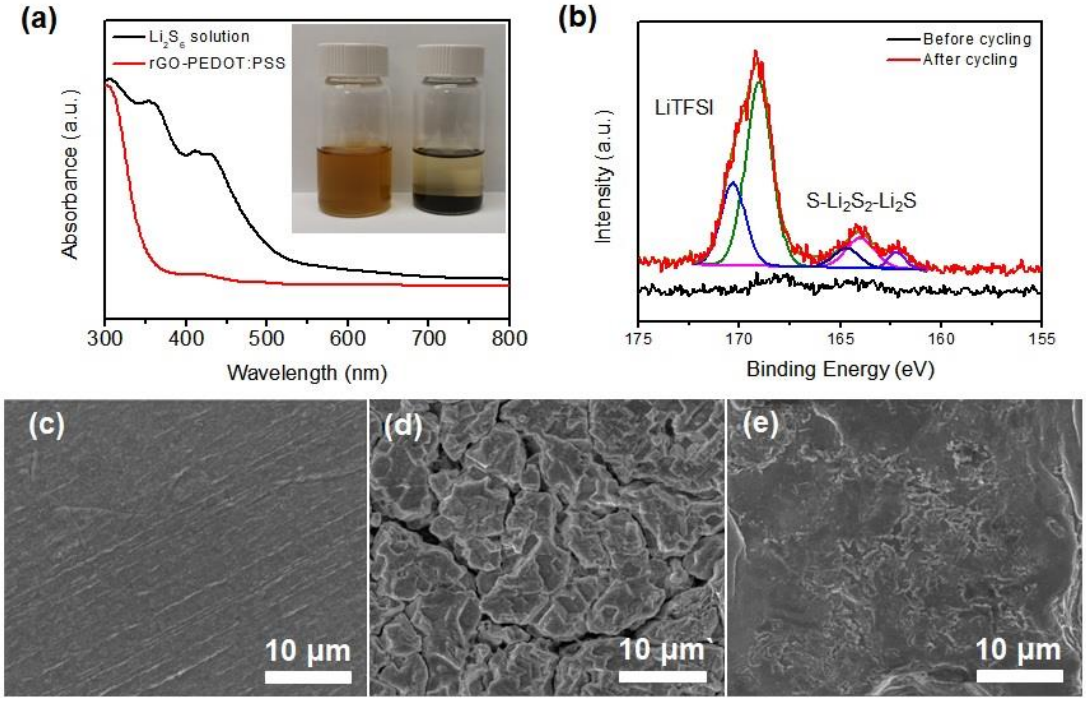

Figure 3.7 a) UV-Vis of lithium Li_2S_6 solution pristine and after rGO-PEDOT:PSS absorbance and digital images of Li_2S_6 solution (left) and Li_2S_6 with rGO-PEDOT:PSS (right). b) XPS high resolution of S_{2p} after cycling c) SEM images of c) Celgard separator d) Lithium anode with pristine separator e) Lithium anode with coated separator.

Figure 3.8) Digital image of Celgard separator after cycling a) pristine separator b) coated separator

Finally, we proceeded to evaluate electrochemical impedance responses of cells before and after cycling. As shown in Figure 3.9a, each Nyquist plot before cycling is composed of a depressed semicircle in the medium to high frequency region and an oblique line in the low frequency region. The former is coupled with the bulk resistance from the electrolyte and charge transfer resistance at the interface between the electrode and electrolyte, while the latter corresponds Warburg diffusion impedance of lithium ions in the electrode.[44] It was observed that the cell with the coated separator exhibited lower charge transfer resistance, which could be ascribed to the improved electrical conductivity of the cell with the coated separator as the conductive layer works as a second current collector in the cell.[22, 31] After cycling (Figure 3.9b), the bulk resistance increased for both cells, and the difference before and after cycling was larger in the cell with the neat separator, resulting from the increase in viscosity of the electrolyte, which is caused by the excessive polysulfide

dissolution.[48] On the other hand, a smaller charge transfer resistance for the cell with coated separator was detected, indicating that the polysulfide shuttling behavior and deposition of insoluble Li_2S_2/Li_2S layer on the electrode were suppressed during cycling.

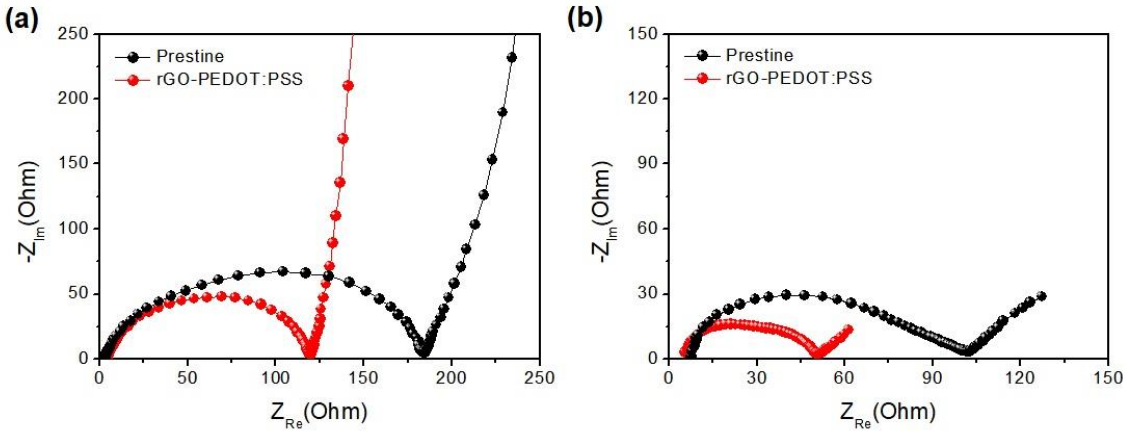

Figure 3.9a) Impedance spectra before cycling b) after cycling

4. CONCLUSIONS

In conclusion, Li-S batteries with rGO-PEDOT:PSS coated separators were successfully fabricated by using the method of air-controlled electrospray process. The improved electrical conductivity and suppressed polysulfide shuttling behavior allowed for enhanced reaction kinetics and reutilization/reactivation of active material. Electrochemical evaluations revealed that the rGO-PEDOT:PSS coated separator could deliver high specific capacity and enhanced cycling performances, suggesting high prospects of this coating material being applied in Li-S batteries.

REFERENCES

(1) Larcher, D.; Tarascon, J. M. Towards greener and more sustainable batteries for electrical energy storage. *Nat. Chem.* **2014,** *7*, 19-29.

(2) Goodenough, J. B. Energy storage materials: A perspective. *Energ. Storage Mater.* **2015,** *1*, 158-161.

(3) Choi, J. W.; Aurbach, D. Promise and reality of post-lithium-ion batteries with high energy densities. *Nat. Rev. Mater.* **2016,** *1*, 16013

(4) Sun, Y.; Liu, N.; Cui, Y. Promises and challenges of nanomaterials for lithium-based rechargeable batteries. *Nat. Energ.* **2016,** *1*, 16071.

(5) Bruce, P. G.; Freunberger, S. A.; Hardwick, L. J.; Tarascon, J.-M. Li–O_2 and Li–S batteries with high energy storage. *Nat. Mater.* **2011,** *11*, 19-29.

(6) Manthiram, A.; Fu, Y.; Chung, S.-H.; Zu, C.; Su, Y.-S. Rechargeable Lithium–Sulfur Batteries. *Chem. Rev.* **2014,** *114*, 11751-11787.

(7) Yin, Y.-X.; Xin, S.; Guo, Y.-G.; Wan, L.-J. Lithium–Sulfur Batteries: Electrochemistry, Materials, and Prospects. *Angew. Chem. Int. Ed.* **2013,** *52*, 13186-13200.

(8) Yang, Y.; Zheng, G.; Cui, Y. Nanostructured sulfur cathodes. *Chem. Soc. Rev.* **2013,** *42* (7), 3018-3032.

(9) Manthiram, A.; Fu, Y.; Su, Y.-S. Challenges and Prospects of Lithium–Sulfur Batteries. *Accounts Chem. Res.* **2013,** *46*, 1125-1134.

(10) Borchardt, L.; Oschatz, M.; Kaskel, S. Carbon Materials for Lithium Sulfur Batteries—Ten Critical Questions. *Chem-Eur. J.* **2016,** *22*, 7324-7351.

(11) Lee, J.; Ko, B.; Kang, J.; Chung, Y.; Kim, Y.; Halim, W.; Lee, J. H.; Joo, Y. L. Facile and scalable fabrication of highly loaded sulfur cathodes and lithium–sulfur pouch cells via air-controlled electrospray. *Mater. Today Energ.* **2017,** *6*, 255-263.

(12) Zheng, G.; Yang, Y.; Cha, J. J.; Hong, S. S.; Cui, Y. Hollow Carbon Nanofiber-Encapsulated Sulfur Cathodes for High Specific Capacity Rechargeable Lithium Batteries. *Nano Lett.* **2011,** *11*, 4462-4467.

(13) Ji, L.; Rao, M.; Aloni, S.; Wang, L.; Cairns, E. J.; Zhang, Y. Porous carbon nanofiber-sulfur composite electrodes for lithium/sulfur cells. *Energ. Environ. Sci.* **2011,** *4*, 5053-5059.

(14) Yuan, Z.; Peng, H.-J.; Huang, J.-Q.; Liu, X.-Y.; Wang, D.-W.; Cheng, X.-B.; Zhang, Q. Hierarchical Free-Standing Carbon-Nanotube Paper Electrodes with Ultrahigh Sulfur-Loading for Lithium–Sulfur Batteries. *Adv. Funct. Mater.* **2014,** *24*, 6105-6112.

(15) Guo, J.; Xu, Y.; Wang, C. Sulfur-Impregnated Disordered Carbon Nanotubes Cathode for Lithium–Sulfur Batteries. *Nano Lett.* **2011,** *11*, 4288-4294.

(16) Zhao, Y.; Wu, W.; Li, J.; Xu, Z.; Guan, L. Encapsulating MWNTs into Hollow Porous Carbon Nanotubes: A Tube-in-Tube Carbon Nanostructure for High-Performance Lithium-Sulfur Batteries. *Adv. Mater.* **2014,** *26*, 5113-5118.

(17) Tang, C.; Zhang, Q.; Zhao, M.-Q.; Huang, J.-Q.; Cheng, X.-B.; Tian, G.-L.; Peng, H.-J.; Wei, F. Nitrogen-Doped Aligned Carbon Nanotube/Graphene Sandwiches: Facile Catalytic Growth on Bifunctional Natural Catalysts and Their Applications as Scaffolds for High-Rate Lithium-Sulfur Batteries. *Adv. Mater.* **2014,** *26*, 6100-6105.

(18) Zhou, G.; Pei, S.; Li, L.; Wang, D.-W.; Wang, S.; Huang, K.; Yin, L.-C.; Li, F.;

Cheng, H.-M. A Graphene–Pure-Sulfur Sandwich Structure for Ultrafast, Long-Life Lithium–Sulfur Batteries. *Adv. Mater.* **2014,** *26*, 625-631.

(19) Wang, H.; Yang, Y.; Liang, Y.; Robinson, J. T.; Li, Y.; Jackson, A.; Cui, Y.; Dai, H. Graphene-Wrapped Sulfur Particles as a Rechargeable Lithium–Sulfur Battery Cathode Material with High Capacity and Cycling Stability. *Nano Lett.* **2011,** *11*, 2644-2647.

(20) Li, N.; Zheng, M.; Lu, H.; Hu, Z.; Shen, C.; Chang, X.; Ji, G.; Cao, J.; Shi, Y. High-rate lithium-sulfur batteries promoted by reduced graphene oxide coating. *Chem. Commun.* **2012,** *48*, 4106-4108.

(21) Fu, C.; Guo, J. Challenges and current development of sulfur cathode in lithium–sulfur battery. *Curr. Opin. Chem. Eng.* **2016,** *13*, 53-62.

(22) Su, Y.-S.; Manthiram, A. Lithium–sulphur batteries with a microporous carbon paper as a bifunctional interlayer. *Nat. Commun.* **2012,** *3*, 1166.

(23) Xiao, Z.; Yang, Z.; Wang, L.; Nie, H.; Zhong, M. e.; Lai, Q.; Xu, X.; Zhang, L.; Huang, S. A Lightweight TiO2/Graphene Interlayer, Applied as a Highly Effective Polysulfide Absorbent for Fast, Long-Life Lithium–Sulfur Batteries. *Adv. Mater.* **2015,** *27*, 2891-2898.

(24) Huang, J.-Q.; Zhang, Q.; Wei, F. Multi-functional separator/interlayer system for high-stable lithium-sulfur batteries: Progress and prospects. *Energ. Storage Mater.* **2015,** *1*, 127-145.

(25) Chung, S.-H.; Manthiram, A. Bifunctional Separator with a Light-Weight Carbon-Coating for Dynamically and Statically Stable Lithium-Sulfur Batteries. *Adv. Funct. Mater.* **2014,** *24*, 5299-5306.

(26) Balach, J.; Jaumann, T.; Klose, M.; Oswald, S.; Eckert, J.; Giebeler, L. Functional Mesoporous Carbon-Coated Separator for Long-Life, High-Energy Lithium–Sulfur Batteries. *Adv. Funct. Mater.* **2015,** *25*, 5285-5291.

(27) Chung, S.-H.; Manthiram, A. A Polyethylene Glycol-Supported Microporous Carbon Coating as a Polysulfide Trap for Utilizing Pure Sulfur Cathodes in Lithium–Sulfur Batteries. *Adv. Mater.* **2014,** *26*, 7352-7357.

(28) Chang, C.-H.; Chung, S.-H.; Nanda, S.; Manthiram, A. A rationally designed polysulfide-trapping interface on the polymeric separator for high-energy Li–S batteries. *Mater. Today Energ.* **2017,** *6*, 72-78.

(29) Kong, W.; Yan, L.; Luo, Y.; Wang, D.; Jiang, K.; Li, Q.; Fan, S.; Wang, J. Ultrathin MnO_2/Graphene Oxide/Carbon Nanotube Interlayer as Efficient Polysulfide-Trapping Shield for High-Performance Li–S Batteries. *Adv. Funct. Mater.* **2017,** *27*, 201606663.

(30) Liu, M.; Li, Q.; Qin, X.; Liang, G.; Han, W.; Zhou, D.; He, Y.-B.; Li, B.; Kang, F. Suppressing Self-Discharge and Shuttle Effect of Lithium–Sulfur Batteries with V_2O_5-Decorated Carbon Nanofiber Interlayer. *Small* **2017,** *13*, 201602539.

(31) Liu, F.; Xiao, Q.; Wu, H. B.; Sun, F.; Liu, X.; Li, F.; Le, Z.; Shen, L.; Wang, G.; Cai, M.; Lu, Y. Regenerative Polysulfide-Scavenging Layers Enabling Lithium–Sulfur Batteries with High Energy Density and Prolonged Cycling Life. *ACS Nano* **2017,** *11* , 2697-2705.

(32) Bai, S.; Liu, X.; Zhu, K.; Wu, S.; Zhou, H. Metal–organic framework-based separator for lithium–sulfur batteries. *Nat. Energ.* **2016,** *1*, 16094.

(33) Ma, G.; Huang, F.; Wen, Z.; Wang, Q.; Hong, X.; Jin, J.; Wu, X. Enhanced

performance of lithium sulfur batteries with conductive polymer modified separators. *J. Mater. Chem. A* **2016,** *4*, 16968-16974.

(34) Fan, Y.; Yang, Z.; Hua, W.; Liu, D.; Tao, T.; Rahman, M. M.; Lei, W.; Huang, S.; Chen, Y. Functionalized Boron Nitride Nanosheets/Graphene Interlayer for Fast and Long-Life Lithium–Sulfur Batteries. *Adv. Energ. Mater.* **2017,** *7*, 201602380.

(35) Yang, Y.; Yu, G.; Cha, J. J.; Wu, H.; Vosgueritchian, M.; Yao, Y.; Bao, Z.; Cui, Y. Improving the Performance of Lithium–Sulfur Batteries by Conductive Polymer Coating. *ACS Nano* **2011,** *5*, 9187-9193.

(36) Li, W.; Zhang, Q.; Zheng, G.; Seh, Z. W.; Yao, H.; Cui, Y. Understanding the Role of Different Conductive Polymers in Improving the Nanostructured Sulfur Cathode Performance. *Nano Lett.* **2013,** *13*, 5534-5540.

(37) Fei, L.; Yoo, S. H.; Villamayor, R. A. R.; Williams, B. P.; Gong, S. Y.; Park, S.; Shin, K.; Joo, Y. L. Graphene Oxide Involved Air-Controlled Electrospray for Uniform, Fast, Instantly Dry, and Binder-Free Electrode Fabrication. *ACS Appl. Mater. Inter.* **2017,** *9*, 9738-9746.

(38) Chen, Z.; To, J. W. F.; Wang, C.; Lu, Z.; Liu, N.; Chortos, A.; Pan, L.; Wei, F.; Cui, Y.; Bao, Z. A Three-Dimensionally Interconnected Carbon Nanotube–Conducting Polymer Hydrogel Network for High-Performance Flexible Battery Electrodes. *Adv. Energ. Mater.* **2014,** *4*, 201400207.

(39) Liu, Z.; Parvez, K.; Li, R.; Dong, R.; Feng, X.; Müllen, K. Transparent Conductive Electrodes from Graphene/PEDOT:PSS Hybrid Inks for Ultrathin Organic Photodetectors. *Adv. Mater.* **2015,** *27*, 669-675.

(40) Kellici, S.; Acord, J.; Ball, J.; Reehal, H. S.; Morgan, D.; Saha, B. A single rapid

route for the synthesis of reduced graphene oxide with antibacterial activities. *RSC Adv.* **2014,** *4*, 14858-14861.

(41) Sun, D.; Jin, L.; Chen, Y.; Zhang, J.-R.; Zhu, J.-J. Microwave-Assisted In Situ Synthesis of Graphene/PEDOT Hybrid and Its Application in Supercapacitors. *ChemPlusChem* **2013,** *78*, 227-234.

(42) Islam, M. M.; Aboutalebi, S. H.; Cardillo, D.; Liu, H. K.; Konstantinov, K.; Dou, S. X. Self-Assembled Multifunctional Hybrids: Toward Developing High-Performance Graphene-Based Architectures for Energy Storage Devices. *ACS Cent. Sci.* **2015,** *1*, 206-216.

(43) Sun, Z.; Zhang, J.; Yin, L.; Hu, G.; Fang, R.; Cheng, H.-M.; Li, F. Conductive porous vanadium nitride/graphene composite as chemical anchor of polysulfides for lithium-sulfur batteries. *Nat. Commun.* **2017,** *8*, 14627.

(44) Shao, H.; Ai, F.; Wang, W.; Zhang, H.; Wang, A.; Feng, W.; Huang, Y. Crab shell-derived nitrogen-doped micro-/mesoporous carbon as an effective separator coating for high energy lithium-sulfur batteries. *J. Mater. Chem. A* **2017,** *5*, 19892-19900..

(45) Xiang, M.; Wu, H.; Liu, H.; Huang, J.; Zheng, Y.; Yang, L.; Jing, P.; Zhang, Y.; Dou, S.; Liu, H. A Flexible 3D Multifunctional MgO-Decorated Carbon Foam@CNTs Hybrid as Self-Supported Cathode for High-Performance Lithium-Sulfur Batteries. *Adv. Funct. Mater.* **2017,** *27*, 201702573.

(46) Zhao, T.; Ye, Y.; Lao, C.-Y.; Divitini, G.; Coxon, P. R.; Peng, X.; He, X.; Kim, H.-K.; Xi, K.; Ducati, C.; Chen, R.; Liu, Y.; Ramakrishna, S.; Kumar, R. V. A Praline-Like Flexible Interlayer with Highly Mounted Polysulfide Anchors for Lithium–Sulfur

Batteries. *Small* **2017,** *13*, 201700357.

(47) Lu, Y.; Gu, S.; Guo, J.; Rui, K.; Chen, C.; Zhang, S.; Jin, J.; Yang, J.; Wen, Z. Sulfonic Groups Originated Dual-Functional Interlayer for High Performance Lithium–Sulfur Battery. *ACS Appl. Mater. Inter.* **2017,** *9*, 14878-14888.

(48) Yang, J.; Chen, F.; Li, C.; Bai, T.; Long, B.; Zhou, X. A free-standing sulfur-doped microporous carbon interlayer derived from luffa sponge for high performance lithium-sulfur batteries. *J. Mater. Chem. A* **2016,** *4*, 14324-14333.

CHAPTER 4

BINDER FREE AND DIRECT DEPOSIT OF SULFUR ELECTRODE ENABLED BY AIR CONTROLLED ELECTROSPRAY PROCESS

Abstract

Lithium-sulfur batteries are one of the most promising energy storage technologies to replace commercial Li-ion batteries due to five-fold higher theoretical energy density, and lower cost. However, due to certain limitations, the technology is not ready to be deployed. To overcome som e of these, scientists have been extensively employing graphene oxide (GO) or graphene material to improve the electrochemical performance. In this work, we present a unique, novel, and facile method to deposit the active materials onto an aluminum collector by utilizing the Van der Waals interaction between graphene oxide and aluminum via an air-controlled electrospray (ACES) process. The role of conventional polymer binder was replaced by GO, resulting in a binder-free substrate. We demonstrated that the elimination of conventional polymer binder and resulting porous electrode surface from the ACES method resulted in higher discharge capacity and retention over 100 cycles. This ACES technique offers potential for improving the overall energy density of sulfur and being adapted for commercialization in the energy storage industry.

Introduction

Due to the rapid development of electronics and electric vehicles, it is imperative to develop new technology for energy storage applications. Lithium-sulfur (Li-S) is one of the promising candidates for energy storage applications because it possesses high theoretical capacity and energy density at 1,670 mAh g^{-1} and 2,500 kW kg^{-1}, respectively [1–3]. Also, the low cost and environmentally benign nature of sulfur components are attractive from an economic and environmental perspective [4,5]. Despite these advantages, several obstacles persist that hinder the commercialization of lithium-sulfur technology. For example, expansion and contraction of active materials during the discharge/charge process, rapid capacity fading due to polysulfide migration, and insulating properties of the sulfur material itself [6–8].

Many approaches have been conducted to circumvent the problems by improving electrical conductivity and trapping the polysulfide species. The most popular approach is employing carbonaceous material, such as: bimodal mesoporous carbon [9–11], carbon nanotubes [12–14], conductive polymer like carbon nanofiber [15–18], PEDOT:PSS [19,20], graphene oxide (GO) [21,22], and graphene materials within the cathode itself [23–25]. In this last approach, embedding interlayers or applying surface modification is very useful for high sulfur loading [16,18,26]. Addition of GO is one of the most popular methods due to its ability to capture polysulfide by acting as a physical barrier, and also through chemisorption by polar-polar interactions. Binding between oxygen functional groups and sulfur polysulfide has been proven to maintain high capacity retention [22,23,27–31]. However, researchers often overlook another potential attribute of graphene oxide. Most of the

current literature focuses on utilizing the oxide content to capture polysulfide as opposed to using GO's other efficacies to anchor active materials onto the aluminum electrode.

In 2015, layer by layer reduced graphene oxide (rGO) deposition onto the aluminum electrode by an electrospray method was reported [32,33]. The binding interaction between GO/rGO and aluminum oxide layer was further asserted using density functional theory [34]. These ideas inspired us to develop an advanced technique to deposit graphene oxide and active sulfur materials simultaneously. Previously, we successfully implemented our novel air-controlled electrospray (ACES) technique for Li-ion batteries and high loading sulfur in Li-S technology [16,35]. This approach permits coating of diverse materials on various surfaces. Herein, we present a novel, facile, and scalable method of the deposition process that utilizes GO as a binder and polysulfide anchor. In general, our electrode fabrication method is only a two-step process: ACES followed by heat treatment. In this manner, we were able to achieve sulfur deposition on aluminum collector without conventional polymer adhesive. In addition, the quick dry spray process eliminates the cracking that results from a typical drying method [36]. As for the conductive carbon, we implemented commercial Ketjen Black with pulverized mesoporous carbon nanofiber (MPCNF) and GO. The overall concentration of GO was less than 1%. To further improve the electrochemical performance of the cell, we also replaced the binder content with commercially available graphene solution to promote electron pathways and sulfur utilization. Incorporation of graphene in the electrode was carried out with the ACES process (ACES-Gr)

For the reference system, a conventional slurry coated electrode with binder was prepared. We utilized lithium polyacrylate (LiPAA) as a polymer binder because LiPAA has shown the best performance among polyvinylidene fluoride (PVDF), polyvinylpyrrolidone (PVP), polyethylene imine (PEI), PVP:PEI (5:1), and Polyaniline (PANI) [37]. The composition of variables of interest is summarized in Table 1 below.

Table 4.1. Summary of the cathode composition with different approach

Technique	**Sulfur (%)**	**Carbon Composite – Ketjen Black : MPCNF+rGO (1:1) weight ratio (%)**	**Binder LiPAA (%)**	**Graphene (%)**
Conventional slurry coating method (SC)	56	34	10	0
Air-controlled electrospray method (ACES)	56	44	0	0
Air-controlled electrospray method (ACES-Gr)	56	34	0	10

Methods

Fabrication of MPCNF+GO powder

1.2 g of polyacrylonitrile (PAN, MW = 150,000, Sigma Aldrich), 0.8 g of polymethylmethacrylate (PMMA) (MW = 15,000 Sigma Aldrich), 0.3 g of tetraethyl

orthosilicate (TEOS) (Reagent Grade, Sigma Aldrich), and 0.05 g of Zinc Chloride ($ZnCl_2$) (Reagent Grade, Amresco) were dissolved in 12 mL of dimethylformamide (DMF) (Alfa Cesar) to form 13.7 wt % of polymer content. The solution was stirred for 72 hours at 65^oC to enhance polymer crosslinking. Air-controlled electrospinning was used to spin 6 ml of the polymer solution with a PHD 2000 Infusion syringe pump (Harvard Apparatus) and a coaxial needle at room temperature. The solution was supplied to the inner 12-gauge needle, and 12 psi air flow rate was applied through the 17-gauge outer shell. The distance between the nozzle tip and aluminum current collector was 30 cm. Positive potential 15 kV was induced to the outer nozzle, and solution feeding rate was set at 0.1 ml min^{-1}. The resulting fiber was peeled and folded to 4 X 6 inches for heat treatment. Initially, the fiber was subjected to stabilization at 280^oC for 2 hours under stagnant air with a ramp rate of 5^oC min^{-1}, followed by carbonization at 900^oC for 2 hours with a ramp rate of 5^oC min^{-1} under N_2 flow, and finally activation at 900^oC for 2 hours with a ramp rate of 5^oC min^{-1} under CO_2 flow. Commercial graphene oxide solution (Dongjin Semichem) was diluted with distilled water to 6 mg ml^{-1}. Then, 5 ml of the solution was extracted and sprayed onto activated MPCNF substrate using ACES method. The positive potential was applied at 25 kV, the distance between the nozzle tip to the collector was 30 cm, solution feeding rate was set at 0.1 ml min^{-1}, and 20 psi airflow was applied through the outer stainless-steel nozzle. After spraying, the surface color of the MPCNF turned into a dark grey, indicating successful coating of GO on MPCNF. Finally, the obtained MPCNF coated GO sheets were pulverized using a ball mill for 15 minutes to form a fine powder.

Preparation of Slurry Coated Electrode (SC)

Initially, 0.56 g of active sulfur material (Spectrum Chemical) was mixed with 0.17 g of Ketjen Black (AkzoNobel) and 0.17 g of MPCNF+GO powder. Then, the mixture was heat treated under air at 155^{o}C for 12 hours to ensure sulfur infiltration and simultaneously reduce the graphene oxide. LiPAA was synthesized by mixing 5 wt % of a polyacrylic acid (PAA) (MW = 450,000, Sigma Aldrich) in H_2O solution and 5 wt % of a 1:1 lithium hydroxide (LiOH) (Powder, Reagent Grade Sigma Aldrich) in H_2O solution and stirred it overnight as previously reported [38]. Then, 0.1 g of the LiPAA solution was thoroughly mixed with the sulfur-carbon composites in a ball mill for 10 minutes. The slurry paste was then cast onto a carbon coated aluminum electrode.

Preparation of Sulfur-Carbon Solution without Graphene (ACES)

Active sulfur material, Ketjen Black, and MPCNF+GO powder were mixed and heat treated as reported above. Afterward, the mixture was dissolved in a water and isopropanol solvent (8:2 weight ratio) at a concentration of 10 mg ml^{-1}.

Preparation of Sulfur-Carbon Solution with Graphene (ACES-Gr)

A mixture of active sulfur material, Ketjen Black, and MPCNF+GO powder was prepared and heat treated as previously stated. Afterward, 0.25 g of commercial 4% wt

graphene solution (ACS Nano) is added to the mixture. Finally, the mixture is dissolved in 10 ml water and isopropanol solvent at 8:2 ratio.

Active Materials Deposition

Similarly, 10mL of sulfur-carbon solution (with or without graphene) was sprayed using onto the aluminum current collector using the ACES process. The voltage applied was 25 kV, distance from the nozzle tip to current collector was 15 cm, convective airflow rate was 25 psi, and solution pump rate was 0.1 ml min^{-1}. After all the dry solutions were deposited onto the aluminum collector, the electrode was punched into 1.75 cm diameter disks. Typical active sulfur loading was around 1 mg cm^{-2}.

Electrolyte Composition

The electrolyte was 1 M of bis(trifluoromethane)sulfonimide lithium salt (LiTFSI) and 0.1 M of lithium nitrate ($LiNO_3$) in a 1:1 volume ratio of 1,2-dimethoxyethane (DME) and 1,3-Dioxolane (DOL). All were purchased from Sigma Aldrich.

Characterization Methods

Fourier Transform Infrared Spectra were recorded with a Bruker Vertex V80V Vacuum FTIR system using an average of 64 scans with a resolution of 4 cm^{-1}.

Thermogravimetric analysis was carried out with a TA Instruments Q500 at a heating rate of 10 ^{o}C min^{-1} under an N_2 atmosphere. X-ray diffraction analysis was conducted with a Bruker D8 Advance ECO powder diffractometer from 5^{o} to 60^{o} at a scan rate of 0.1^{o} s^{-1}. Scanning electron microscopy (SEM) images and energy dispersive X-ray spectroscopy (EDS) mapping were taken using an LEO 1550 FESEM. X-ray photoelectron spectroscopy measurements were conducted with a Surface Science instrument equipped with a monochromatic Al Kα X-ray source (1468.6 eV). Electrochemical characterizations of the coated separator were performed using 2032-type coin cells consisting of Li metal anode (MTI Corporation). All cells were assembled in an argon-filled glove box. Cyclic voltammetry and electrochemical impedance spectroscopy (EIS) test were performed using a potentiostat (Princeton PARSAT 4000). Galvanostatic charge/discharge cycles were carried out in the voltage range of 1.8-2.8 V using a battery cycler (MTI Corporation) at room temperature. All current densities and specific discharge capacities calculated in this study were based on sulfur mass.

Results

Heat Treatment Sulfur Encapsulation

Heat treatment at 155^{o} C is purported to encapsulate the sulfur inside the carbon composite, as shown in previous literature [39,40]. The GO content is only around 1% of the overall composition, which is essential to ensure that the insulating properties of GO do not hinder electron pathways. To confirm that there are no chemical reactions

between sulfur and carbon composites after heat treatment in the system, we conducted high-resolution spectra of XPS and FTIR (Fig 4.1). Stagnant peaks before and after heat treatment from XPS shows that no chemical interaction happens between terminal sulfur and oxygen group from GO [41]. From FTIR results, no distinct peak is formed after thermal treatment, which also clarifies the absence of chemical reaction during sulfur infusion [21]. Wide-angle XRD patterns in Fig 4.2 show a sharp peak for sulfur components around 23^{o}. Carbon composite (MPCNF + GO + KB) displays several small peaks from 8^{o} to 60^{o}. The absence of a peak at 10^{o} two theta shows that the content of GO is insignificant in the system [42]. After mixing the sulfur with the carbon composite for air-controlled electrospray (AC), their respective peaks were observed on a single spectrum. After the heat treatment for sulfur infusion, the sharp peak at 23^{o} two theta disappears, implying that the bulk of sulfur crystallinity turns into amorphous sulfur. Moreover, when graphene is incorporated to the ACES system (ACES-Gr), a sharp peak at 27^{o} is observed, indicating the presence of graphitic layer in the system [43].

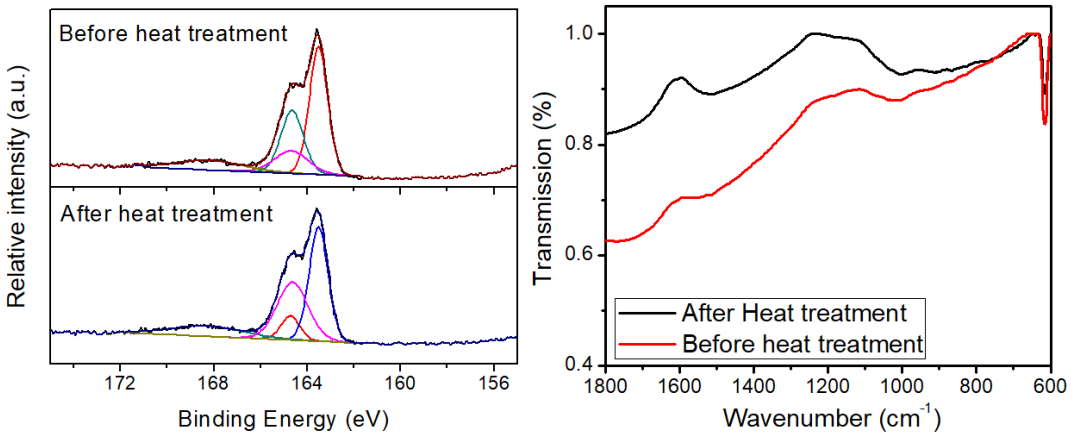

Figure 4.1) High resolution of S_{2p} before and after heat treatment (left) and FTIR spectra before and after heat treatment (right)

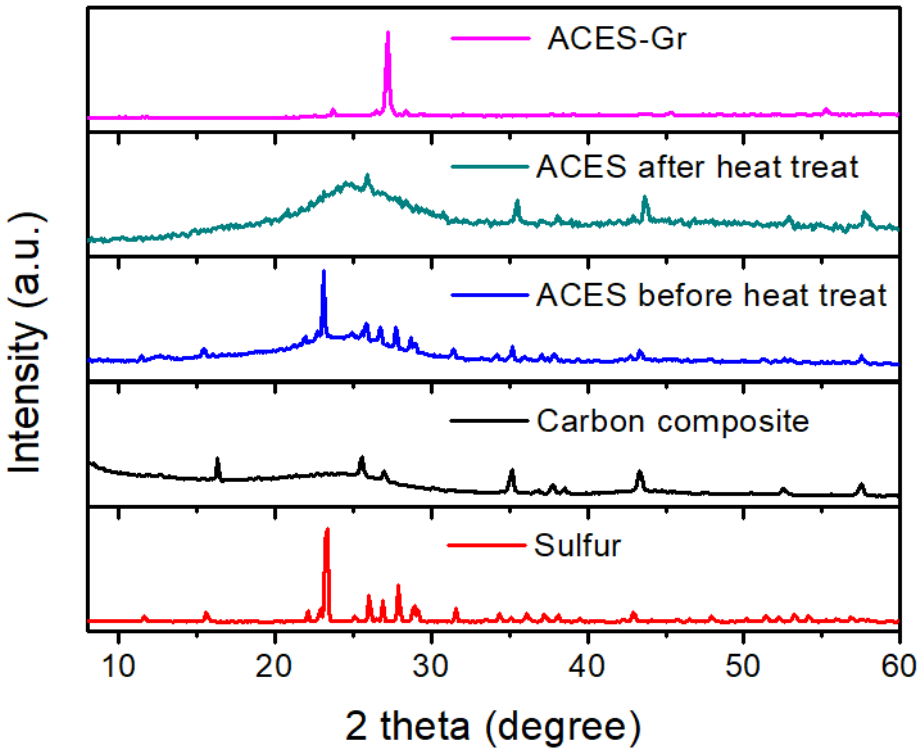

Figure 4.2) XRD characterization of pristine sulfur and carbon composite, then a mixture of sulfur and carbon composite before and after heat treatment, and the presence of graphene in the system.

Air Controlled Electrospray Process

The schematic process of air-controlled electrospray and conventional electrospray are illustrated in Figure 4.3a & c below. As opposed to conventional electrospray process, the air-controlled electrospray (ACES) utilizes a convective air flow jet to accelerate the drying and deposition process. The nozzle is comprised of two concentric cylinders. The solution is ejected from the inner cylinder, while the air propels through outer nozzle, which is connected to a high voltage source. Our studies indicate that the impinging dry air of the air-controlled electrospray process tends to form smaller charged droplets and evaporate solvent faster, resulting in dry solute deposited on the current collector. The evaporation is accelerated due to higher surface area exposed to the surrounding dry air. In general, a higher voltage, faster airflow rate, and longer distance between the nozzle tip and current collector enhance the evaporation rate and reduce the droplet sizes of the solution. If evaporation rate is too slow, wet solutions are formed on the current collector, which cause poor particle dispersion and may disrupt uniformity. However, if evaporation rate is too fast, solutes might disappear along with the solvent, causing discontinuity and disorder in the material on the current collector. Images of the air-controlled sprayed electrode without (ACES) and with graphene (ACES-Gr) is displayed in Figure 4.3b & d below. Poor dispersion and non-uniform deposition are observed from the conventional electrospray process, whereas a smooth and continuous film is attained with the air-controlled electrospray process. After the ACES process finishes, the electrochemical performance of the resulting dry solutes can be tested immediately, contrary to solution casting that

requires additional drying. This also makes ACES an effective method for scaling up. Image of the actual ACES process is displayed in Figure 4.4 below. The deposition is presumably enabled by the interaction between charged graphene oxide and an aluminum oxide film on the current collector as mentioned in previous reports [33,34].

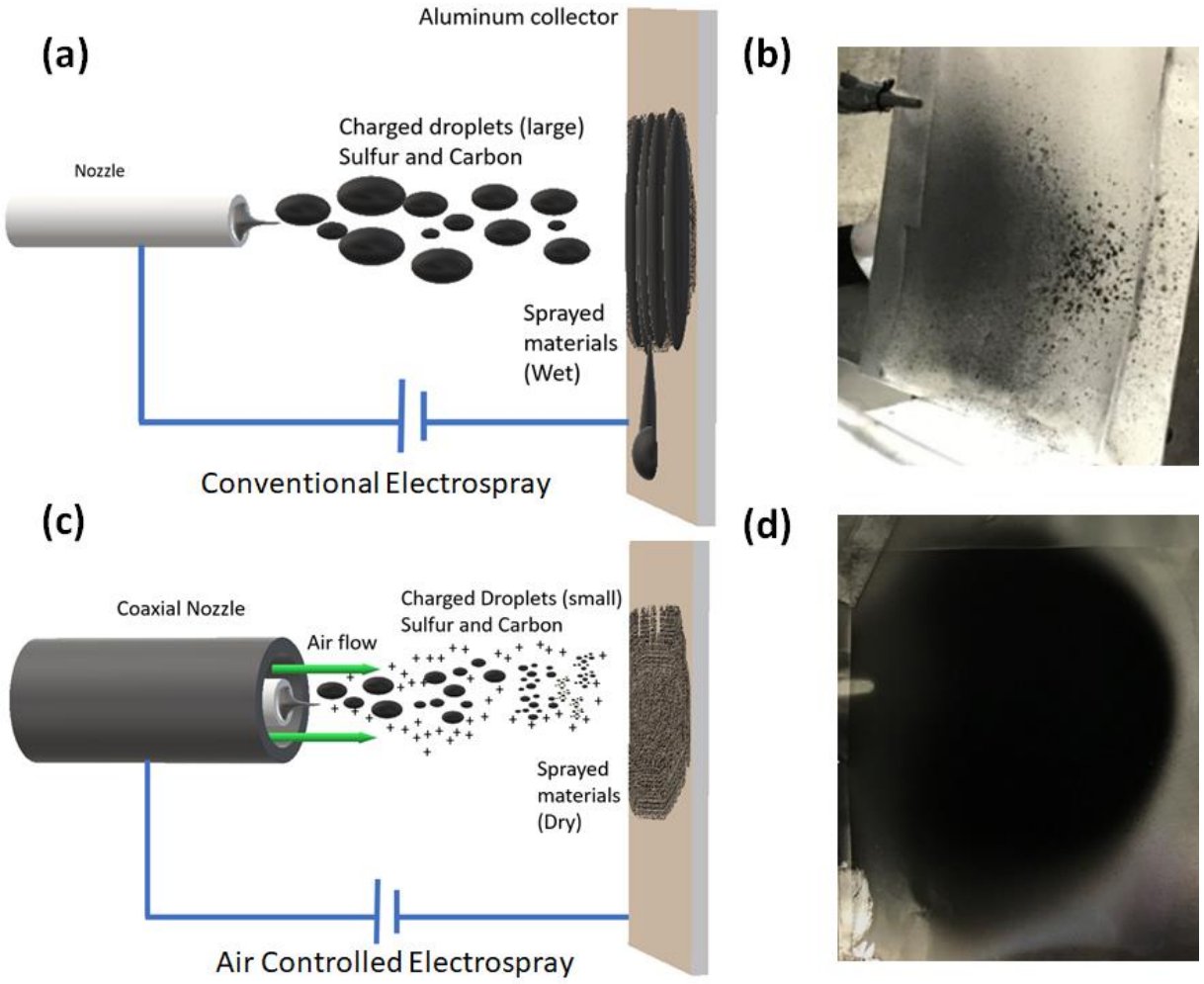

Figure 4.3 Schematic illustration of a) conventional electrospray c) air-controlled electrospray (ACES) and material deposited images right after b) conventional electrospray and d) air-controlled electrospray (ACES).

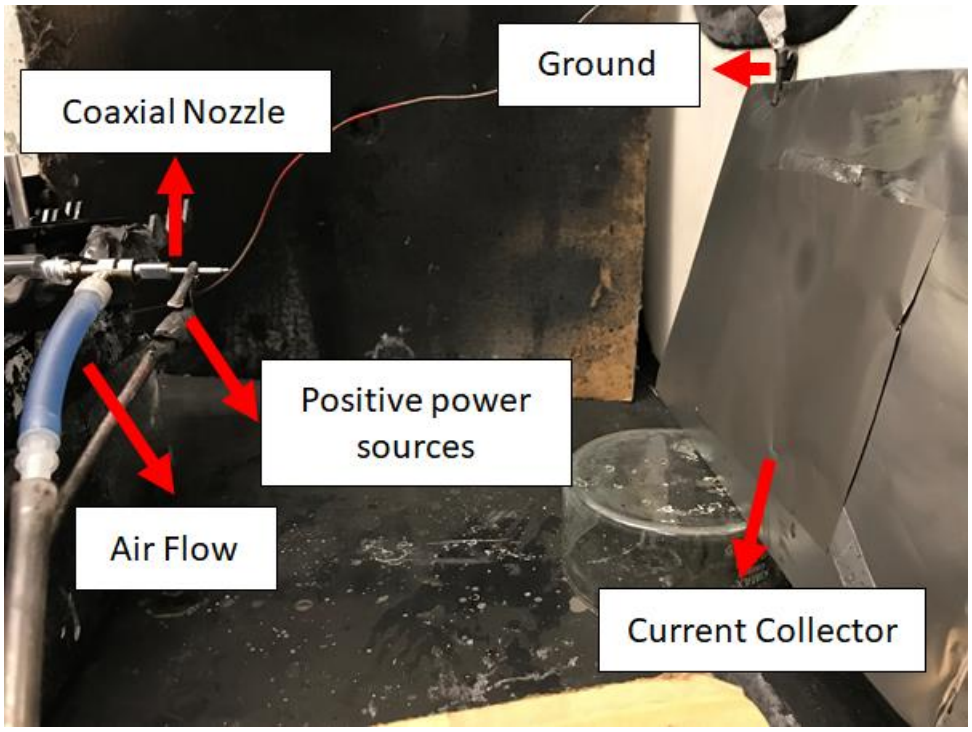

Figure 4.4) Digital image of air-controlled electrospray process

Surface Morphology and Characterization.

The morphologies between conventional slurry coating (SC) and ACES can be easily distinguished from SEM images (Fig 4.5). Top view and cross-sectional images of the SC technique (Fig. 4.5a-b) show a dense and smooth film with cracking. This inevitable cracking happens during the drying process. The fracture amplifies as the sulfur loading increases [36]. By looking at the cross-sectional images, the cracking only appears on the surface. An intact structure is observed beneath the surface, which is presumably due to low sulfur loading. However, in the ACES technique (Fig. 4.5c-d), voids and rough surfaces are observed while carbon interconnections are preserved. A porous morphology is beneficial to the sulfur electrode as it accommodates the

sulfur expansion during cycling to preserve the structure [44]. Moreover, it also provides good accessibility of electrolyte to active sulfur materials. In the SC method, uniform thickness and smooth surfaces are maintained because a fixed gap is applied from the doctor blade. In ACES process, thickness is a function of flow rate, distance, and convective airflow. These factors make it extremely difficult to produce a flat, smooth, and continuous structure. Despite the difference in morphology, sulfur and carbon are uniformly well-dispersed for both systems as depicted in EDS (central images of Fig. 4.5). In most electrochemical systems, uniform state of the electrode is a crucial factor in obtaining consistent and accurate results.

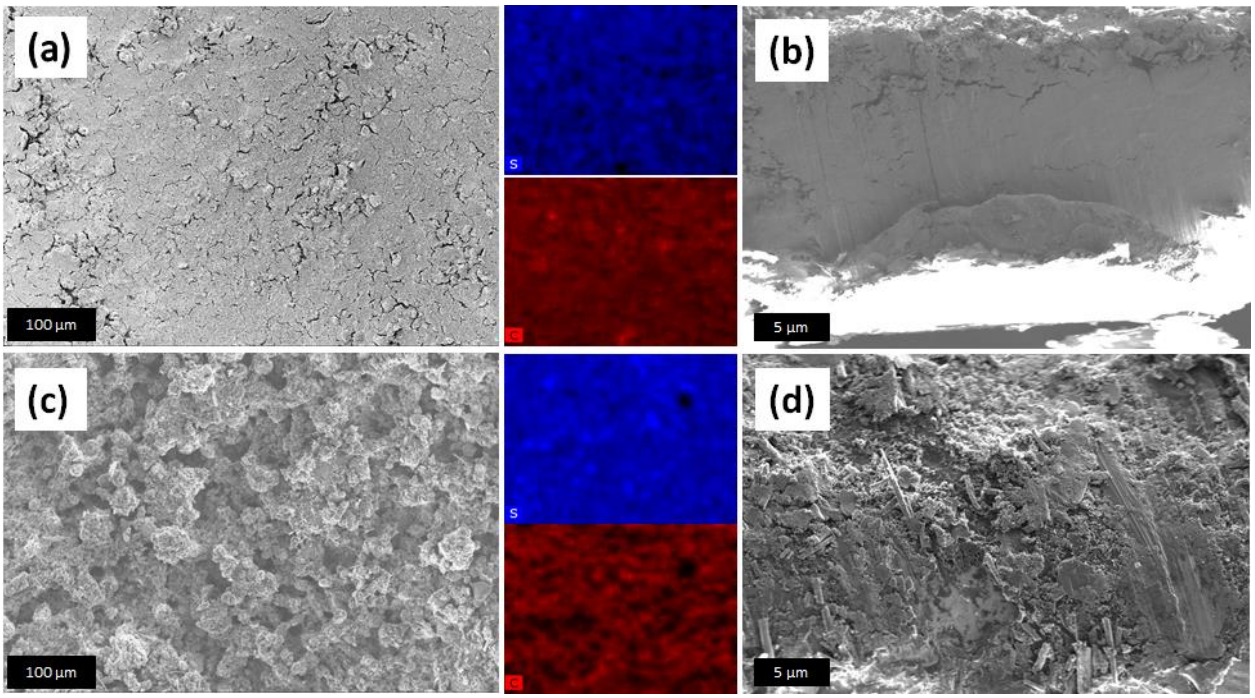

Figure 4.5. The morphologies of top view SEM images with SC (a) and ACES (b). Cross-sectional SEM images of SC (c) and ACES (d). EDS mapping of sulfur and carbon correspond to top view images of part a and c.

The incorporation of graphene solution results in structural changes of sulfur-carbon active materials. High-resolution SEM measurement was carried out to distinguish structural differences from the incorporation of graphene sheets. From the ACES image of Figure 4.6, it is seen that sulfur is aggregated on the carbon nanofiber substrate. In the ACES-Gr image, thin planar graphene sheets cover the surface of active materials. This encapsulation is self-assembled during the spray process.

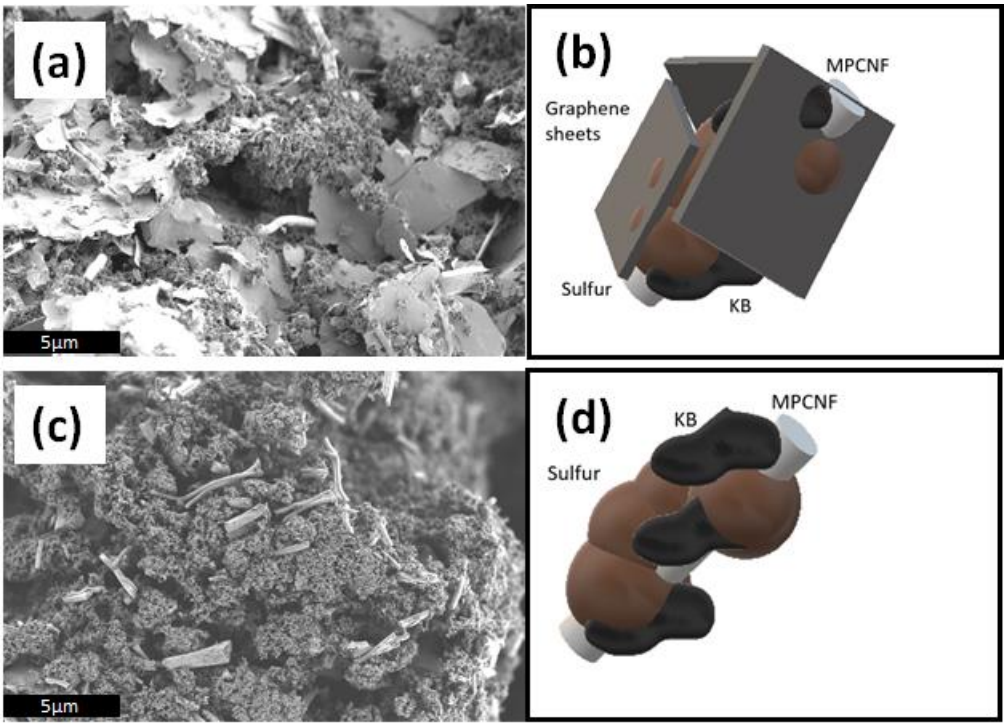

Figure 4.6. High magnification SEM images and schematic illustration of ACES-Gr (a,b) and ACES system (c,d).

Electrochemical Performance

Cyclic voltammogram (CV) profiles of SC, ACES, and ACES-Gr are displayed in Figure 4.7 below. Cyclic voltammetry was conducted from 2.8 V to 1.6 V

at a scan rate 0.1 mV s^{-1}. Two reduction peaks are observed in all samples. The first reduction peak at around 2.2 V corresponds to the reduction of S_8 to higher order polysulfides (Li_2S_x, $4 \leq x \leq 8$), and the second reduction at 2.0 V is ascribed to a further reduction to insoluble Li_2S [45,46]. In the SC and ACES systems, the first reduction peak happens at around 2.2 V. After the first cycle, the peak shifts to around 2.3 V, and the second reduction peak stabilized to 2.0 V after several cycles suggesting a higher kinetic barrier for the direct reduction of bulk-sized commercial sulfur powder to polysulfides. By replacing binders with graphene sheets, the first and second reduction peaks of ACES-Gr were maintained at 2.3 V and 2.0 V for all cycles, which implies superior stability in lithium-sulfur performance. In addition, replacing graphene with binder produces sharp reduction peak at 2.0 V, indicating excellent utilization of active materials from the sulfur-carbon network. The clear distinction can be detected from the oxidation peak between SC and ACES. The SC technique only has one peak at 2.42 V, whereas the ACES process has two oxidation peaks at 2.38 at 2.42 V after the first cycle. A singlet anodic peak at 2.4 V confirms the oxidation of insoluble polysulfide to Li_2S_8 [46], whereas doublet anodic peak at 2.38 V and 2.42 V implies complete conversion to S_8 [47].

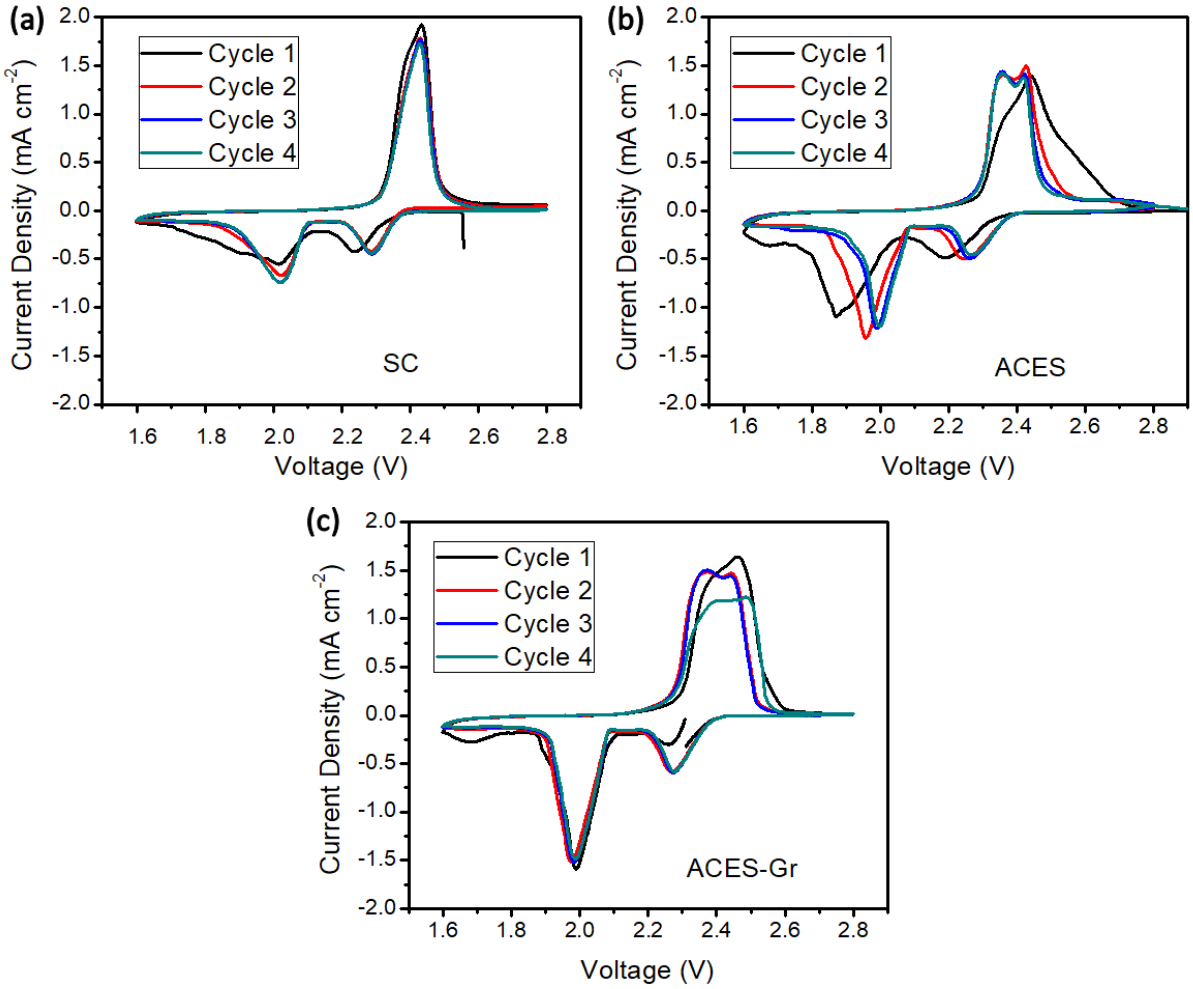

Figure 4.7) Cyclic voltammogram of various techniques a) SC b) ACES c) ACES-Gr.

To elucidate the advantage of ACES deposition, electrochemical impedance spectroscopy (EIS), cycling performance, and rate capability were carried out (Fig 4.8a-c). The EIS result from 10^7 Hz to 0.01 Hz at 5 mV amplitude is displayed in Figure 4.8a. The ACES system had a slightly shorter x-intercept and half semicircle as opposed to a conventional SC system, which suggests that the replacement of binder with carbon decreases interfacial and charge transfer resistances of the cells [48]. Then, the integration of graphene reduces the semicircle and x-intercept even further due to the excellent electrical conduit from the carbon planar. This phenomenon ensures better electrochemical environment and higher utilization of the active material, which shows an agreement with the CV data from Figure 4.7.

Prior to electrochemical cycling, thermogravimetric analysis (TGA) was carried out to justify that the composition of sulfur is around 56 % after the spraying process (Fig. 4.9). To evaluate the electrochemical performance, electrodes produced by SC, ACES, and ACES-Gr with sulfur loading of 1 mg cm^{-2} were cycled from 1.8 V to 2.8 V at the C/4 rate for cyclability testing and different current densities to test rate capability (Fig 4.8b & c). At a rate of C/4, the initial capacity of 849.51 mAh g^{-1}, 926.29 mAh g^{-1}, and 1076.43 mAh g^{-1} are obtained for the SC, ACES, and ACES-Gr cells respectively. Improved cycling performance compared to the SC technique is clear. The ACES system delivers good capacity retention over 99 cycles at C/4 with a fade rate of 0.31% and 0.33% with and without graphene addition, whereas the SC method declines at 0.44% per cycle. The cells from the ACES system also display remarkable discharge capacity at a higher rate. They are discharged/charged at various current densities from C/10 to 2C for five cycles at each rate. The results show that as

the rate increases, the difference of discharge capacity becomes more apparent. By replacing insulating binder with more electrically conductive carbon, the reversible capacity is increased from 142 mAh g^{-1} to 348 mAh g^{-1} at 2C discharge rate. Moreover, by integrating graphene sheets into the cell, the reversible capacity is further improved to 550 mAh g^{-1} at 2C. This shows that electron pathway and lithium-ion accessibility are critical in achieving remarkable capacity at higher current. Overall, the ACES system achieves higher discharge capacity due to favorable kinetics from higher electronic conductivity and excellent electrolyte accessibility because of the rough and porous cathode structure.

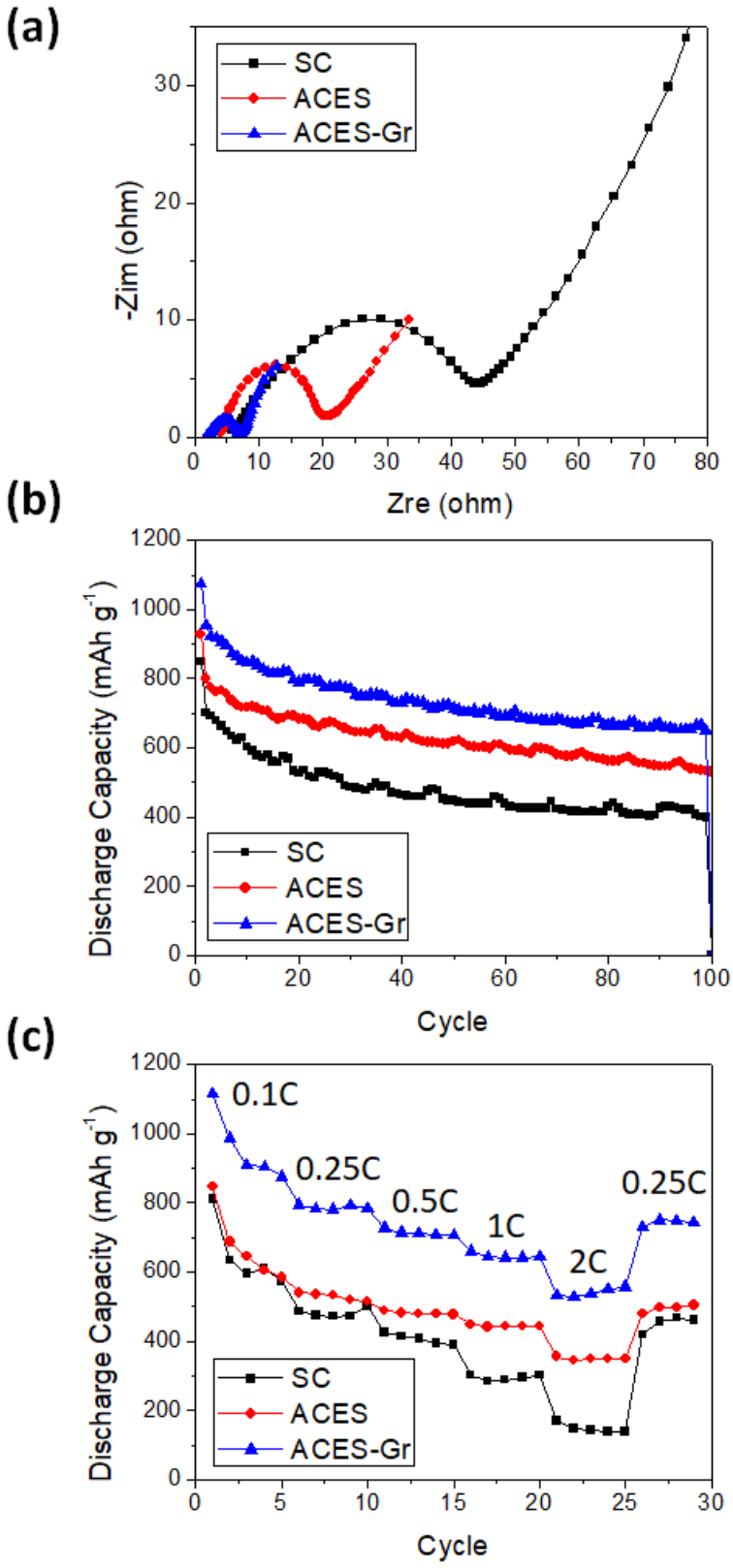
(a)
SC
ACES
ACES-Gr
-Zim (ohm)
Zre (ohm)
(b)
Discharge Capacity (mAh g-1)
Cycle
(c)
0.1C
0.25C
0.5C
1C
2C
0.25C

Figure 4.8a) Impedance spectra b) cycling performance at 0.25C rate (1C = 1670 mA g^{-1}) and c) rate capability of deposition methods.

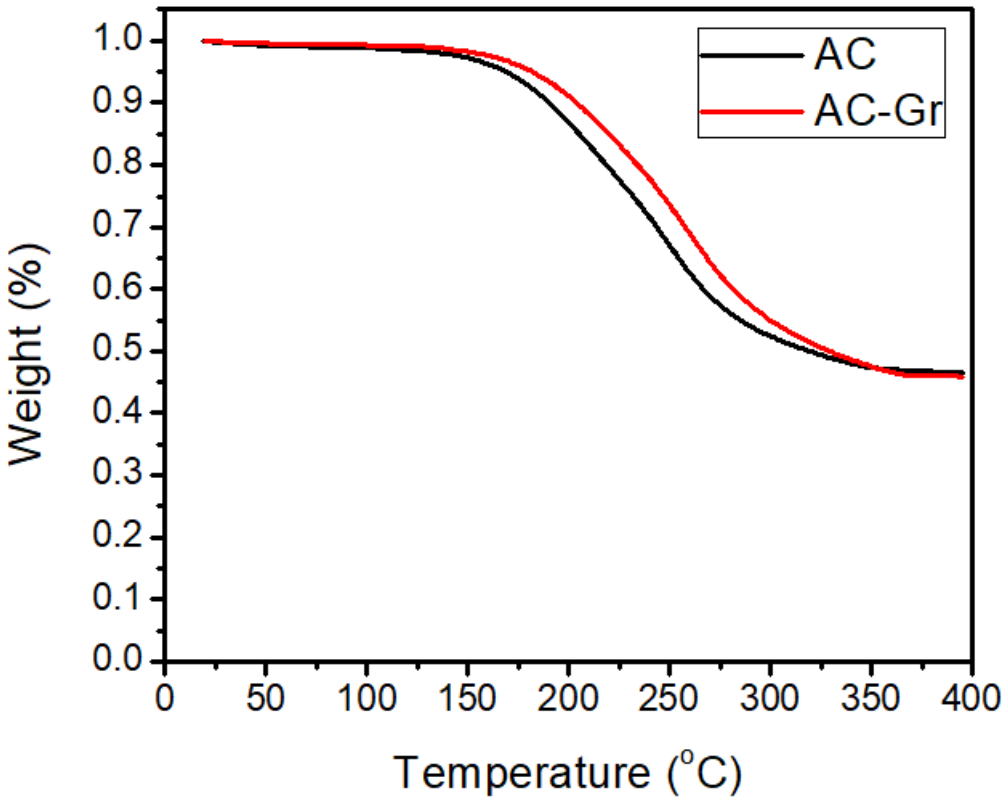

Figure 4.9) Thermogravimetric analysis of ACES and ACES-Gr after deposition on current electrode. Similar value around 56% indicated that composition was properly maintained after spray process.

Post-Mortem Analysis

After the cell finished cycling, we conducted SEM and high-resolution S_{2p} spectra to investigate morphologies and polysulfide profiles (Fig. 4.10). The SEM images show that the number of rifts increased, the gaps widened, and particles aggregated more.

These presumably occur during continuous discharge and charge because the compact structure does not accommodate volume expansion. The expansion induces constant stress among neighboring particles during the discharge/charge process, resulting in cracking and more structure disorder. Surprisingly, the ACES structure becomes more compact after 100 cycles of charge/discharge process. The pores are filled with sulfur-carbon composite. Cracking is observed after cycling, but less apparent and ubiquitous compared to the conventional slurry coating process. As for graphene incorporated electrode, the structure is completely intact and coarse, which indicates excellent trapping of polysulfide species. A clear distinction of morphology at various resolutions before and after cycling is displayed in Figure 4.11.

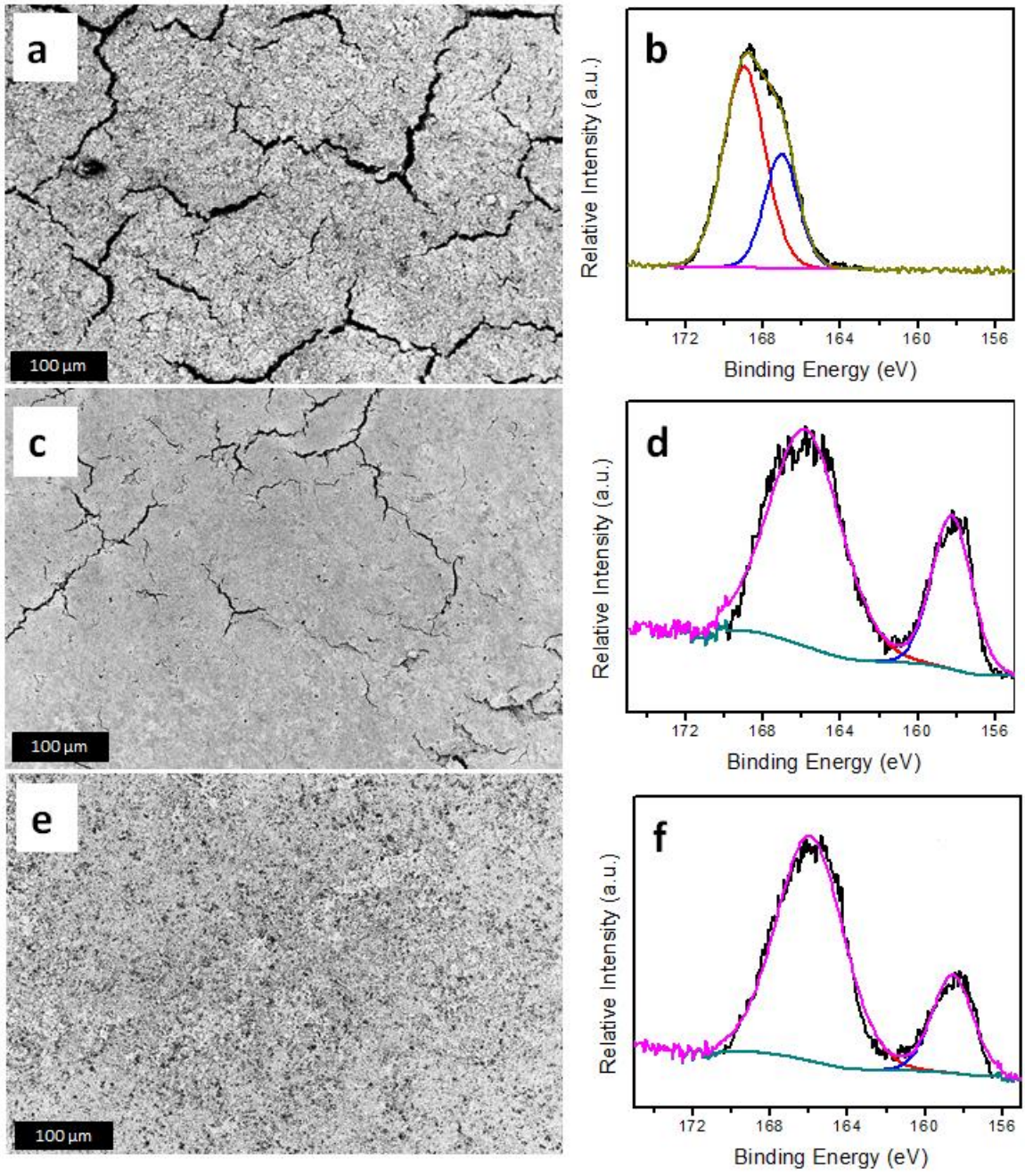

Figure 4.10) SEM images of sulfur cathode after cycling from a) SC c) ACES e) ACES-Gr. High-resolution s_{2p} of sulfur cathode after cycling from b) SC e) ACES f) ACES-Gr.

We conducted high-resolution S_{2p} spectra after finished cycling to add more features to ACES process (Fig. 4.10b,d,f). Surprisingly, both the ACES and ACES-Gr exhibit two peaks at around 165.7 and 158.4 eV, whereas the SC process only displays one sharp peak at 168.7 eV with a shoulder on the right-hand side at 166.9 eV. The peaks at 165.7 eV can be attributed to sulfonyl residue from the LiTFSI salt and sulfur oxide species from electrolyte decomposition, and the peak at 158.4 eV corresponds to insoluble polysulfides, Li_2S_2 and Li_2S [49,50]. Absence of the second peak from SC technique entails the possibility that lithium polysulfide completely detached and migrated to the lithium anode.

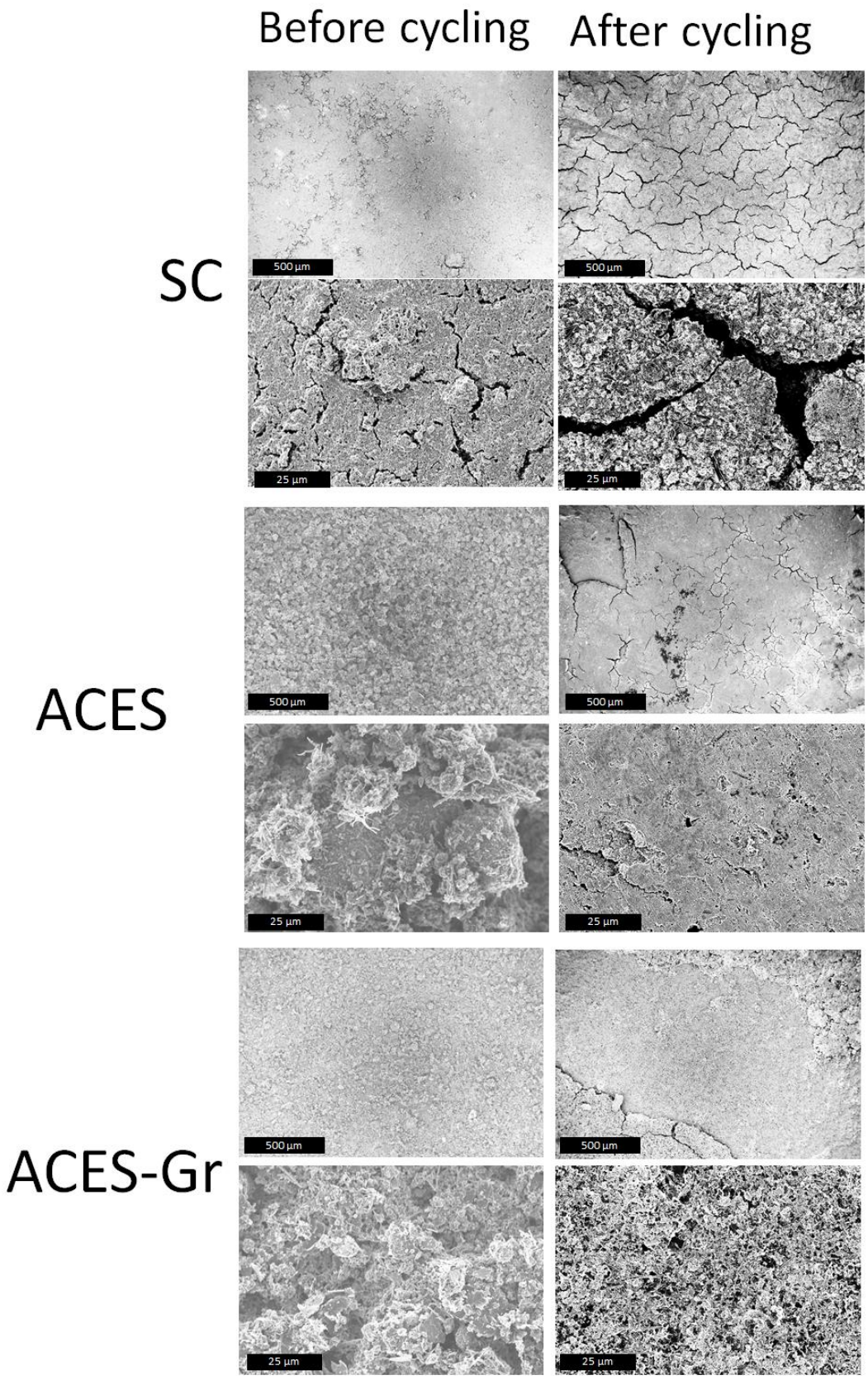
Before cycling
After cycling
SC
ACES
ACES-Gr
500 µm
25 µm

Figure 4.11) SEM images of sulfur cathode morphology from various deposition techniques before and after cycling at low and high resolution.

The SEM images and EDS mapping on lithium anodes confirm the migration of polysulfide onto the lithium surface (Figure 4.12). In the SC system, the lithium anode surface shows intense cracking and polysulfide coverage. However, in the ACES system, fewer bulk polysulfides are deposited on the anode, suggesting that morphology is important in suppressing the migration of polysulfide. Moreover, the ACES-Gr system displays significantly less number of particles and sulfur distribution as observed in the EDS spectra. From this outcome, we speculate that rough morphology has a beneficial role in inhibiting the polysulfide shuttle effect. As the tortuosity increases from surface area roughness, the path for polysulfides to the anode side is delayed, and they are ultimately trapped inside the carbon composites structures. Also, the encapsulation of sulfur by a graphene composite adds an extra barrier for the diffusion of soluble sulfur to the anode side, which causes significantly less insoluble polysulfide deposited onto the lithium anode.

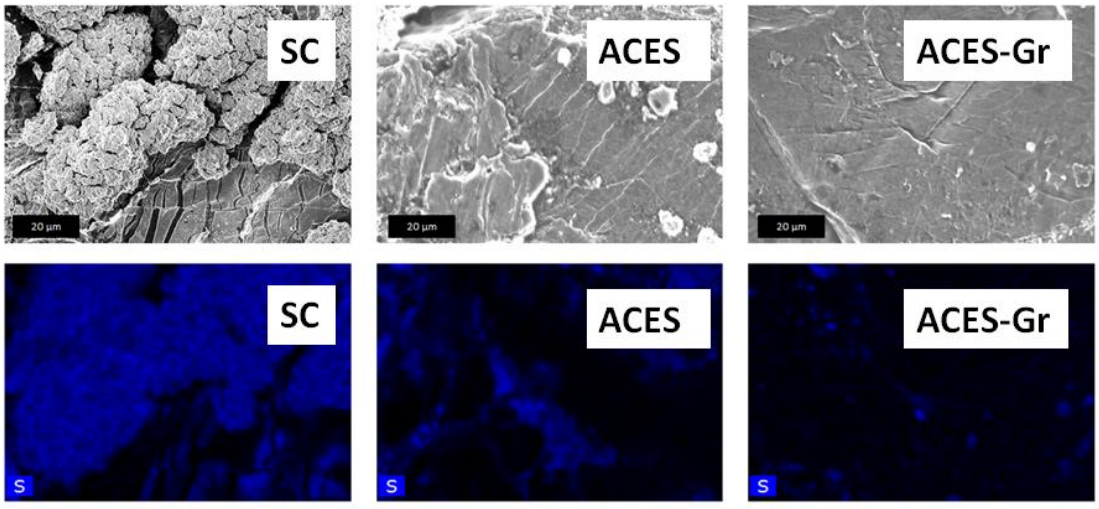

Figure 4.12) SEM images and EDS mapping of sulfur on lithium anode from various deposition techniques after cycling.

From this phenomenon, we notice that an inherent cathode structural configuration also influences the lithium-sulfur electrochemical performance and shuttling effect. For the SC system, a more compact cathode structure explains lower sulfur utilization because less active materials are exposed to the electrolyte, and the soluble polysulfides that form on the interfacial surface cause the nuclei to escape easily from the cathodes. However, for the ACES system, greater accessibility of electrolyte and sulfur particles ensures higher active material utilization and better retention due to more sulfur particles reacting with lithium ions. Greater tortuosity interferes with the polysulfide migration to the lithium anode.

As the ACES system introduces binder free and a unique morphology, it creates many opportunities to advance electrochemical research. This ACES system allows deposition of diverse materials on various surfaces. High sulfur loading is necessary to compete with the current lithium-ion technology, and ACES offers potential to improve the total sulfur loading while maintaining high volumetric energy density. However, incorporation of the binder is paramount to adhere higher amount of active materials on the current collector. Therefore, modified conductive polymer binder is needed to optimize the lithium-sulfur performance.

Conclusion.

The air-controlled electrospray process offers many benefits over the slurry casting method. The removal of binder, increased tortuosity, and improved pore mechanical structure enhance the electrical conductivity, electrolyte accessibility, and sulfur adsorption, which ultimately improves lithium-sulfur electrochemical performance. In addition, the elimination of a drying step avoids surface cracking and offers the potential for scaled up processes. A safety concern is also mitigated by replacing common dangerous solvent for sulfur deposition (N-Methyl-2-pyrrolidone or Carbon disulfide or chloroform) with more relatively benign solvent (80% water and 20% isopropanol). This novel system exhibits a potential for energy storage applications.

ACKNOWLEDGMENTS

This work was partly funded by EIC Labs (Cornell CCMR ICP No. M01-9124) and Axium Nano, LLC (Cornell OSP No. 80674). All the material characterizations were obtained via facilities at the Cornell Center for Materials Research (part of NSF MRSEC Program, Grant DMR 1120296).

REFERENCES

[1] S. Urbonaite, T. Poux, P. Novák, Adv. Energy Mater. 5 (2015).

[2] A. Manthiram, S.-H. Chung, C. Zu, Adv. Mater. 27 (2015) 1980–2006.

[3] J. Lochala, D. Liu, B. Wu, C. Robinson, J. Xiao, ACS Appl. Mater. Interfaces 9 (2017) 24407–24421.

[4] Y.X. Yin, S. Xin, Y.G. Guo, L.J. Wan, Angew. Chemie - Int. Ed. 52 (2013) 13186–13200.

[5] D. Eroglu, K.R. Zavadil, K.G. Gallagher, J. Electrochem. Soc. 162 (2015) A982–A990.

[6] A. Manthiram, Y. Fu, Y.-S. Su, Acc. Chem. Res. (2012).

[7] A. Manthiram, Y. Fu, Y.-S. Su, Acc. Chem. Res. 46 (2013) 1125–1134.

[8] D. Bresser, S. Passerini, B. Scrosati, Chem. Commun. (Camb). 49 (2013) 10545–62.

[9] G. He, X. Ji, L. Nazar, Energy Environ. Sci. 4 (2011) 2878.

[10] M. Rao, X. Song, E.J. Cairns, J. Power Sources 205 (2012) 474–478.

[11] J. Song, T. Xu, M.L. Gordin, P. Zhu, D. Lv, Y.B. Jiang, Y. Chen, Y. Duan, D. Wang, Adv. Funct. Mater. 24 (2014) 1243–1250.

[12] J. Guo, Y. Xu, C. Wang, Nano Lett. 11 (2011) 4288–4294.

[13] A. Barinov, L. Gregoratti, P. Dudin, S. La Rosa, M. Kiskinova, Adv. Mater. 21 (2009) 1916–1920.

[14] G. Zhou, F. Li, H.-M. Cheng, Energy Environ. Sci. 7 (2014) 1307–1338.

[15] Q. Li, Z. Zhang, K. Zhang, J. Fang, Y. Lai, J. Li, J. Power Sources 256 (2014)

137–144.

[16] J. Lee, B. Ko, J. Kang, Y. Chung, Y. Kim, W. Halim, J.H. Lee, Y.L. Joo, Mater. Today Energy 6 (2017) 255–263.

[17] B.P. Williams, Y.L. Joo, J. Electrochem. Soc. 163 (2016) A2745–A2756.

[18] J. Wang, Y. Yang, F. Kang, Electrochim. Acta 168 (2015) 271–276.

[19] H. Li, M. Sun, T. Zhang, Y. Fang, G. Wang, J. Mater. Chem. A 2 (2014) 18345–18352.

[20] Z. Gong, Q. Wu, F. Wang, X. Li, X. Fan, H. Yang, Z. Luo, RSC Adv. 5 (2015) 96862–96869.

[21] L. Ji, M. Rao, H. Zheng, L. Zhang, Y. Li, W. Duan, J. Guo, E.J. Cairns, Y. Zhang, J. Am. Chem. Soc. 133 (2011) 18522–18525.

[22] X. Zhou, Y. Li, G. Ma, Q. Ma, Z. Lei, J. Alloys Compd. 685 (2016) 216–221.

[23] S. Stankovich, D.A. Dikin, R.D. Piner, K.A. Kohlhaas, A. Kleinhammes, Y. Jia, Y. Wu, S.B.T. Nguyen, R.S. Ruoff, Carbon N. Y. 45 (2007) 1558–1565.

[24] H.C. Schniepp, J.L. Li, M.J. McAllister, H. Sai, M. Herrera-Alonson, D.H. Adamson, R.K. Prud'homme, R. Car, D.A. Seville, I.A. Aksay, J. Phys. Chem. B 110 (2006) 8535–8539.

[25] X. Liang, C. Hart, Q. Pang, A. Garsuch, T. Weiss, L.F. Nazar, Nat. Commun. 6 (2015).

[26] L. Qie, A. Manthiram, Adv. Mater. 27 (2015) 1694–1700.

[27] L. Zhang, L. Ji, P.-A. Glans, Y. Zhang, J. Zhu, J. Guo, Phys. Chem. Chem. Phys. 14 (2012) 13670.

[28] A. Ganguly, S. Sharma, P. Papakonstantinou, J. Hamilton, J. Phys. Chem. C

115 (2011) 17009–17019.

[29] C. Mattevi, G. Eda, S. Agnoli, S. Miller, K.A. Mkhoyan, O. Celik, D. Mastrogiovanni, G. Granozzi, E. Carfunkel, M. Chhowalla, Adv. Funct. Mater. 19 (2009) 2577–2583.

[30] X. Liang, C. Hart, Q. Pang, A. Garsuch, T. Weiss, L.F. Nazar, Nat. Commun. 6 (2015) 5682.

[31] P.-G. Ren, D.-X. Yan, X. Ji, T. Chen, Z.-M. Li, Nanotechnology 22 (2011) 55705.

[32] H. Tang, C. Yang, Z. Lin, Q. Yang, F. Kang, C.P. Wong, Nanoscale 7 (2015) 9133–9139.

[33] M. Mustafa, M.N. Awais, G. Pooniah, K.H. Choi, J. Ko, Y.H. Doh, J. Korean Phys. Soc. 61 (2012) 470–475.

[34] J.M. Polfus, O.M. Løvvik, P.M. Rørvik, R. Bredesen, J. Eur. Ceram. Soc. 36 (2016) 719–724.

[35] L. Fei, S.H. Yoo, R.A.R. Villamayor, B.P. Williams, S.Y. Gong, S. Park, K. Shin, Y.L. Joo, ACS Appl. Mater. Interfaces 9 (2017) 9738–9746.

[36] Z.W. Seh, W. Li, J.J. Cha, G. Zheng, Y. Yang, M.T. McDowell, P.C. Hsu, Y. Cui, Nat. Commun. 4 (2013).

[37] E. Peled, M. Goor, I. Schektman, T. Mukra, Y. Shoval, D. Golodnitsky, J. Electrochem. Soc. 164 (2017) A5001–A5007.

[38] Z.-J. Han, K. Yamagiwa, N. Yabuuchi, J.-Y. Son, Y.-T. Cui, H. Oji, A. Kogure, T. Harada, S. Ishikawa, Y. Aoki, S. Komaba, Phys. Chem. Chem. Phys. 17 (2015) 3783–3795.

[39] X. Ji, K.T. Lee, L.F. Nazar, Nat. Mater. 8 (2009) 500–506.

[40] J. Schuster, G. He, B. Mandlmeier, T. Yim, K.T. Lee, T. Bein, L.F. Nazar, Angew. Chemie - Int. Ed. 51 (2012) 3591–3595.

[41] Q. Pang, D. Kundu, M. Cuisinier, L.F. Nazar, Nat. Commun. 5 (2014) 4759.

[42] L. Stobinski, B. Lesiak, A. Malolepszy, M. Mazurkiewicz, B. Mierzwa, J. Zemek, P. Jiricek, I. Bieloshapka, J. Electron Spectros. Relat. Phenomena 195 (2014) 145–154.

[43] H. Chen, M.B. Müller, K.J. Gilmore, G.G. Wallace, D. Li, Adv. Mater. 20 (2008) 3557–3561.

[44] P. Barai, A. Mistry, P.P. Mukherjee, Extrem. Mech. Lett. 9 (2016) 359–370.

[45] H. Yamin, A. Gorenshtein, J. Penciner, Y. Sternberg, E. Peled, J. Electrochem. Soc. 135 (1988) 1045.

[46] S.-E. Cheon, K.-S. Ko, J.-H. Cho, S.-W. Kim, E.-Y. Chin, H.-T. Kim, J. Electrochem. Soc. 150 (2003) A800.

[47] J.R. Akridge, Y. V. Mikhaylik, N. White, in:, Solid State Ionics, 2004, pp. 243–245.

[48] V.S. Kolosnitsyn, E. V. Kuzmina, E. V. Karaseva, S.E. Mochalov, J. Power Sources 196 (2011) 1478–1482.

[49] M. Fantauzzi, B. Elsener, D. Atzei, A. Rigoldi, A. Rossi, RSC Adv. 5 (2015) 75953–75963.

[50] C. Fu, B.M. Wong, K.N. Bozhilov, J. Guo, Chem. Sci. 7 (2016) 1224–1232.

CHAPTER 5

CONCLUSION AND FUTURE WORKS

Lithium Sulfur Prospects

Due to ever increasing demand for energy storage, lithium-sulfur batteries exhibit one of the most propitious technology to replace the conventional lithium-ion battery due to low costs and high theoretical capacity and its energy density. Focus on achieving high reversible capacity and addressing safety issues have been intensified since 2008. In this work, we mainly focus on the fabrication method by utilizing air-controlled electrospray to provide polysulfide barrier and porous mechanical structures to accommodate sulfur expansion and excellent accessibility of electrolyte-sulfur interface.

The commercialization of lithium-sulfur might be closer than we expected. A lot of resources were dedicated to the development of advanced renewable technology, and energy storage to meet increasing demand for portable electronics, and electric vehicles, and also to combat climate change. However, to bring this technology to the market, many problems need to be solved, in particular, safety issues. The use of pure lithium metal as an anode source might not be the brightest idea, as it easily oxidized and flammable when it exposed to the open atmosphere. Moreover, the use of toxic electrolyte is also dangerous and causing health concern. These areas need more attention and investigation.

For this Master of Science thesis, I only applied carbonaceous materials to improve the performance of lithium-sulfur batteries. Working with the lithium-sulfur battery was one of the most memorable experiences in my life. Due to time constraint, I was not able to investigate the fundamental of lithium-sulfur and its transport, kinetic, or thermodynamic properties more deeply. However, I learned on how to perform and analyze various characterizations technique (SEM, EDS, XRD, XPS, TGA, BET, EIS, CV, FTIR, UV-vis, Raman spectra, etc) to elucidate the behavior of the cells. In the future works, I would like to incorporate metal oxide or conductive pillar to improve the performance further and investigate the compatibility with air-controlled electrospray. Also, the needs for safer and more benign electrolyte and lithium anode also encourages me to explore their properties and utilizes air-controlled electrospray to coat the sensitive lithium anode and mitigate the toxicity. Also, performing numerical simulation from continuum analysis also an interesting idea to bridge mathematics to kinetics or transport properties of lithium-sulfur. By having an accurate model, surely it will be beneficial for the future research. The idea of integrating simulation concerning lithium-sulfur performance will also elucidate the kinetics, mass transport, and thermodynamic properties of lithium-sulfur to step up the investigation to the next level.